MAGNETICALLY ACTIVE REGENERATION

by

Carl P. Tausczik

B.S.M.E., Stanford University

1980

S.M.M.E., Massachusetts Institute of Technology

1982

Submitted to the Department of Mechanical

Engineering in partial fulfillment of the

Requirements for the Degree of

DOCTOR OF PHILOSOPHY

at the

MASSACHUSETTS INSTITUTE OF TECHNOLOGY

October 1986

© Massachusetts Institute of Technology 1986

Signature of Author _____

Department of Mechanical Engineering
October 21, 1986

Certified by _____

Yukikazu Iwasa
Thesis Supervisor

Certified by _____

oseph L. Smith, Jr.
Thesis Supervisor

Accepted by _____

Ain A. Sonin
Chairman, Departmental Committee on Graduate Students

MASSACHUSETTS INSTITUTE
OF TECHNOLOGY

MAR 09 1987

LIBRARIES

MAGNETICALLY ACTIVE REGENERATION

by

Carl P. Tausczik

Submitted to the Department of Mechanical Engineering
on October 21, 1986 in partial fulfillment of the
requirements for the Doctor of Philosophy

ABSTRACT

The concept of magnetically active regeneration is explored in a prototype magnetic refrigerator which has produced a refrigeration of 0.40 W at 3.79 K while rejecting 3.0 W to a 5.51 K sink. The prototype refrigerator consists of a Gadolinium-Gallium-Garnet ($Gd_3 Ga_5 O_{12}$) regenerator core excited by an AC superconducting solenoid. A reversing flow of 3 atm supercritical helium carries the heat of magnetization to the hot reservoir and refrigerates the cold reservoir with the cooling of demagnetization.

Thesis Supervisor: Dr. Yukikazu Iwasa
Title: Senior Research Engineer, Francis Bitter National Magnet Laboratory

Thesis Supervisor: Professor Joseph L. Smith, Jr.
Title: Professor of Mechanical Engineering

Acknowledgments

I want to thank all the people who made this thesis an enjoyable and educational experience. In particular I want to thank the following friends whose help made this project possible. Ruth Heffernan; for constructing the 10 K temperature controller and whose indefatigable spirit and sense of humor brightened the basement of building 41. Woody Chin: for fabricating the superconducting magnet, with the skillful assistance of John Deydt, and for his boundless enthusiasm and great heart. Steve Fantone, president of the Optikos Corporation; for machining the magnetic refrigerant and proving to me that all republicans aren't bad people. Fred Cogswell, my capable successor; for his help with the first experiments. I owe my deepest thanks to Greg Gallagher, who assisted me on all aspects of the project, it has been a great pleasure to work with him. Finally, I wish to thank my mother, Ruth Taussig, for her sacrafice, love, and confidence.

Table of Contents

Abstract i
Acknowledgements ii
Table of Contents iii
List of Figures iv
List of Tables vi
1. Introduction to Magnetic Refrigeration 1
1.1 The Thermodynamics of Magnetism 1
1.2 Developement of Magnetic Refrigeration 4
2. Idealized Magnetically Active Regeneration 13
2.1 Design Concepts 13
2.2 Simple Model of the Ideal Cycle 14
3. Design of the Regenerator Core 20
3.1 Introduction 20
3.2 Selection of Uniform Field and Constant Core Cross-Section . . . 20
3.3 Specification of the Design 22
3.4 Specification of the Internal Geometry of the Regenerator Core . . 35
4. The Experiments 57
4.1 Experimental Apparatus 57
4.2 Procedure for the Preliminary Experiments 71
4.3 Results 76
Appendix 1 Thermodynamics of a Magnetic Substance 100
Appendix 2 Design of the Superconducting Solenoid 105
Appendix 3 Fabrication of the Regenerator Core 116
References 126
Annotated Bibliography 128

List of Figures

1.1.1 Magnetic Material in Solenoidal Field 2
1.2.1 Open Cycle Adiabatic Demagnetization 5
1.2.2 Magnetic Carnot Cycle with Superconducting Valves 6
1.2.3 Carnot, Stirling, & Ericsson Magnetic Cycles 7
1.2.4 Double-Acting Reciprocating Magnetic Refrigerator 8
1.2.5 Carnot Cycle Machine with AC Magnet and Heat Switch 9
1.2.6 Limitation of Carnot Cycle Temperature Span 10
1.2.7 Fluid-Core-Regenerator Stirling Cycle 11
2.2.1 Cascaded Carnot Cycle Refrigerators 14
2.2.2 Idealized Temperature Profiles 15
2.2.3 Incremental Magnetic Carnot Refrigerator 15
2.2.4 Efficiency and Performance for the Idealized Cycle 18
2.2.5 Hardware Schematic of Idealized Refrigerator 18
3.3.1 Idealized Temperature Profiles in the Working Fluid 23
3.3.2 Timing Variables for the Active Regeneration Cycle 24
3.3.4 Time Dependence of Magnetic Field 26
3.3.5 Specific Heat at Constant pressure for Helium 27
3.3.6 Phase Diagram for ^{4}Helium 28
3.3.7 Temperature-Entropy Diagram for GGG 30
3.3.8 Carnot Cycle at Cold End of Regenerator 31
3.3.9 Control Volume Used For Estimating ℓ 33
3.4.1 Effect of Entrainment on Carnot Cycle Capacity 36
3.4.2 Magnetic Refrigerant and Entrained Helium 37
3.4.3 Model of Packed Bed 39
3.4.4 Parallel Tube Core Geometry 40
3.4.5 Thermal Conductivity of GGG 41
3.4.6 Composite Construction of Parallel Tube Core 42
3.4.7 Interleved GGG and Thermal Barriers 42
3.4.7 Parallel Plate Core 44
3.4.8 Differential Section of Regenerator Core 46
3.4.9 Entropy Generation vs d at 5 K 49
3.4.10 Isothermal Wall Segment 50
3.4.11 Two Isothermal Segments 51
3.4.12 Comparison of Average Stream-to-Wall ΔT 52
3.4.13 Entropy Generation vs Number of Segments 53
3.4.14 Axial Conduction Heat Leak 54
3.4.15 Dimensionless Barrier Entrainment Loss 55

4.1.1 Configuration of the Magnetic Refrigerator . . . 58
4.1.2 Displacer Assembly . . . 60
4.1.3 Compensator Assembly . . . 62
4.1.4 Magnet system Schematic . . . 63
4.1.5 Core Container Section . . . 65
4.1.6 Temperature Controller Schematic . . . 67
4.1.7 Temperature Control Circuit . . . 68
4.1.8 Magnetic Refrigeration Dewar . . . 70
4.3.1 Data From a No-Flow Field-Cycling Run . . . 77
4.3.2 Initial Cycles of a Passive Regenerator Experiment . . . 79
4.3.3 Later Cycles of a Passive Regenerator Experiment . . . 81
4.3.4 Interpretation of Mass Flow Data . . . 82
4.3.4 Two Part Model of Working Volume . . . 84
4.3.5 Magnetic Field Waveform for the First Experiments . . . 86
4.3.6 Mass and Field Waveforms for $m_s = 4.5$ g . . . 87
4.3.7 Mass and Field Waveforms for $m_s = 6.25$ g . . . 88
4.3.8 Data From the 2.0 $g\,s^{-1}$ Run . . . 89
4.3.9 Data From the 1.0 $g\,s^{-1}$ Run . . . 89
4.3.10 Hot-End Temperature Transducer Mounting . . . 95
4.3.11 Run Illustrating Loss of Performance due to Magnet Lag . . . 97
4.3.12 Modification of Carnot Cycle for More Efficient Use of GGG . . . 99
A2.1 Cross-Section of Solenoid . . . 105
A2.2 Field Requirements for the Solenoid . . . 106
A2.3 Geometry of Center Section of Solenoid . . . 107
A2.4 Geometry of Compensating Coils . . . 109
A2.5 Model Used for Evaluating Biot-Savart Integral . . . 110
A2.6 Hexagonal Array of Superconducting Filaments . . . 112
A2.7 Variables for Heat Transfer Analysis . . . 114
A3.1 Sawing Strips from Laminated Segment . . . 118
A3.2 Reassembly of Thirty Wafer Long Strips with Shims . . . 119
A3.3 Header Plate Construction . . . 119
A3.4 Fitting the Header Plates to the Core Segments . . . 120
A3.5 Jig for Aligning the Header Plates . . . 120
A3.6 Header Plates Cover Only Shim Material . . . 121
A3.7 Pressure Checking Jig . . . 121
A3.8 Pressure Drop For Core Sections Compared to Design Values . . . 122
A3.9 Injector (right) and Mold with Core Section Inside . . . 123
A3.10 Pressure Drop For Fully-Assembled Core . . . 124

List of Tables

3.3.1 Design Variable Assignments 34
4.3.1 Distribution of Refrigerator Working Volume 83
4.3.2 Refrigeration Performance 94
A1.1 Summary of Appendix 1 104
A2.1 Magnet Data 115

Chapter 1 Introduction to Magnetic Refrigeration

This chapter introduces the thermodynamics of magnetism in section 1.1. Section 1.2 describes the use of the magneto-caloric effect in low temperature refrigeration from its roots as a one shot processes through its evolution into continuous machines employing both regenerative and non-regenerative cycles. The strengths and weaknesses discovered in this review highlight the reasons for choosing the cycle presented in Chapter 2.

1.1 The Thermodynamics of Magnetism

In a ferromagnetic material, the adjacent atoms in the lattice are closely coupled producing spontaneous alignment of the dipole moments. The dipole moments in paramagnetic materials are sufficiently uncoupled so that random thermal agitation prevents spontaneous alignment. The presence of an applied field causes the dipoles of a paramagnetic material to align parallel to the applied field. The magnetization of a paramagnet decreases with increasing thermal agitation and increases with the applied field. Around 1895 Pierre Curie quantified his experimental observations of paramagnets. Curie's law relates the magnetization $\mathcal{M}$, to the applied field intensity H, and the temperature T.

$$\mathcal{M} = C\frac{H}{T} \tag{1.1.1}$$

Curie's law becomes invalid at either very low temperatures or very high fields where alignment of the dipoles is approached, but it gives a qualitative understanding of the mechanism of paramagnetism.

Fig. (1.1.1) shows a solenoid of length ℓ wrapped around a bar of magnetic material with cross-sectional area A. If the resistance of the wire is neglected, then the entire terminal voltage, ε, is applied to changing the flux in the solenoid. The solenoid is long enough that B is uniform and axial inside and zero outside. The

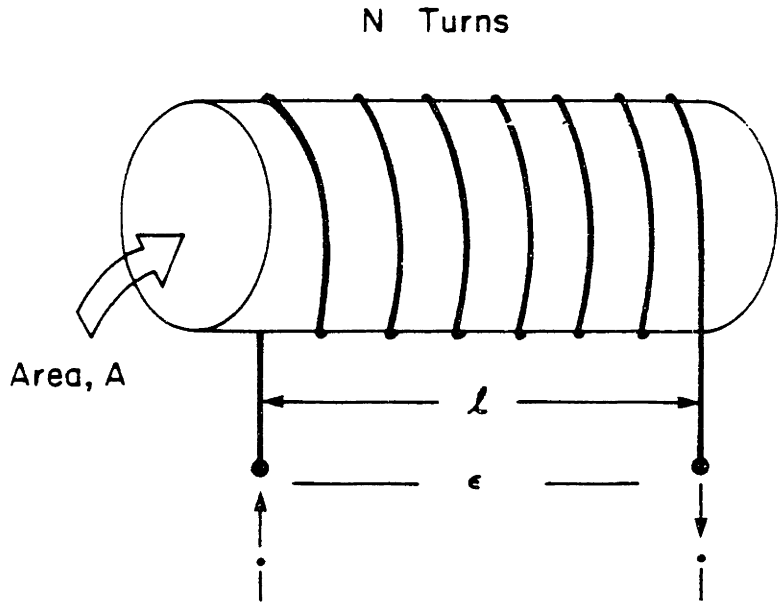

Fig. 1.1.1 Magnetic Material in Solenoidal Field

work done on the system by increasing the current through the solenoid winding by di in time dt (expressed in MKS units) is

$$dW_{sys} = \varepsilon i \, dt, \tag{1.1.2}$$

where ε is the terminal voltage and i is the average current during time dt. The terminal voltage calculated from Faraday's law is

$$\oint_c \bar{E} \cdot \bar{d\ell} = -\frac{d}{dt} \iint_s \bar{B} \cdot \bar{dA}$$

$$\varepsilon = -\frac{dB}{dt} NA, \tag{1.1.3}$$

where N is the number of turns of the solenoid. The current as function of the magnetic field intensity is found by Amphere's law.

$$\iint_s \left(\bar{J} + \frac{\bar{d\rho}}{dt} \right) \cdot \bar{dA} = \oint_c \bar{H} \cdot \bar{d\ell}$$

$$i = \frac{H\ell}{N} \tag{1.1.4}$$

The work defined in Eq. (1.1.2), expressed in terms of the magnetic variables is

$$\begin{aligned} dW_{sys} &= \frac{dB}{dt} N A \frac{H\ell}{N} dt \\ &= V H \, dB. \end{aligned} \tag{1.1.5}$$

where $V(= A\ell)$ is the volume of the magnetic material. Eq. (1.1.5) gives the work done by the solenoid on the system of the magnetic material and the space it occupies. This can be seen by expanding the magnetic induction into its components defined by $\overline{B} = \mu_0(\overline{H} - \overline{\mathcal{M}})$.

$$\begin{aligned} dW_{sys} &= V H \mu_0 (dH + d\mathcal{M}) \\ &= V \mu_0 (H \, dH - H \, d\mathcal{M}) \end{aligned} \tag{1.1.6}$$

The first term is the work done increasing the field in free space. The second term represents the work done on the magnetic material. Therefore, the work done by the magnetic material during this process is the inverse of the second term since thermodynamic work is defined as positive when performed by the system.

$$dW_{mag} = -V \mu_0 H \, d\mathcal{M} \tag{1.1.7}$$

The general differential form of the combined first and second laws of thermodynamics is

$$dU = T \, dS - dW. \tag{1.1.8}$$

Eq. (1.1.8) can be rewritten in terms of the magnetic variables, assuming the system only undergoes magnetic work interactions.

$$T \, dS = dU + \mu_0 V H \, d\mathcal{M} \tag{1.1.9}$$

A useful analogy can be shown by comparing Eq. (1.1.9) to the $T \, ds$ equation for a simple compressible substance.

$$T\,dS = dU - P\,dV \tag{1.1.10}$$

The pressure P of a compressible substance is analogous to the magnetic field intensity H of a magnetic substance. The change in volume dV of the compressible substance and the quantity $-\mu_0 V\,d\mathcal{M}$ of the magnetic substance are also analogous. This analogy gives a useful insight into the magneto-caloric effect. An adiabatic demagnetization is analogous to an adiabatic expansion. Likewise, an isothermal magnetization is akin to an isothermal compression. Other details of the analogy are discussed in Appendix (1) and reference (1).

1.2 Developement of Magnetic Refrigeration

In 1895 Nickola Tesla patented an electrical generator which employed an iron link cyclically heated above its Curie point (the temperature where iron transforms to the bcc phase and loses its ferromagnetism) to produce a changing magnetic flux[2]. The first use of magnetic cooling was by physists trying to approach absolute zero[3]. Helium was first liquefied by Kamerlingh Onnes on July 9, 1908. Many saw this achievement as the last major step towards absolute zero. Lowering the vapor pressure over the liquid produced a temperature of approximately 1 K, but no lower temperatures could be reached with conventional gas cycles. In 1926, William Francis Giaque and Peter Debeye independently proposed magnetic cooling as a means of achieving temperatures below 1 K.

The scheme proposed by Giaque and Debeye utilized gadolinum sulfate, a rare-earth salt which obeys Curie's law at temperatures below 1 K. The crucial consequence being that to obey Curie's law the magnetic moments must be in a state of random thermal agitation (Fig. (1.2.1), state 1) which implies that the state of ordered dipole moments must correspond to a magnetized state (Fig. (1.2.1), state 2) or to a lower temperature in the absence of field (Fig. (1.2.1),state 3). Fig. (1.2.1) also shows the corresponding T-S diagram for the process. With this process Giaque achieved a temperature of 0.25 K in 1933.

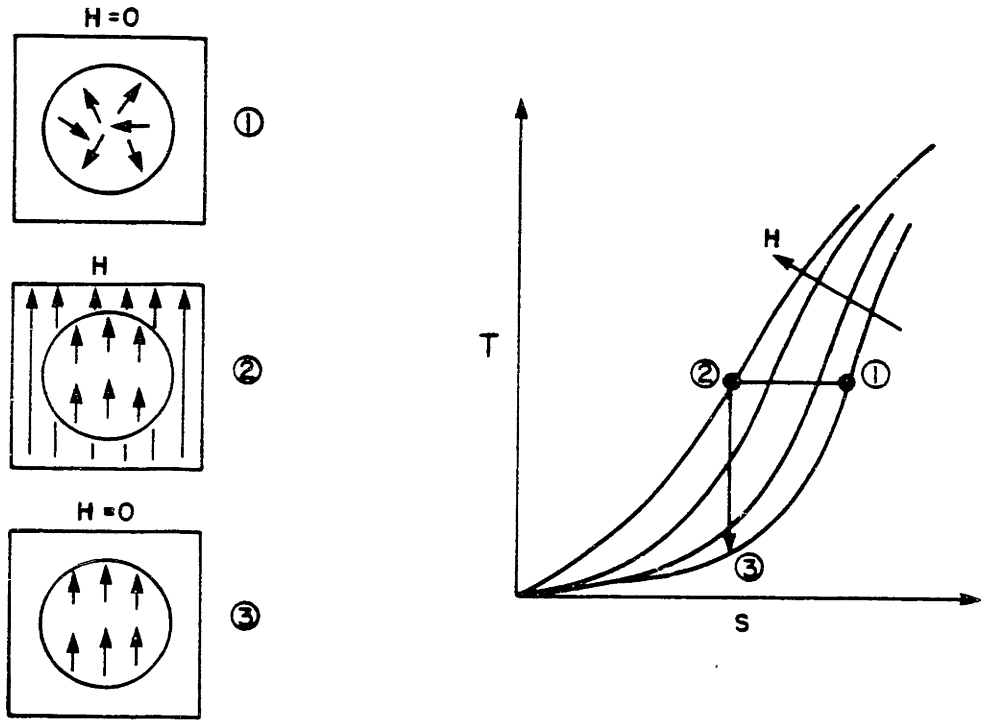

Fig. 1.2.1 Open cycle Adiabatic Demagnetization

The experiment was conducted in three steps. First, the salt was magnetized isothermally at 1 K (process 1-2 in the T-S diagram). Next, the salt is insulated from the 1 K bath by evacuating the space between them. Finally, the salt is demagnetized adiabatically, forcing the temperature to drop (process 2-3). The field in Giaque's experiment was produced by a resistive magnet requiring an intricate cryostat design. Giaque's experiment provided a technique for achieving temperatures as low as $\approx 15\,\mu$K by cascading stages[4]. The one-shot nature of Giaque's technique prohibited it from providing continuous refrigeration to a heat source at low temperatures.

In the 1950's and early '60's, continuous magnetic refrigerators were built to provide refrigeration at around 0.2 K. Fig. (1.2.2) shows a schematic of the machine built by Zimmerman, M$^{\underline{c}}$ Nutt, and Bohm[5] and its cycle on a T-S diagram.

This machine used ferric amoninum alum (a paramagnetic salt) grown about

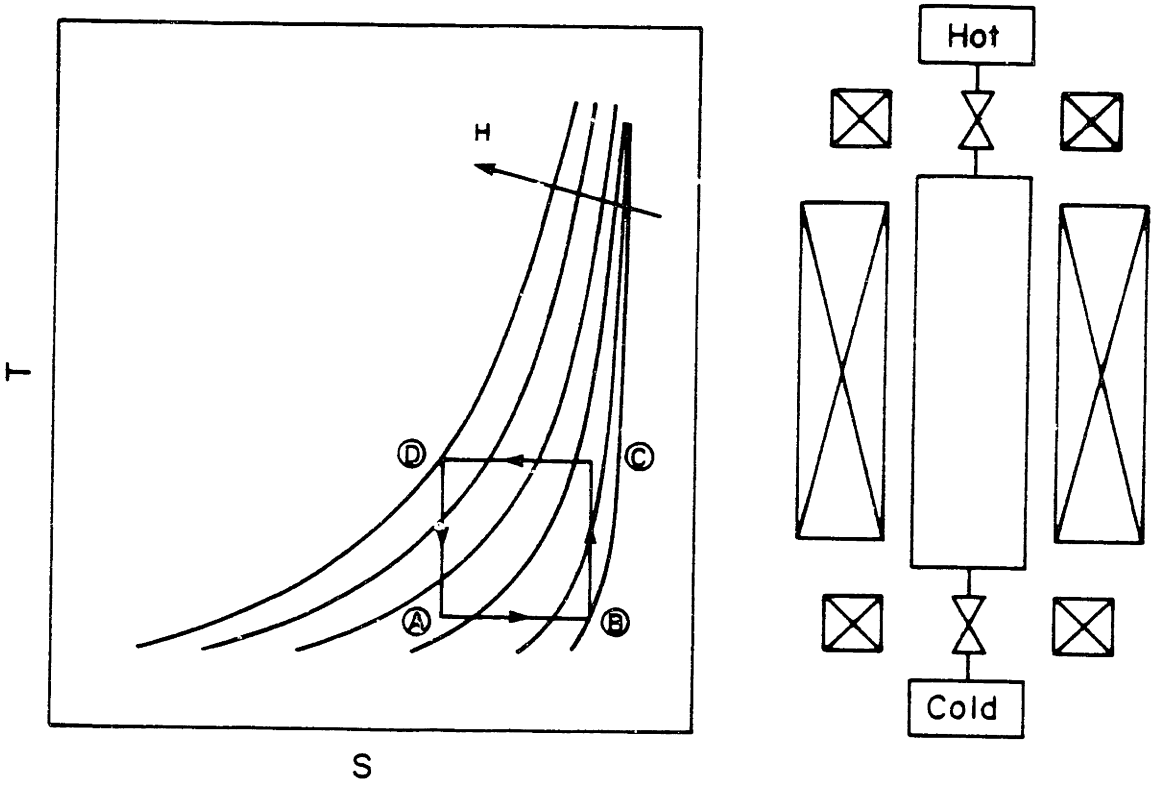

Fig. 1.2.2 Magnetic Carnot Cycle with Superconducting Valves

parallel strands of fine copper wire. The wires were bundled at each end of the working salt and soldered to lead superconducting valves, which in turn were connected to the hot and cold reservoirs. When the superconducting valves' critical field is exceeded, their heat conduction is greatly reduced, thereby closing the valve. The magnetic Carnot cycle executed by this machine was implemented by suitable variations in the magnetic field surrounding the paramagnetic material timed with appropriate operation of the superconducting valves. For example, during the isothermal demagnetization process (segment A-B on Fig. (1.2.2)) the hot valve is closed (high field) and the cold valve is open (low field) while the field on the magnetic refrigerant is decreased. The isothermal demagnetization process provides

refrigeration to the cold reservoir. The machine represents a great improvement over the experiments by Giaque. The superconducting valves allowed continuous operation with a heat load of 0.1 mW at 0.26 K. Superconducting valves are unsuitable for higher capacity machines because at high heat fluxes the valves lose their superconductivity analagous to the loss of superconductivity associated with exceding the critical current. Maintaining the aspect ratio of the valves (which is necessary to preserve the switching ratio between the conduction of an open valve and that of a closed valve) and increasing their size to accomodate the higher heat flux results in valves and magnets which are too large.

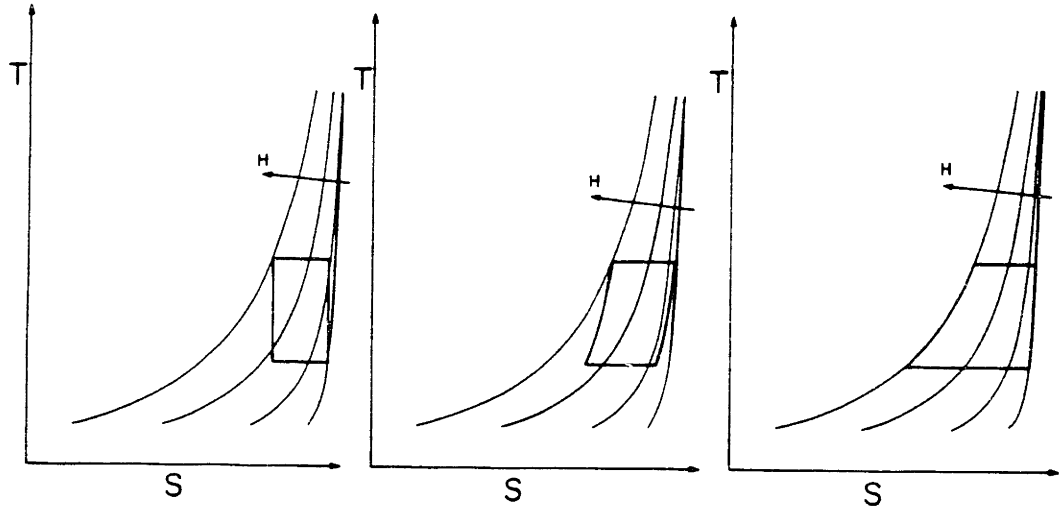

Fig. 1.2.3 Carnot, Stirling, & Ericsson Magnetic Cycles

The next step in the evolution of magnetic refrigeration has been the development of systems to provide multi watt refrigeration capacities at temperatures between 2 K and 4 K to sink temperatures in the 10-20 K range. Almost all the magnetic refrigerators built operate on the magnetic analogy of one of three thermodynamic cycles; Carnot, Stirling, or Ericsson. The magnetic refrigeration cycles

are shown on Fig. (1.2.3).

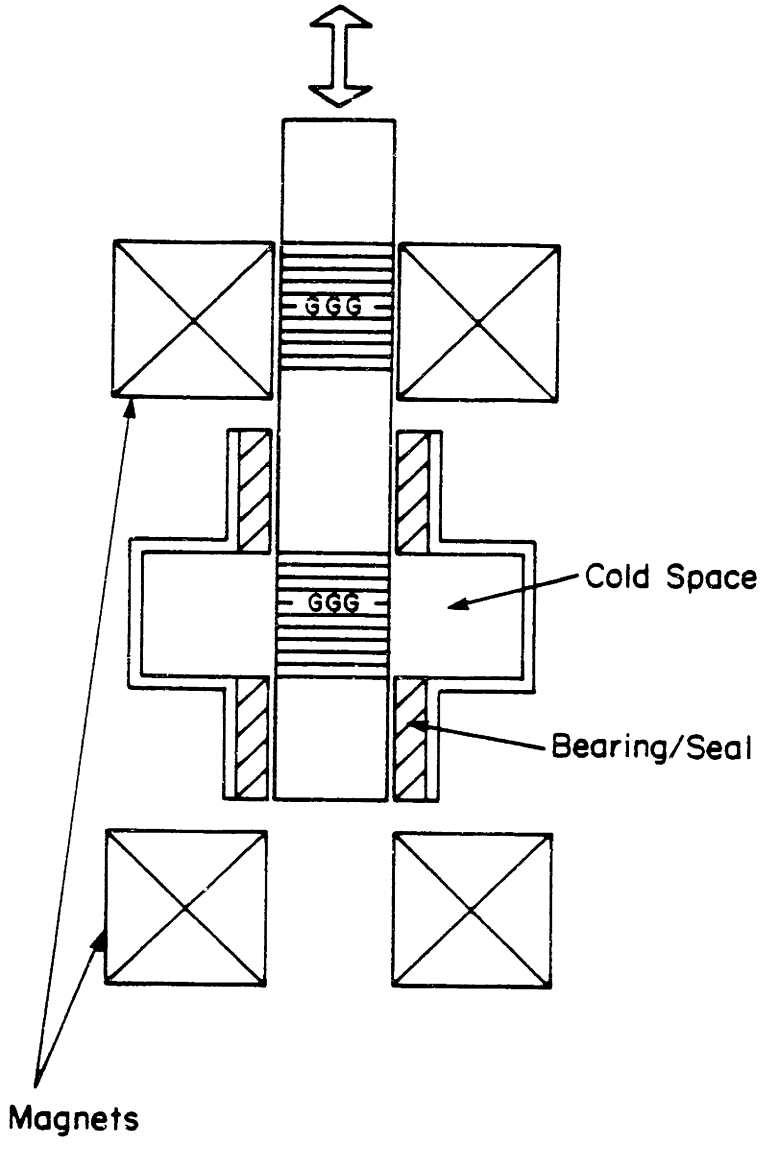

Fig. 1.2.4 Double-Acting Reciprocating Magnetic Refrigerator

The Carnot type machines will be discussed first, then the regenerative (Stirling and Ericsson) cycle machines. The design of Zimmerman *et al.*, mentioned before, was a Carnot cycle but its superconducting valves were poorly suited for high capacity heat transfer. A group of scientists in Grenoble France constructed a double-acting reciprocating Carnot-cycle refrigerator in 1981[6-11] which provided refrigeration at 1.8 K while rejecting heat to a sink at 4.2 K (Fig. (1.2.4)). It consists of two magnetic elements formed into a bar which is driven in a reciprocating

motion by a hydraulic servo.

At one extreme of the stroke an element is magnetized isothermally in a 4.2 K bath by superconducting coils while the other element demagnetizes isothermally in the 1.8 K superfluid bath. The elements undergo adiabatic processes during a stroke as they pass through the bearings either into or out of the magnetic field. The salt elements operate 180^0 out of phase. A maximum refrigeration of 1.2 W at 1.8 K was produced and by extending the heat transfer area a maximum of 80% of the Carnot efficiency was achieved. Three factors were the largest contributors to inefficiency in the system: friction of the magnetic elements in the seals, motion of fluid through the annular space between the bushings and the rod, and heat transfer losses due to film boiling in the 4.2 K bath and Kapitza resistance in the 1.8 K bath.

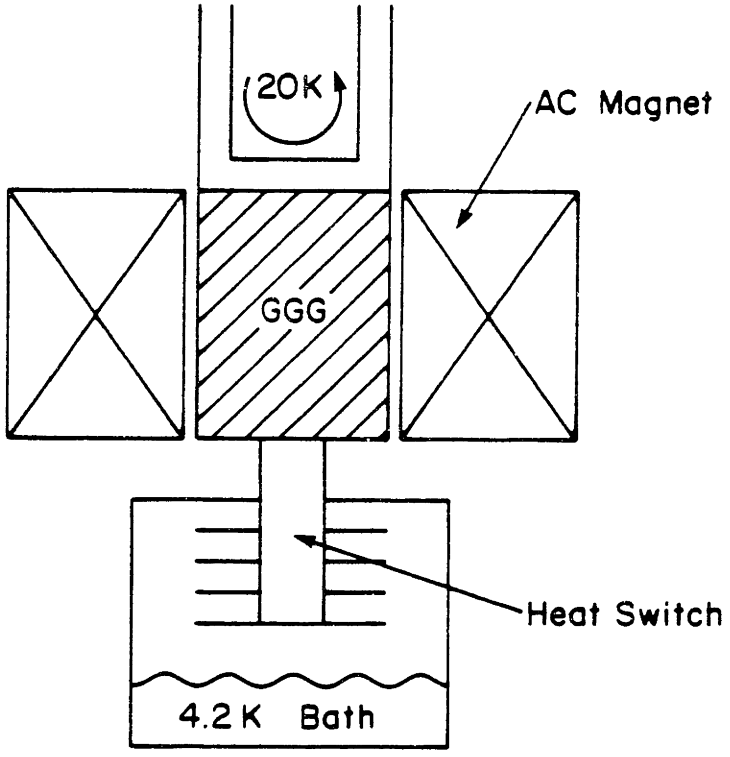

Fig. 1.2.5 Carnot Cycle Machine with AC Magnet and Heat Switch

Nakagome, *et al.* reported on another carnot cycle magnetic refrigerator in 1983[12]. This machine provides refrigeration at 4.2 K from a sink at 20 K. The schematic shown in Fig. (1.2.5) shows the four major components.

The novel heat switch allows heat to pass from the 4.2 K bath to the magnetic refrigerant salt but blocks the flow of heat in the opposite direction. The principle of operation is that when the salt is colder than 4.2K, helium condenses on its lower surface providing excellent heat transfer. When the refrigerant's temperature rises above 4.2 K a stable stationary helium gas barrier forms which has low thermal conductivity. The Carnot cycle of Fig. (1.2.2) is executed in the following four steps. Starting at point **B** in Fig. (1.2.2) the paramagnetic salt is isentropically magnetized to a temperature of 20 K at point **C**. during this process no gas flows in the 20 K circuit and the heat switch blocks communication with the 4.2 K bath. The salt is isothermally magnetized from point **C** to point **D** while gas flows in the 20 K circuit. The 20 K coolant flow is then stopped and the salt is demagnetized isentropically to 4.2 K at point **A** when the heat switch closes,thermally connecting the salt to the liquid helium bath. The cycle is closed by isothermal demagnetization to point **B**. The apparatus produces 6.25 W at 4.2 K with an efficiency of 50% of the ideal cycle. The efficiency given excludes the large losses generated in pulsed AC operation of the superconducting magnet.

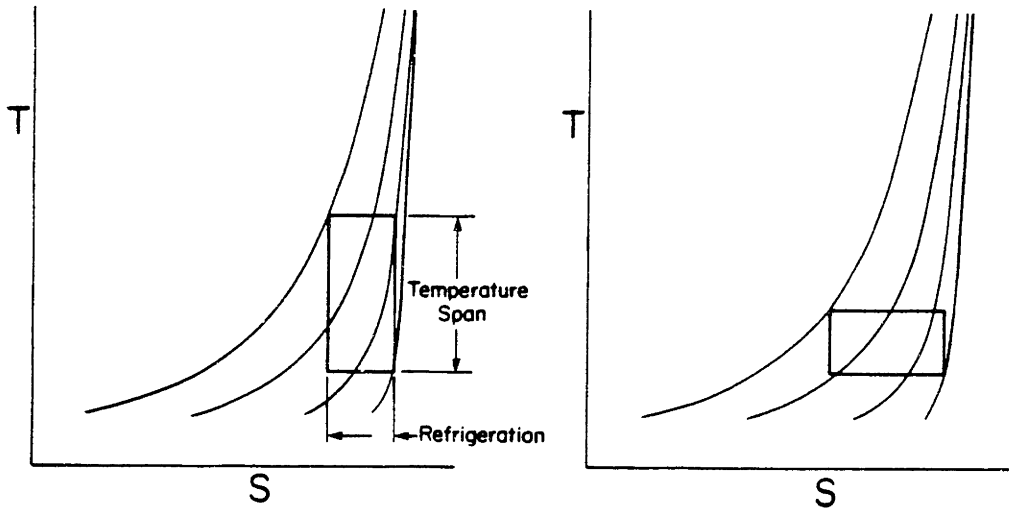

Fig. 1.2.6 Limitation of Carnot Cycle Temperature Span

The Carnot cycle is simpler to implement than the cycles employing regeneration but its temperature span is limited. Qualitatively, this is because as the tem-

perature span is increased, more of the total magnetization is required to change the temperature of the paramagnet so less is available for refrigeration. Fig. (1.2.6) illustrates the trade off between temperature span and refrigeration power for a limited maximum magnetic field intensity.

Ericsson and Stirling magnetic cycles (Fig. (1.2.3)) offer greater possible performance for machines with larger temperature span. Their drawback is that they require heat transfer over their complete temperature span. Designers have typically employed regenerative heat exchange to implement these cycles. It is possible to use either a thermally stratified working fluid as the thermal storage element or use the magnetic refrigerant itself as the regenerator.

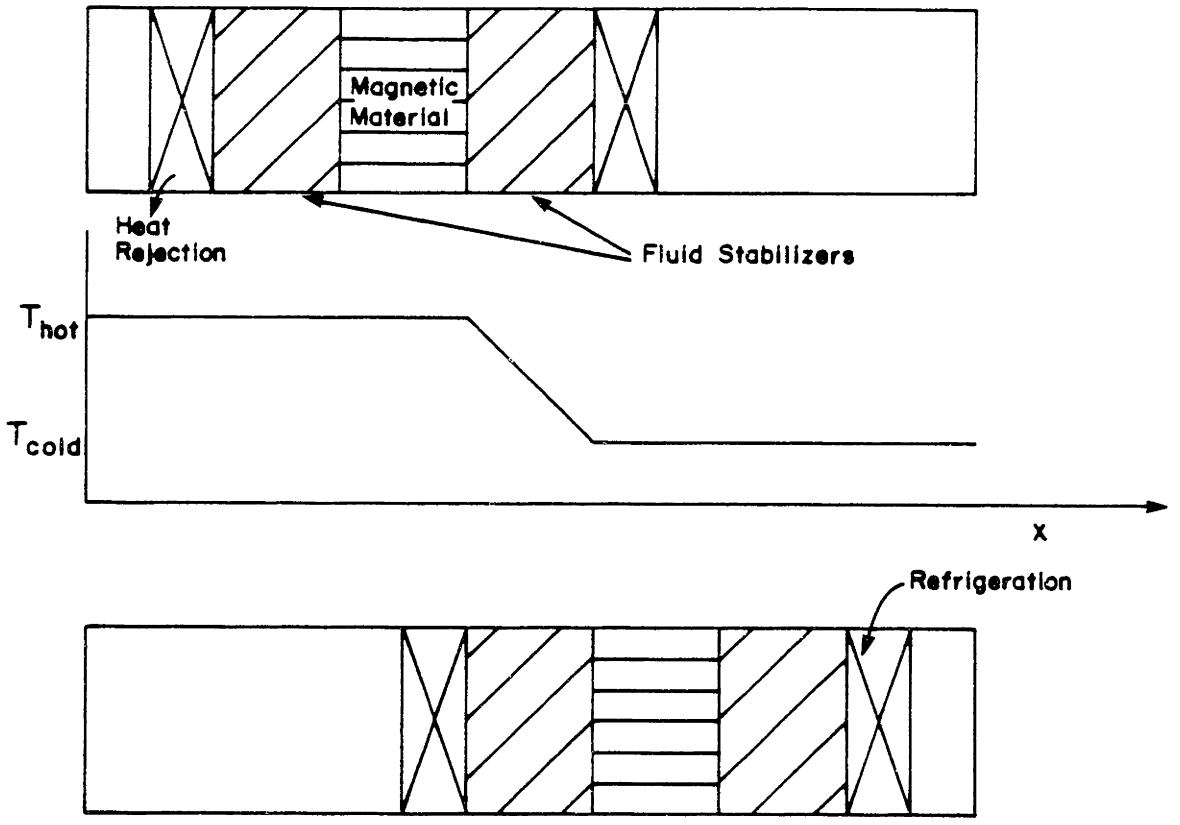

Fig. 1.2.7 Fluid Core Regenerator Stirling Cycle

The former concept was first suggested by Van Geuns in a PhD thesis at the University of Leiden in 1966[13]. Van Geuns proposed a Stirling cycle machine with a thermally stratified column of supercritical helium serving as a regenerator. The

temperature profile in the helium is shown in the center of Fig. (1.2.7). The components of the refrigerator are: the cooler which rejects heat to the hot reservoir, the freezer which cools the low temperature reservoir, the magnetic refrigerant, and stabilizers which prevent mixing in the fluid regenerator. In a complete cycle the magnetic refrigerant is first magnetized isothermally in the hot reservoir as shown in the top of Fig. (1.2.7).

The next process in the cycle is an isomagnetic heat regeneration where the magnetic refrigerant is swept through the fluid regenerator lowering its temperature to T_{cold}. The specific heat of the refrigerant is assumed insignificant relative to the supercritical helium so the temperature profile in the fluid regenerator remains unchanged. Once at T_{cold} the refrigerant is demagnetized isothermally providing cooling to the freezer (as shown by the bottom of Fig. (1.2.7)). The cycle is closed by returning the refrigerant through the regenerator at low magnetization to the hot reservoir.

In 1976 Brown implemented an Ericsson cycle machine using Van Geuns' concept at room temperature[14]. The regenerator in his machine was a mixture of ethyl alcohol and water. Porous plates of gadolinium were used as a magnetic refrigerant. A water-cooled electromagnet provided 7 T of induction. The machine provided a no load temperature span of 47 K. Brown noted substantial losses due to imperfect sealing around the moving element and due to jets causing mixing in the regenerator.

Barclay, Moze, and Patterson reported an Ericsson cycle magnetic refrigerator, again patterned after Van Geuns'. Their machine operated between 2 K and 4 K and produced approximately 50 mW of cooling power[15]. The design suffered from frictional heating due to motion of the magnetic refrigerant and mixing in the fluid core.

Other designs have been proposed which employ helium working fluid and an active regenerator core constructed from a magnetic refrigerant[16]. The refrigerator described in the remainder of this thesis is also of this type.

Chapter 2 Idealized Magnetically Active Regeneration

Chapter 1 discussed the history of continuous magnetic refrigeration. This chapter begins in section 2.1 with a discussion of the difficulties designers have encountered in evolving the technique. Section 2.1 concludes with a presentation of the design concepts underlying the present effort. Section 2.2 introduces a simple analytical framework to describe the idealized cycle then describes the hardware required to realize the cycle. In closing, section 2.2 discusses the losses present in the real cycle.

2.1 Design Concepts

The machines discussed in the previous chapter fall into two categories: Carnot cycles, and regenerative cycles. Carnot cycles have suffered from two basic difficulties. The magneto-thermodynamics of the magnetic refrigerant limit the temperature span. And low thermal conductance between the magnetic refrigerant and the reservoirs has limited performance. Regenerative machines constructed so far have had difficulties with mixing in the fluid regenerator. Both Carnot and regenerative cycles have had losses associated with friction generated by relative motion of the magnetic components, and leakage and friction caused by cold seals.

The design concepts for the present effort were motivated by the experience gained from previous machines. A regenerative cycle was chosen because of its ability to span the 4-10 K temperature range with relatively low intensity magnetic fields. A second inherent advantage of regenerative cycles is forced convection heat transfer. It was decided to use the magnetic refrigerant as the regenerator core to avoid the problems of mixing in fluid regenerators. To avoid the problem of cold-seal leakage it was agreed that the regenerator core should be stationary. The helium working fluid would be circulated by warm sealed displacers. In order to prevent friction due to relative motion of the magnetic components, it was resolved to excite the magnetic refrigerant via AC operation of a superconducting solenoid. It will

be shown in Appendix 2 and discussed in Chapter 3 that the AC losses for superconducting solenoids at low frequency can be made small relative to refrigeration power.

2.2 Simple model of the Ideal Cycle

The proposed cycle can be idealized as a series of cascaded Carnot cycle refrigerators (Fig. (2.2.1)). In one cycle, a mass of helium m_s flows from the cold reservoir at temperature T_{cold} and is heated as it flows across the tops of the heat pumps until it reaches the hot reservoir with a temperature greater than T_{hot}.

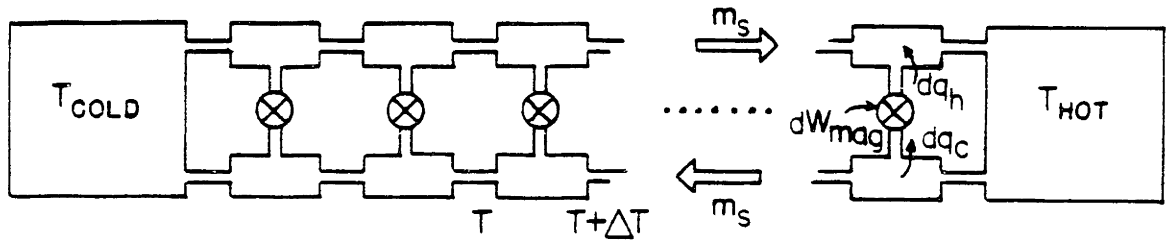

Fig. 2.2.1 Cascaded Carnot Cycle Refrigerators

An equal mass of helium flows from the hot reservoir and is cooled as it passes along the bottom of the heat pumps until it reaches the cold reservoir with a temperature less than T_{cold}, thus providing refrigeration to the cold bath. Fig. (2.2.2) shows idealized temperature profiles for the cycle.

The temperature distribution $T_h(x)$ is in the stream which is being heated and $T_c(x)$ is the temperature profile in the stream being cooled. In this simple analysis, it is assumed that enough Carnot refrigerators are present so that each one only heats or cools the working fluid by a differential increment in temperature. Further assume the working fluid is a simple substance with a constant specific heat c and that all interactions between the Carnot refrigerators and working fluid are loss-free. Fig. (2.2.3) shows an individual incremental heat pump removed from an arbitrary location in the refrigerator.

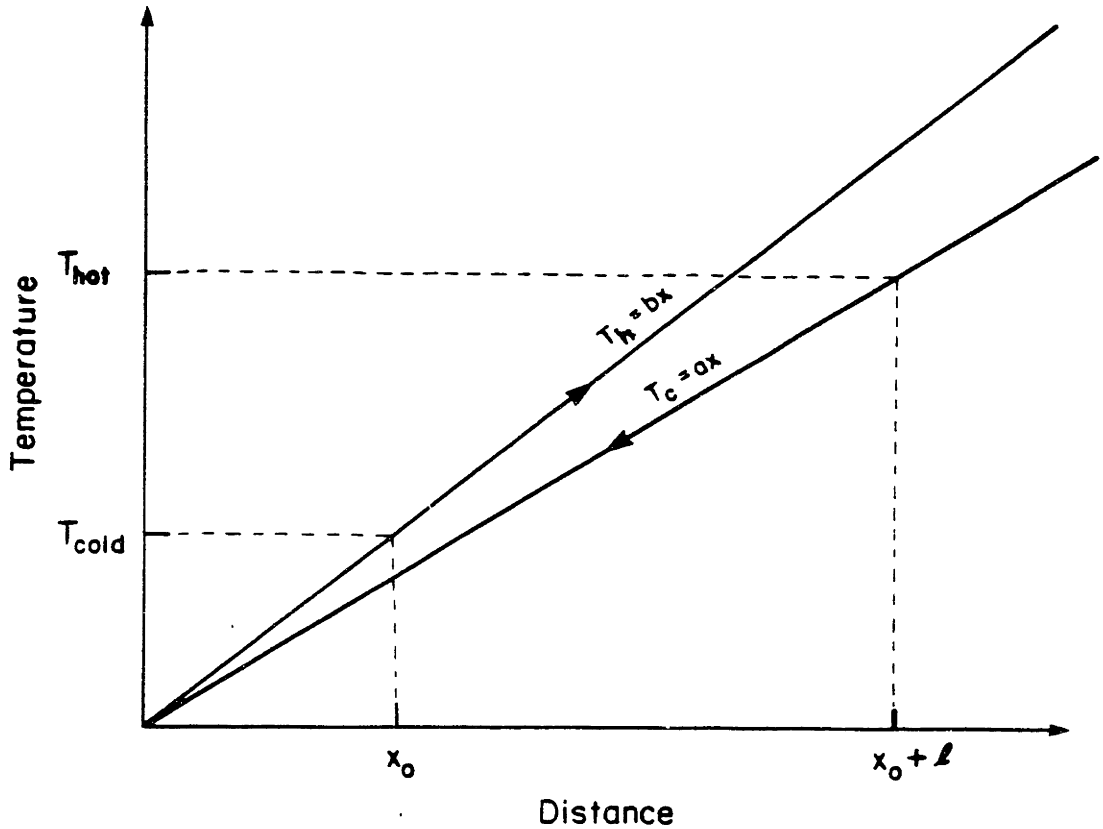

Fig. 2.2.2 Idealized Temperature Profiles

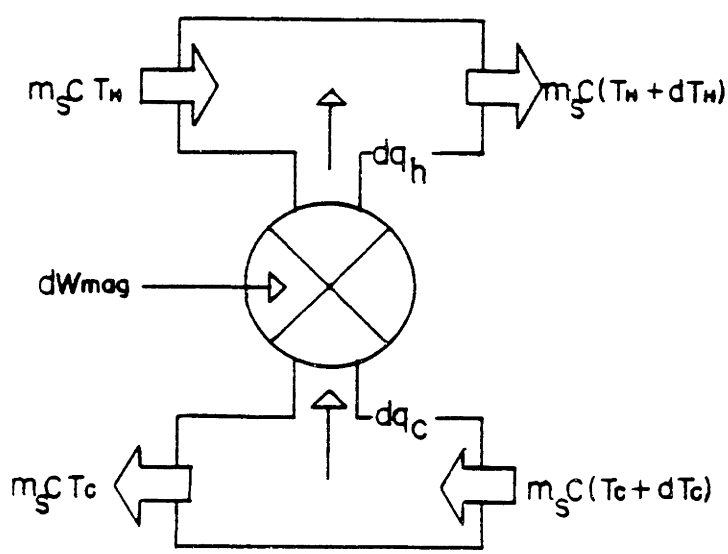

Fig. 2.2.3 Incremental Magnetic Carnot Refrigerator

The energy balance for the incremental heat pump for a complete cycle is

$$dW_{mag} = dq_h - dq_c, \tag{2.2.1}$$

where $$dq_h = m_s c\, dT_h, \tag{2.2.2}$$

and $$dq_c = m_s c\, dT_c. \tag{2.2.3}$$

The entropy balance for the reversible cycle is

$$\frac{m_s c\, dT_h}{T_h} = \frac{m_s c\, dT_c}{T_c}. \tag{2.2.4}$$

Eq. (2.2.4) can be integrated to show that the ratio of hot and cold temperatures is a positive constant greater than unity, independent of location.

$$\frac{T_h(x)}{T_c(x)} = \text{constant} = K \tag{2.2.5}$$

The functional dependence of the temperatures on position is not determined by Eq. (2.2.5). If the temperature distributions are specified apriori, then the required magnetic work input as a function of location can be determined by an energy balance. As an illustrative example, consider the simple case of linear temperature profiles shown on Fig. (2.2.2).

$$T_c(x) = ax \tag{2.2.6}$$

$$T_h(x) = bx \tag{2.2.7}$$

These temperature profiles are subject to the conditions $T_c(x_0 + \ell) = T_{hot}$ and $T_h(x_0) = T_{cold}$. The energy balance for the differential Carnot cycle, at an arbitrary location x, shows the magnetic work input per unit length W'_{mag} required as a function of position.

$$m_s c(\frac{dT_h}{dx}dx - \frac{dT_c}{dx}dx) - W'_{mag}\, dx = 0 \tag{2.2.8}$$

Assuming the linear temperature functions defined by Eq. (2.2.6) and Eq. (2.2.7) the magnetic work per unit length is

$$W'_{mag} = m_s c(b - a). \tag{2.2.9}$$

This result shows that for linear temperature profiles and constant specific heat working fluid the magnetic work input per unit length is constant.

The refrigeration and efficiency of the ideal cycle depend on the temperature profile ratio K. The refrigeration power per cycle is calculated by an energy balance on the cold reservoir.

$$\dot{Q}_{ref} = \frac{m_s}{t} c T_{cold}(1 - \frac{1}{K}) \tag{2.2.10}$$

t is the total cycle time in Eq. (2.2.10). Similarly the heat rejection is calculated from an energy balance on the hot reservoir.

$$\dot{Q}_{rej} = \frac{m_s}{t} c T_{hot}(K - 1) \tag{2.2.11}$$

An efficiency for a refrigeration cycle can be defined

$$\eta = \frac{\dot{Q}_{ref}/\dot{Q}_{rej}}{T_{cold}/T_{hot}}. \tag{2.2.12}$$

An ideal refrigerator efficiency as calculated by Eq. (2.2.12) is unity. The efficiency for the distributed Carnot cycle machines is $1/K$. Fig. (2.2.4) shows the efficiency of the ideal cycle plotted versus the nondimensional refrigeration ($\dot{Q}_{ref}/\frac{m_s}{t} c T_{cold}$). It is shown on the figure that refrigeration increases with the temperature profile ratio K, but the efficiency decreases. The maximum efficiency for the cycle is less than the Carnot efficiency despite being completely reversible internally because the refrigeration and rejection are generated via thermal mixing in the reservoirs.

Fig. (2.2.5) shows schematically the hardware required to realize the distributed Carnot cycle refrigerator. The figure shows a porous matrix of magnetic refrigerant connected to the hot and cold reservoirs. The reservoirs are shown as flexible bellows capable of expanding and contracting in phase to drive the shuttle mass of helium between them through the porous bed. The core is surrounded by a magnet providing a field whose intensity is a function of space and time.

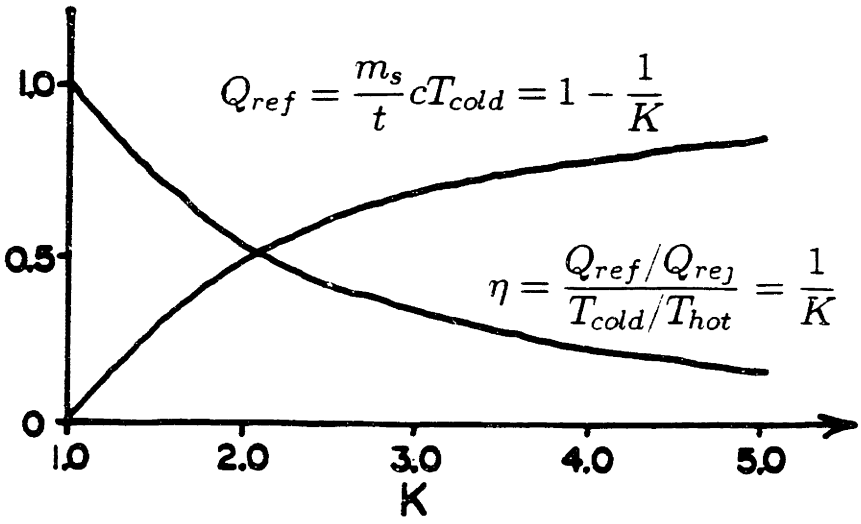

Fig. 2.2.4 Efficiency and Performance for the Ideal Cycle

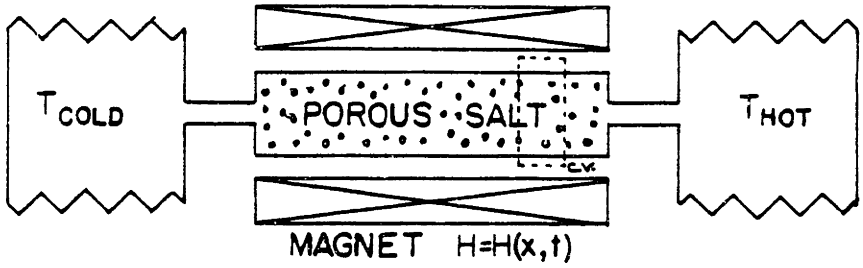

Fig. 2.2.5 Hardware Schematic of Idealized Refrigerator

The distributed Carnot cycle is realized in four discrete processes. First the shuttle mass, initially in the hot reservoir, is driven through the core by compressing the warm bellows and expanding the cold. During this flow process, the magnetic field is decreased in such a way that the temperature profile in the helium stream approximates that of $T_c(x)$ on Fig. (2.2.2). In the second step there is no flow. The core is adiabatically magnetized until the temperature profile becomes that of $T_h(x)$. During the third step, the shuttle mass flows from the cold reservoir to the hot while the magnetization continues in a manner to maintain the temperature profile at

$T_h(x)$. The fourth step completes the cycle by demagnetizing the core adiabatically while the shuttle mass resides in the hot reservoir returning the temperature profile to $T_c(x)$ in preparation for the next cycle to begin.

In order for the hardware represented by Fig. (2.2.5) to duplicate the ideal distributed carnot cycle, the losses were ignored. Irreversibilities in the actual cycle stem from various sources: axial conduction of heat through the regenerator core, stream-to-wall temperature gradients, temperature gradients within the magnetic refrigerant, fluid friction in the flow passages of the regenerator core, and entrainment of helium within the regenerator core.In addition to these idealizations concerning interaction of the fluid and matrix, the nature of the working fluid itself is important. The actual working fluid will have neither constant density nor constant specific heat; these non-ideal working fluid properties complicate the design.

The subject of how these losses were managed in the design and how the field profiles, temperature profiles, and mass flow rates were selected for the particular design are the subject of the next chapter.

Chapter 3 Design of the Regenerator Core

3.1 Introduction

This chapter describes in detail the design of the regenerator core used to experimentally investigate the cycle proposed in chapter 2. The design presented is not intended to be optimal. It represents the author's interpretation of the most feasible approach to create a flexible test apparatus able to generate a wide variety of data from a modicum of skills and resources.

The remaining three sections of this chapter are organized in terms of the evolution of the design. Section 3.2 explains the reasons for making the initial simplifications of spatially uniform magnetic field and constant regenerator cross section. Section 3.3 defines the set of variables which descibe the design and introduces the constraints and performance parameters used to specify those variables. A feasible set of design variables are selected exclusive of the internal geometry of the regenerator core. Section 3.4 completes the design by specifying the internal geometry of the core. This section examines the roles of the various loss mechanisms and considers the best geometry to minimize them. The assumptions made in the earlier analysis are then verified for the specific core geometry selected.

3.2 Selection of Uniform Field and Constant Core Cross-Section

The regenerator core designed for this experiment is roughly a right circular cylinder and the magnet which surrounds it provides a field which is spatially uniform throughout the core. These decisions were not mandated by the analysis; either or both the shape of the regenerator core or the magnetic field might be functions of position along the axis. The particular shape of the core and field intensity profile were initially considered because they would be the simplest to design and manufacture. The decision was supported by a simple analysis which approximates the equation of state of the magnetic refrigerant to be that of a simple paramagnet governed by Curie's law.

$$\mathcal{M} = C\frac{H}{T} \tag{3.2.1}$$

The cannonical form of the combined first and second laws for the magnetic material was derived in Chapter 1 (Eq. (1.1.9)). This Tds relation can be rewritten with H and T as independent variables.

$$T\,ds = c_H\,dT - \mu_0 v T\left(\frac{\partial \mathcal{M}}{\partial T}\right)_H dH \tag{3.2.2}$$

For an isothermal process the heat of magnetization, dq_T, is equal to the isothermal magnetic work.

$$dq_T = T\,ds\,|_T = \mu_0 v T\left(\frac{\partial \mathcal{M}}{\partial T}\right)_H dH_T \tag{3.2.3}$$

Assuming Curie's law as the equation of state, the heat of magnetization can be written

$$dq_T = -\mu_0 v c\frac{H}{T}\,dH. \tag{3.2.4}$$

Eq. (3.2.4) shows that for an isothermal field sweep of a given magnitude the heat of magnetization per unit mass of paramagnetic material will vary as the inverse of the temperature. This is an important result because to implement the linear temperature profiles of Chapter 2 in a working fluid whose specific heat falls with temperature (a zeroth order approximation for helium in this temperature range) requires that the magnetic heat input decreases with increasing temperature.

The idealized analysis also predicts that the temperature swings produced by an adiabatic magnetization should vary linearly with temperature for the cycle with linear temperature profiles. The temperature swing produced during an adiabatic magnetization cannot be predicted by the Curie law alone. Setting ds equal to zero in Eq. (3.2.2), the differential adiabatic magnetization temperature swing, dT_s, is calculated.

$$dT_s = \frac{-\mu_0 v T}{c_H}\left(\frac{\partial \mathcal{M}}{\partial T}\right)_H dH_s \tag{3.2.5}$$

The specific heat at constant field, c_H, is defined in Appendix 1 as the sum of two terms.

$$c_H = \left(\frac{\partial u}{\partial T}\right)_H - \mu_0 v H \left(\frac{\partial \mathcal{M}}{\partial T}\right)_H \tag{3.2.6}$$

Since for a paramagnetic material obeying Currie's law $(\partial u \ \partial H)_T = 0$ the specific heat at constant field $(\partial u \ \partial T)_H$ must be equal to the specific heat at zero field $(\partial u \ \partial T)_{H=0}$. Therefore the first term of Eq. (3.2.6) is the lattice specific heat. The second term represents the magnetic ordering at constant field due to change in temperature. If this term dominates (as it should for a magnetic refrigerant) then in the limit as $(\partial u / \partial T)_H \ll -\mu_0 v H (\partial \mathcal{M} \ \partial T)_H$ Eq. (3.2.5) approaches

$$dT_s \approx \frac{T}{H} dH_s. \tag{3.2.7}$$

The adiabatic magnetization temperature swing indicated by Eq. (3.2.7) depends linearly on temperature as predicted by the idealized analysis. The arguments of the preceding paragraphs, though not rigorous, indicate why the initial design selections of constant refrigerant mass per unit length and uniform magnetic field intensity seemed to be reasonable aproximations for further analysis.

Several over-simplifications were made in the preceding arguments. The magnetic properties of typical magnetic refrigerants are not well modeled by the Curie law which ignores saturation effects. Likewise, the assumption of a working fluid with a specific heat varying inversely with temperature is a poor model for helium in the temperature range of the refrigerator.

3.3 Specification of the Design

This section describes the variables required to specify the design of the system exclusive of the internal geometry of the regenerator core. The variables are organized into five groups based on the feature they describe: temperature profile, timing, working fluid, magnetic field, or external regenerator core geometry. A feasible set of design variables is selected based on design equations and restrictions.

The design equations are simple relations between the design variables based on the ideal analysis of chapter 2. The set of restrictions include refrigeration performance parameters, limitations imposed by the design of hardware, and limitations imposed by properties of the working fluid and the magnetic refrigerant.

Temperature Profile Variables

For the purpose of selecting the design variables, the temperature profiles have been idealized as linear as they were in Chapter 2. Fig. (3.3.1) shows the temperature profiles plotted versus axial position in the regenerator core.

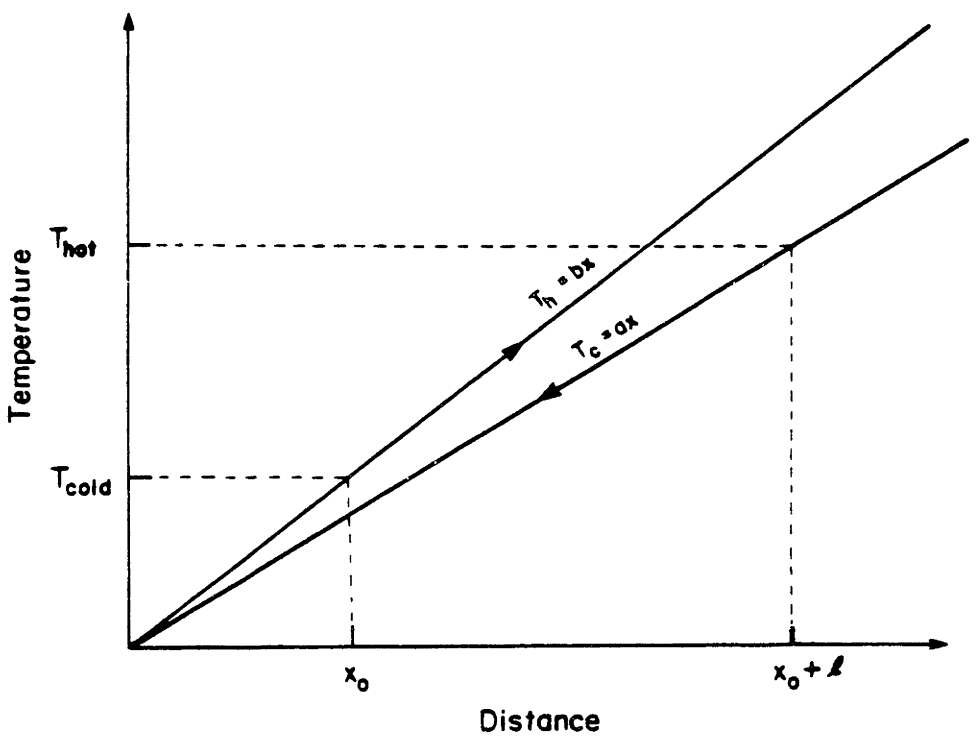

Fig. 3.3.1 Idealized temperature profiles in working fluid.

The temperature profile in the working fluid during a hot blow (mass flowing from the cold end to the hot end) is $T_h(x) = b\,x$ and $T_c(x) = a\,x$ is the temperature profile during a cold blow. The location x_0 corresponds to the cold end of the regenerator. Fluid entering the core at this location has the cold reservoir temperature. The location $x_0 + \ell$ is at the hot end of the core (fluid entering the core at this

location has the hot reservoir temperature). The design variable $\frac{a}{b}$ is defined as the isentropic temperature ratio. It represents the temperature swing at any axial location during an adiabatic process (subject to the idealizations of Chapter 2). The larger the ratio $\frac{a}{b}$, the greater the refrigeration for fixed shuttle mass and hot and cold resevoir temperatures. The temperature profiles are completely specified by the adiabatic temperature swing and the hot and cold reservoir temperatures T_{hot} and T_{cold}.

Timing variables

The refrigeration cycle consists of four processes: adiabatic demagnetization, isothermal demagnetization, adiabatic magnetization and isothermal magnetization. Fig. (3.3.2) shows the timing design variables τ_S, the time for an adiabatic process, and τ_T the time required for an isothermal process.

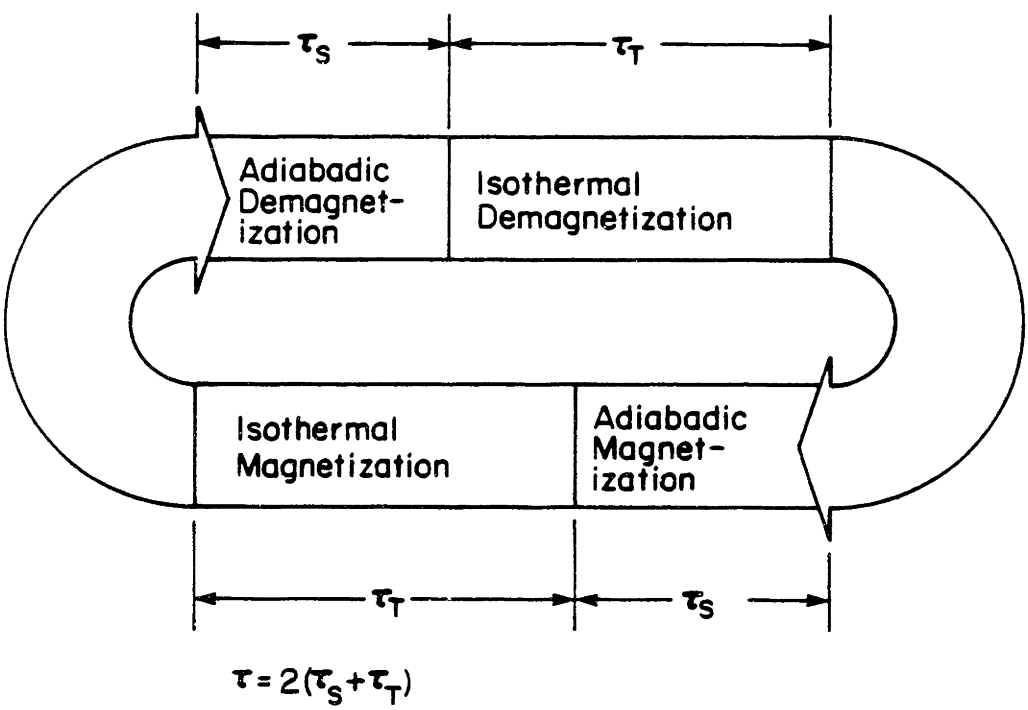

Fig. 3.3.2 Timing variables for active regeneration cycle

The processes are assumed to take the same amount of time whether they occur during magnetization or demagnetization. The total cycle time τ is related to the design variables τ_S and τ_T by the relationship $\tau = 2(\tau_S - \tau_T)$.

External core geometry.

The regenerator core is assumed to have a circular cross section of diameter D. The length of the core is defined ℓ. The internal flow passage geometry of the core will be specified in the last section of this chapter.

Magnetic field variables

The temporal variation in the spatially uniform magnetic field is shown in Fig. (3.3.4). The temporal field variation is specified by the design variables H_{max},the maximum field intensity, H_{min}, the minimum field, and $\dot{H}_{max}$ the maximum allowable field sweep rate. †
Linear temporal field variations are assumed because they are the simplest to implement and reduce the complexity of interpreting the experiments.

Working fluid variables

The working fluid for the experiment, helium, is described by two design variables m_s, the shuttle mass, which is the mass of helium which cycles through the core during either of the isothermal magnetic work interactions and P the nominal pressure of the system.

Selection of feasible set of design variables

Except for the internal geometry of the regenerator core the design is completely specified by the set of design variables: ℓ, D, $\frac{a}{b}$, τ_T, τ_S, H_{max}, H_{min}, $\dot{H}_{max}$, m_s,

† In MKS units the magnetic induction is defined by the equation $B = \mu_0(H + \mathcal{M})$ and has the units of tesla; H is the magnetic field intensity in Am^{-1}. It is common, though inaccurate, practice to express the magnetic field intensity as $\mu_0 H$ in tesla; to avoid confusion this thesis refers to field intensity in units of tesla.

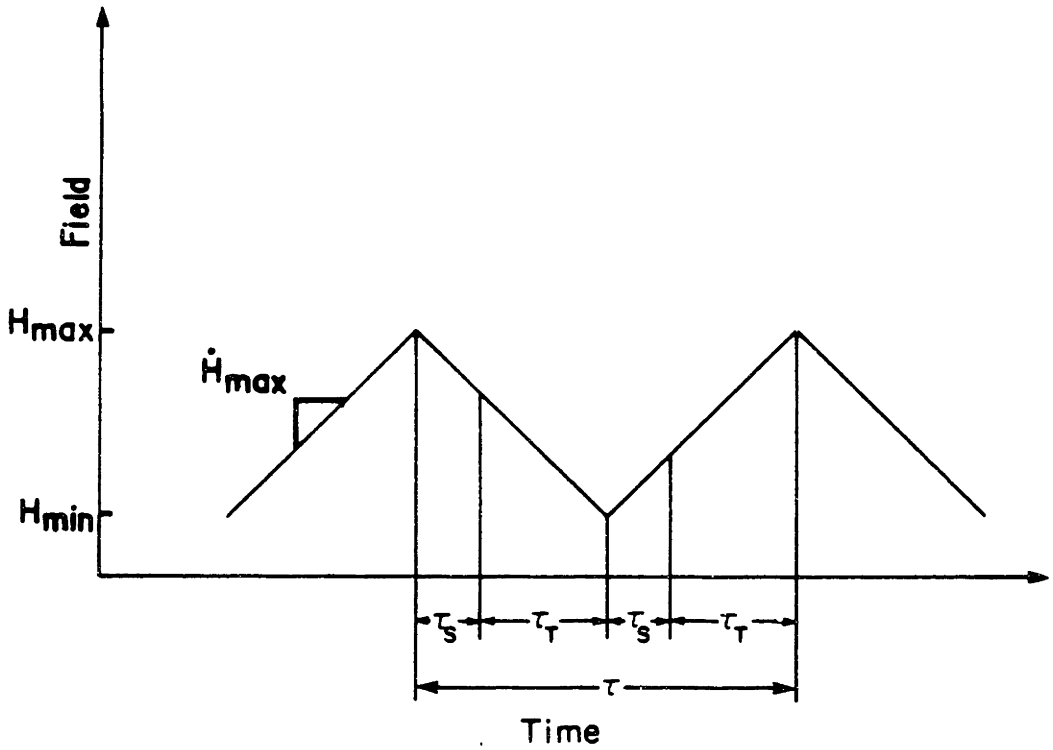

Fig. 3.3.4 Time dependence of magnetic field

P, T_{hot}, and T_{cold}. A feasible set of design variables meeting the performance parameters of the cycle can be ascertained by solving the design equations subject to the constraints. The performance parameters for this design are to provide 1.5 W of refrigeration to a 4.2 K load while rejecting heat to a 10 K sink. The constraints on the choice of variables rise from various sources: the design of the superconducting magnet, the size of the cryostat, the fluid properties, and the properties of the magnetic refrigerant.

Superconducting magnet

The design and construction of the superconducting solenoid imposed constraints on, H_{max}, $\dot{H}_{max}$, and the diameter of the regenerator core, D. The following specifications were selected: maximum bore 38 mm diameter, maximum field 4 T, and maximum sweep rate 0.5 Ts^{-1}. These figures were suggested as reasonable limits for an AC magnet to avoid the possibility of quenching, to be fabricated rea-

sonably inexpensively with commercially available superconductor, to be contained in a dewar no larger than 22 cm in diameter, and to provide acceptable AC loss. The last criterion is meant only to keep the helium consumption at a level which will allow economical operation of the experiments. The magnet for this experiment was not designed to produce losses small compared with the refrigeration power of the device. The detailed design of the magnet is provided in Appendix 2.

Fluid properties

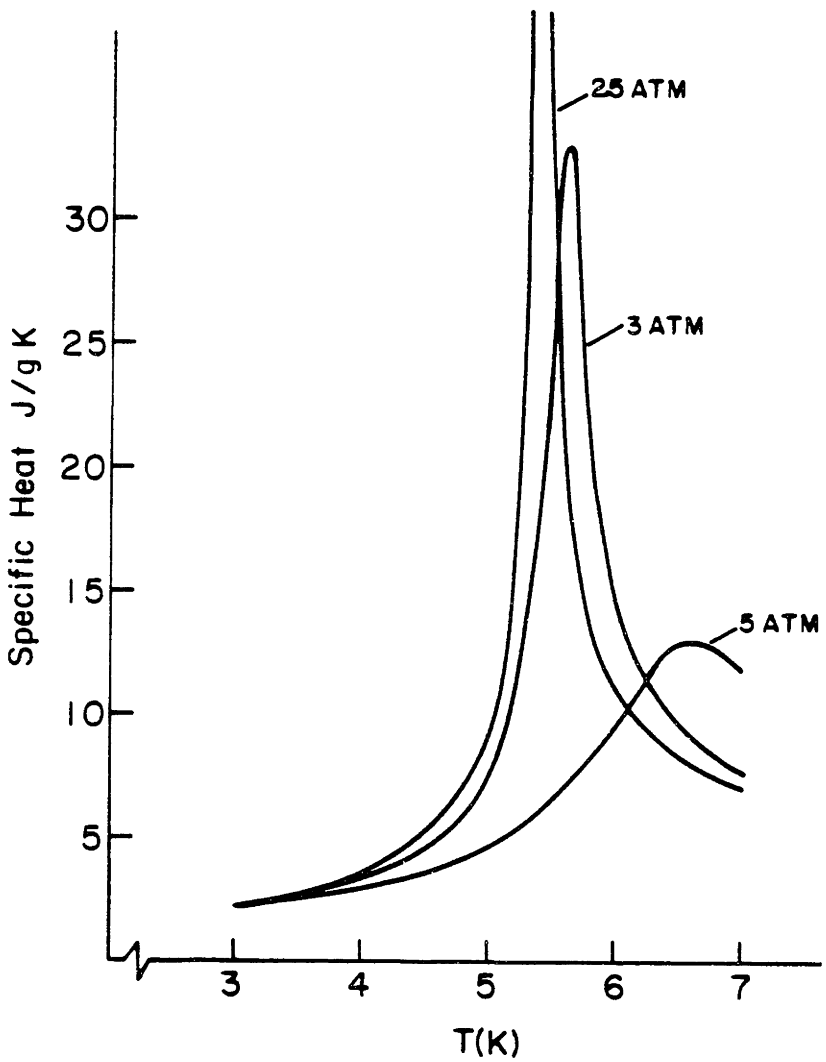

Fig. 3.3.5 Specific heat at constant pressure for helium

The pressure of the working fluid also constrains the design. Fig. (3.3.5) shows

helium's specific heat at constant pressure plotted against temperature for various isobars.In order to avoid two-phase flow in the regenerator core it was decided to operate the working fluid in the supercritical state. The higher the pressure the more uniform the specific heat becomes in the temperature span of the experiment. High working pressure of the helium mandates strong heavy construction in the gas handling equipment. Heavy construction in cryogenic equipment leads to unacceptable axial conduction heat leak. The increase in density at higher pressure causes greater entrainment losses in the regenerator core as will be explained in section 3.5. Three atm was chosen as the working pressure as a compromise between helium properties and manufacturing difficulties.

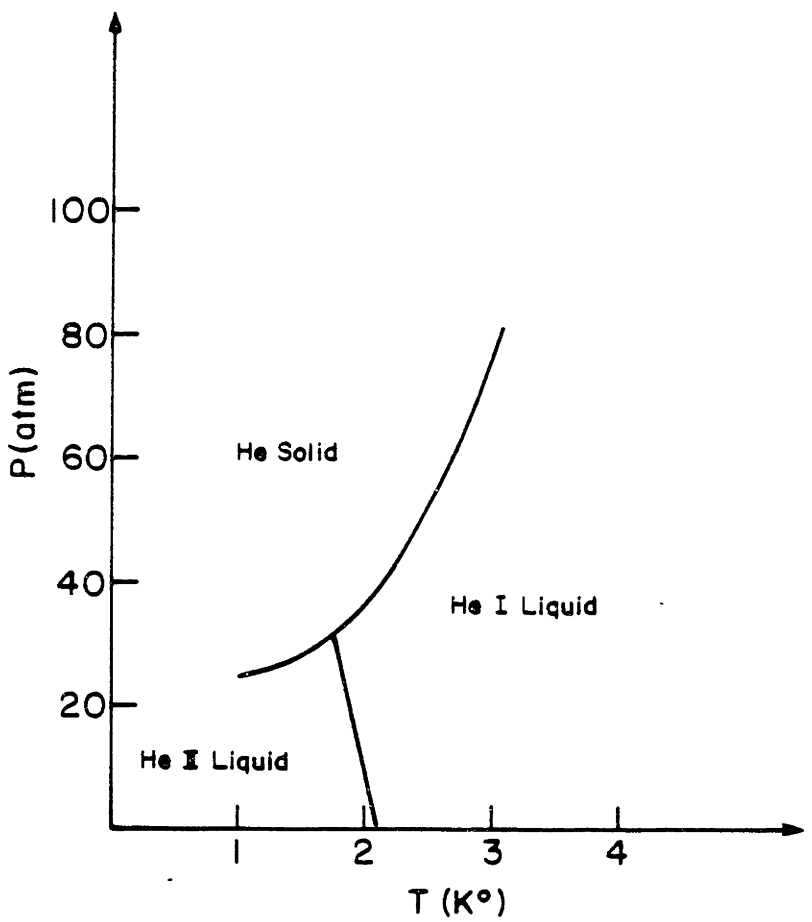

Fig. 3.3.6 Phase diagram for ^{4}Helium

The λ transition of helium imposes another constraint on the design. Fig.

(3.3.6) shows a phase diagram for the isotope ^{4}Helium. ^{4}He undergoes a second order phase change at approximately 2.1 K to the superfluid phase. A logarithmic singularity in helium specific heat is associated with this phase change and the transport properties are discontinuous at the phase boundary. In order to avoid complications involving HeII it was decided to keep all temperatures in the regenerator core above the λ transition by designing for a cold blow cold end temperature $T_c(x_0)$ of 2.8 K.†

Properties of the magnetic refrigerant

The specification of the design requires the selection of a particular magnetic refrigerant. gadolinium-gallium-garnet ($Gd_3 Ga_5 O_{12}$), the best known magnetic refrigerant for the temperature range from 2 to 20 K, was chosen for this design. A magnetic refrigerant should have an ordering temperature below the lowest temperature of the refrigeration cycle; GGG has an ordering temperature below 1 K. The material should have a large ordering resulting from the application of magnetic field because the magnetic entropy is a measure of the power density of the material. A magnetic refrigerant should have a small lattice specific heat so that the maximum magnetic effect is available for refrigeration and not absorbed by the thermal inertia of the lattice. High thermal conductivity is important to maintain a uniform temperature in the bulk refrigerant. References (17-21) discuss the properties of various magnetic refrigerants. Mechanical properties of the magnetic refrigerant are also important. It is important that the material be stable chemically and suitable for processing to the geometric configuration desired.

Fig. (3.3.7) is a temperature-entropy diagram for the magnetic refrigerant GGG. The close spacing of the 0 T and 1 T isofields indicates that the quantity $T(\partial s/\partial H)_T$ is small between these field intensities. Since $T(\partial s/\partial H)_T$ represents the cooling power of the refrigerant, it was decided to avoid using field intensities below 1 T in the experiment. The properties of the magnetic refrigerant GGG were used to select the partitioning of the cycle time into adiabatic and isothermal processes. A Carnot cycle was fit onto the T-S diagram for GGG coresponding to

† Diluting ^{4}He with the isotope ^{3}He supresses T_λ to lower temperatures

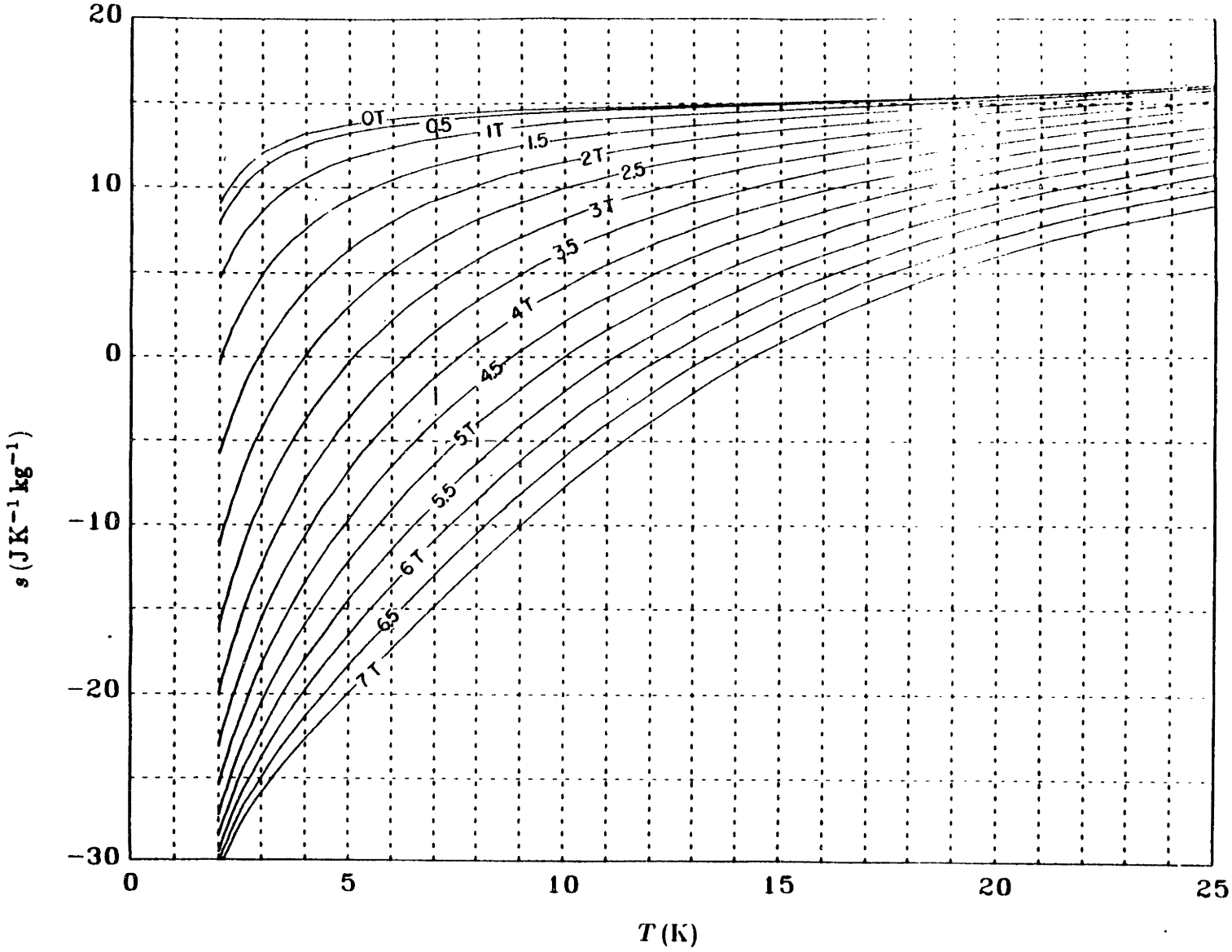

Fig. 3.3.7 Temperature-Entropy Diagram for GGG

the coldest end of the regenerator core. The maximum refrigeration is achieved for the lowest cold temperature, 2.8 K, and the largest magnetic field swing, 1 T-4 T, allowed by the constraints.

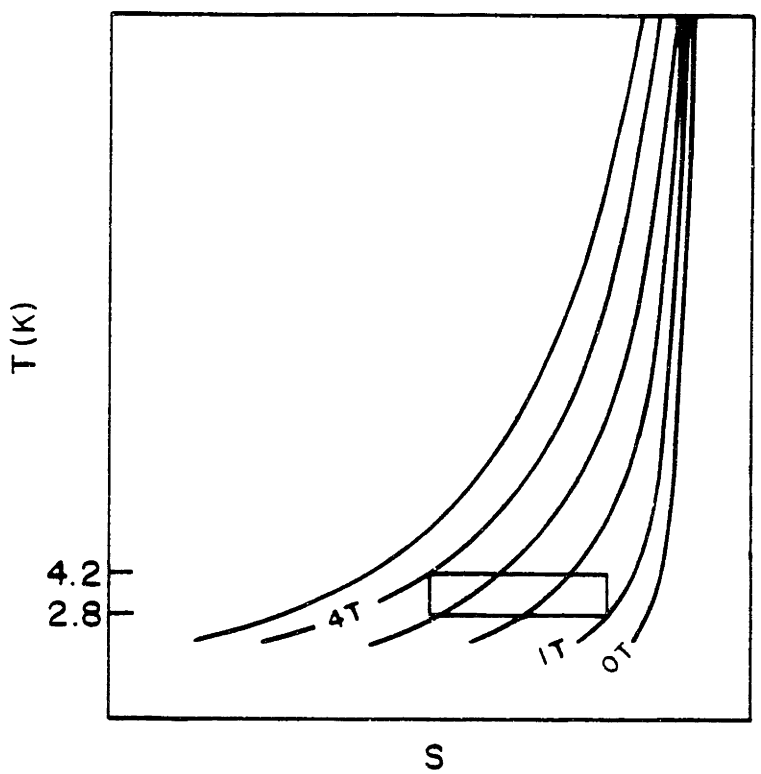

Fig. (3.3.8) Carnot cycle at cold end of regenerator

An adiabatic temperature swing from 4.2 K to 2.8 K initialized at 4T requires approximately 0.75 T. This leaves 2.25 T for the isothermal process. Since a uniform sweep rate is assumed the cycle time must be partitioned in the same manner as the field. This requires that the time for an isothermal process be three times the time for an adiabatic one. Fig. (3.3.2) shows that $\tau = 2\,(\tau_T + \tau_S)$. Therefore $\tau_T = 3/8\,\tau$ or equivelently $\tau_S = 1/8\,\tau$.

The remaining design variables, τ the total cycle time, m_s the shuttle mass, and ℓ the regenerator core length can now be calculated using the idealized equations

of chapter 2.

Period of cycle

The refrigeration power is the net efflux of enthalpy from the cold end per cycle divided by the total cycle time.

$$\text{Refrigeration power} = \frac{m_s}{t}(h_{out} - h_{in}) \tag{3.3.1}$$

Assuming the cold blow temperature remains constant at 2.8 K and that during the hot blow helium enters the core from a reservoir fixed at 4.2 K, the shuttle mass divided by the total cycle time m_s/τ can be solved. Assuming that the magnet is always ramped at its maximum design rate, $\dot{H}_{max}$ between the limits imposed on the field by H_{max} and H_{min}, the total cycle time can be solved from the simple geometry of Fig. (3.3.4)

$$\tau = 2\left(\frac{H_{max} - H_{min}}{\dot{H}_{max}}\right) = 12\,\text{s}. \tag{3.3.2}$$

Because mass flow only takes place during the isothermal processes the actual mass flow rate for either isothermal processes is given by m_s/τ_T and will be assumed constant throughout the flow process. This choice is made for greater ease of design and experimentation. It is not the ideal choice for refrigeration performance because the internal heat generation term $T(\partial s/\partial H)_T$ for the magnetic refrigerant is field-dependent thus producing unsteady effects in the temperature for a constant-mass-flow, uniform-field-sweep-rate process. The actual mass flow, m_s/τ_T, is found using the known values of m_s and τ and the relationship $\tau_T = 3/8\,\tau$.

Regenerator core length

The final design variable to be selected is the length of the regenerator core ℓ. The length of the regenerator core required is estimated by an entropy balance for a flow process assuming steady reversible heat transfer between magnetic refrigerant and helium and neglecting the mass of helium in the void space. Fig. (3.3.9) shows the control volume used to formulate the equation.

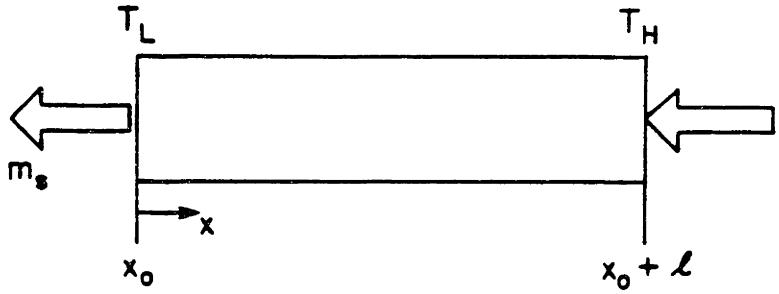

Fig. 3.3.9 Control volume used for estimating ℓ

The reversible entropy balance for the control volume is

$$\int_{x_0}^{x_0+\ell} \rho_{GGG} \frac{\pi D^2}{4} \overline{\dot{s}_{mag}}\,|_T \; dx = \frac{m_s}{\tau_T}(s_{out} - s_{in})_{He} \tag{3.3.3}$$

The quantity $\overline{\dot{s}_{mag}}\,|_T$ is the isothermal entropy sweep for GGG averaged both by field (from 1 to 4T) and by temperature (2.8 to 10K) using the data from Fig. (3.3.7).

$$\overline{\dot{s}_{mag}}\,|_T = \frac{1}{\tau_T} \frac{1}{T_c(x_0+\ell) - T_c(x_0)} \int_{T_c(x_0)}^{T_c(x_0+\ell)} \frac{1}{H_{high} - H_{low}} \int_{H_{low}}^{H_{high}} \left(\frac{\partial s}{\partial H}\right)_T dH\, dT \tag{3.3.4}$$

The design calculations were performed with a crude estimate of $\overline{\dot{s}_{mag}}\,|_T$ averaged at only three different temperature locations. The entropy swing for the complete field swing was calculated at 4.2 K, 5.5 K, and 10 K. These entropies were then averaged and the result divided by τ_T to approximate $\overline{\dot{s}_{mag}}\,|_T$.

To calculate ℓ Eq. (3.3.3) is integrated. Because none of the factors in the integral depend on position, the length can be solved for by simple division.

$$\ell = \frac{m_s}{\tau_T}\left(\frac{s_{He}(10\,\mathrm{K},3\,\mathrm{atm}) - s_{He}(2.8\,\mathrm{K},3\,\mathrm{atm})}{\rho_{GGG}\frac{\pi D^2}{4}\overline{\dot{s}_{mag}}\,|_T}\right) \tag{3.3.5}$$

The material properties, hardware limitations, and performance parameters discussed in the previous paragraphs have specified the following design variables. The adiabatic temperature ratio, $\frac{a}{b}$, was determined by the cold reservoir temperature and the minimum working fluid temperature to be 1.5. Three atm was selected

Table (3.3.1) Design Variable Assignments

Variable	Definition	Value [units]	Eqns.	Constraints
a/b	adiabatic temp ratio	1.5		T_λ, T_{cold}
t_T	isothermal process time	4.5 s	3.3.2	$H_{max}, H_{min}, \dot{H}_{max}$, GGG
t_s	adiabatic process time	1.5 s	3.3.2	$H_{max}, H_{min}, \dot{H}_{max}$, GGG
m_s	shuttle mass		3.3.1	$t_T, T_{cold}, a/b$
$\dot{H}_{max}$	max sweep rate	$0.5\,\mathrm{T\,s^{-1}}$		magnet
H_{max}	max field	4 T		magnet
H_{min}	min field	1 T		magnet
ℓ	core length	27.0 cm	3.3.5	m_s, GGG
D	core diameter	3.8 cm		magnet
P	working pressure	3 atm		Helium properties

as the working pressure, P, as a compromise between helium properties and hardware design. The core diameter (D=3.8 cm), the maximum magnetic field strength (H_{max}= 4 T), and the maximum field sweep rate ($\dot{H}_{max}$ = $0.5\,\mathrm{Ts^{-1}}$), were determined by the magnet design limitations. The properties of the magnetic refrigerant, GGG, selected the ratio of isothermal to adiabatic process times as 3:1. The design variables τ, m_s, and ℓ were solved using the idealized design equations of Chapter 2. Table (3.3.1) shows the complete list of design variables, their values, and the equations and constraints used to derive them. Although the calculated length of

the regenerator core is 27.0 cm, it was decided to construct the core 30.5 cm long.

3.4 Specification of the internal geometry of the regenerator core

The performance of the design specified in section 3.3 has been numerically simulated by Gallagher[22]. His transient simulation invokes the actual thermodynamic properties of the working fluid and the magnetic refrigerant. Gallagher's analysis only considers irreversibilies generated by stream-to-wall temperature differences. This section will demonstrate that the regenerator core geometry can be selected so that other losses are of secondary importance.

The loss mechanisms which detract from the ideal performance are introduced and discussed in conjunction with three possible configurations for the regenerator core: packed bed, parallel tube, and parallel plate. Parallel plate configuration is selected as the best geometry to provide the small dimension flow passages and low porosity mandated to minimize the loss mechanisms in an easy-to-fabricate package. The variables describing the parallel plate geometry are selected based on the criteria of loss minimization and practicality. The final portion of this section reviews how the actual core compares with the idealization of the previous sections.

Loss mechanisms

The losses considered in the design of the regenerator core were axial conduction of heat through the core, loss of net refrigeration due to entrainment of helium and other non-active materials in the core, generation of entropy through fluid friction between the working fluid and the flow passages, irreversible heat transfer due to temperature gradients within the GGG and at the fluid-GGG interface. Other losses considered in the design of the overall refrigerator system are AC loss in the superconducting solenoid, and heat leaks from the regenerator core to the environment. These losses will be discussed in Chapter 4 in conjunction with the experimental apparatus.

Entrainment

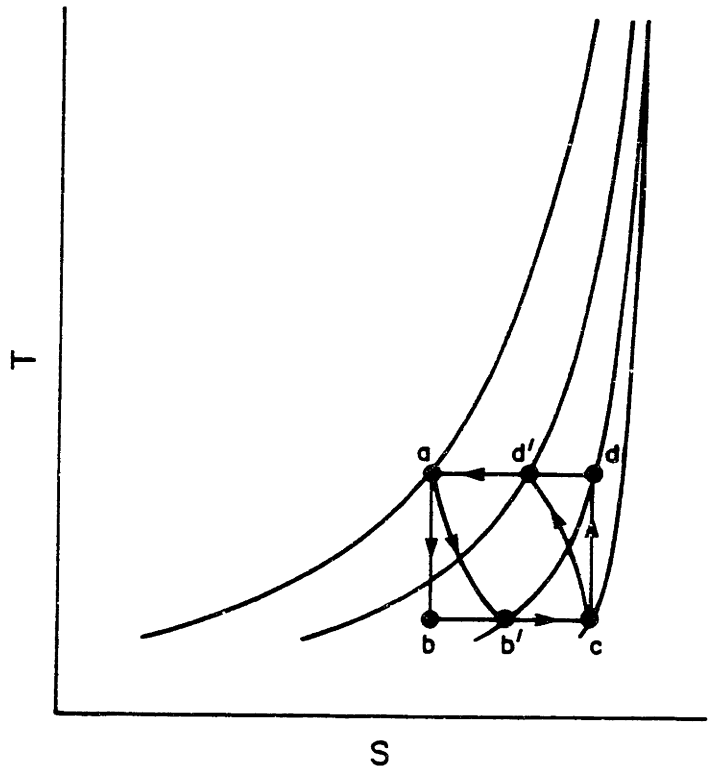

Fig. (3.4.1) Effect of entrainment on Carnot cycle capacity

The loss of performance associated with entrained helium is important and must be described in greater detail before examining the specific core configurations. The presence of entrained helium in the core reduces the capacity of the cycle, yet it need not generate entropy. Fig. (3.4.1) shows a magnetic Carnot cycle on a T-S plot of the refrigerant.

The entrained helium (helium in the void space of the regenerator core) remains in thermal communication with the GGG continually, thereby preventing the refrigerant from undergoing an adiabatic process. Entropy is transferred out of the refrigerant into the entrained helium on an "adiabatic" (nonflow) magnetization and from the helium to the GGG on an "adiabatic" demagnetization. The result, for a fixed temperature span and magnetic field span, is the isothermal en-

tropy swing for a cycle without entrainment (segments bc or da on Fig. (3.4.1)) is reduced (segment b'c or d'a). The isothermal entropy swing determines the cooling power of the cycle. The loss of isothermal entropy swing and therefore refrigeration power is present even if the heat transfer between the salt and helium is reversible.

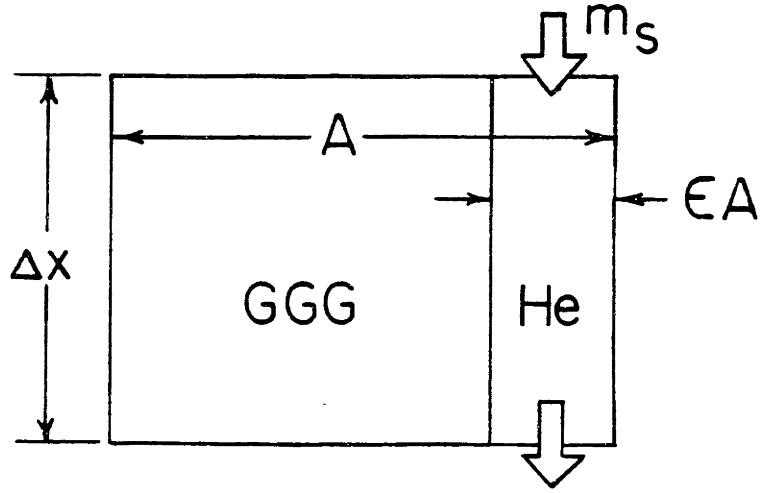

Fig. (3.4.2) Magnetic refrigerant and entrained helium

To quantify the effects of entrainment consider the system of helium and GGG in Fig. (3.4.2) executing the Carnot cycle of Fig. (3.4.1). Consider an adiabatic magnetization process for the combined system with helium and salt in mutual stable equilibrium. A temperature swing of ΔT from T_i to T_f requires that a quantity of entropy $\Delta S_{mag_{nonflow}}$ is transferred to the helium (segment d-d').

$$\Delta S_{mag}\,|_{nonflow} = \rho \epsilon A c_p \ln \frac{T_f}{T_i} \Delta x \tag{3.4.1}$$

In Eq. (3.4.1) ρ and c_p refer to the density and specific heat of the helium. The porosity ϵ is defined as the ratio of flow passage cross-sectional area to total cross-sectional area (note that for the case of uniform regenerator core geometry the porosity could also be defined as the ratio of the void volume to the total volume). This entropy transfer reduces the available isothermal entropy swing. The isothermal entropy swing without entrainment effects $\Delta S_{mag}\,|_T$ (segment d-a) can be approximated in terms of the shuttle mass m_s and the local helium specfic heat and temperature gradient during a flow process.

$$\Delta S_{mag}\ |_T = m_s \frac{c_p}{T} \frac{dT}{dx} \Delta x \tag{3.4.2}$$

The ratio of the entrained helium entropy swing to the isothermal entropy swing is a dimensionless number which indicates the amount of refrigeration power lost to helium entrainment.

$$\frac{\Delta S_{mag\ \ nonflow}}{\Delta S_{mag\ \ T}} = \frac{\rho \epsilon A \ln \frac{T_f}{T_c}}{m_s \frac{dT}{dx} T} \tag{3.4.3}$$

The entrainment ratio expressed by Eq. (3.4.3) can be estimated for any particular location in the regenerator core using the design variables selected in the previous section. The importance of this loss mechanism is illustrated by the following example: If the maximum degradation of refrigeration power acceptable is 5% then the evaluation of Eq. (3.4.3) at the cold end indicates that a maximum porosity of $\epsilon = 0.028$ could be tolerated.

Bed configurations

To evaluate the effect of manufacturing limitations on the loss mechanisms it is necessary to consider specific geometries. Three refrigerant core configurations were examined in detail: packed bed, parallel tube, and parallel plate. The first two geometries proved unsuccessful because of anticipated difficulties to meet the criteria of acceptable losses and manufacturability. These configurations will be briefly discussed before turning to the detailed design of the parallel plate regenerator core.

Packed bed

The simplest regenerator core to construct is a packed bed. In this configuration axial conduction is small because of the contact resistance of the many granuals. To analyze the packed bed it was modeled as a close packed array of spheres of uniform diameter D (Fig. (3.4.3)).

Nusselt number and friction factor corelations for packed beds can be found in the literature[23]. The packed bed was not chosen for this application because of its

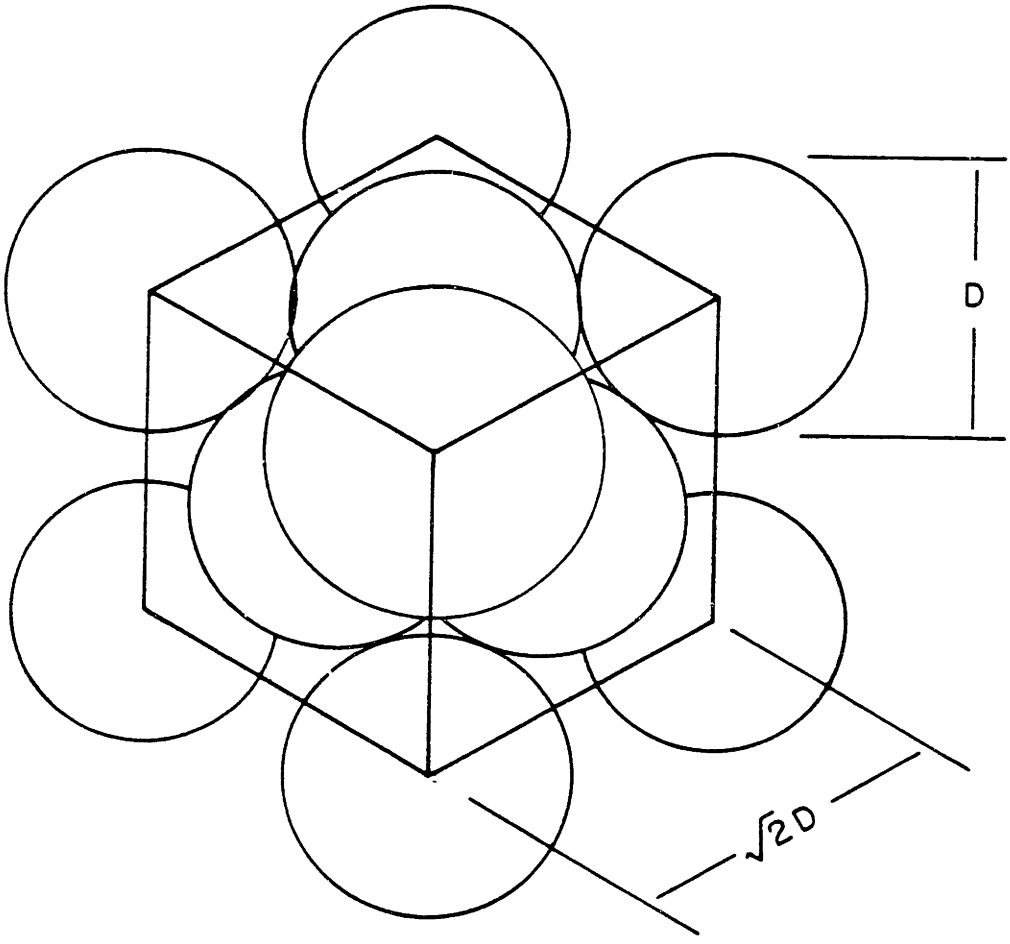

Fig. (3.4.3) Model of packed bed

relatively high porosity. The theoretical porosity for a close packed bed of uniform spheres is 26%, which causes unacceptable entrainment losses. If a fcc matrix is assumed, the reduction in porosity resulting from filling the octahedral interstices with smaller spheres can be calculated. The porosity for the filled fcc matrix is 21% which still has unacceptable entrainment. These calculations are based on contrived models. Typical actual porosities for packed beds of random spheres are on the order of 35%[23].

One possible solution for reducing the porosity of the packed bed is hot isostatic pressing. Hot isostatic pressing subjects the packed bed to large external pressure at temperatures above the recrystalization point resulting in compaction of the

matrix to any required porosity. Sintered bronze filters are examples of matrices formed in this way. Isostatic pressing has the advantage of fixing the packed bed in a contiguous unit eliminating the problems of tunneling and shifting associated with loose packed beds. Unfortunately, the resulting relationship between pressure drop and heat transfer coefficient is unknown and would have to be determined by experiment. It was feared that at the low porosities required the core might be completely occluded.

Parallel tube

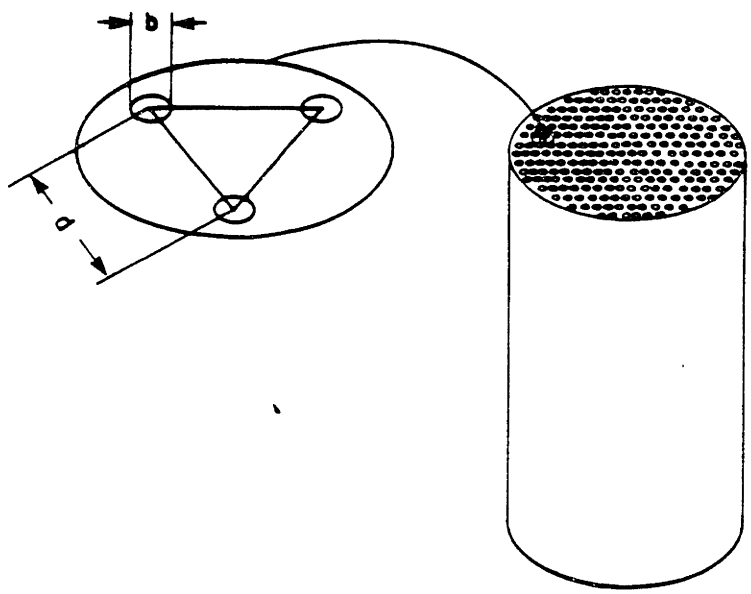

Fig. 3.4.4 Parallel tube core geometry

The parallel tube core design (Fig. (3.4.4)) is a series of tubular passageways spaced on vertices of an equalateral triangular grid. The characteristics of this geometry are described by d the hole diameter, and b the hole spacing. The 60° array was chosen because it minimizes the transverse temperature gradients caused by conduction of heat through the magnetic refrigerant. The porosity of this configuration is a function of d/b; this means that the characteristic size (represented by

either d or b) and therefore the transport properties can be varied at constant ϵ. Two drawbacks of the parallel tube core are axial conduction through the core and manufacturing complexity.

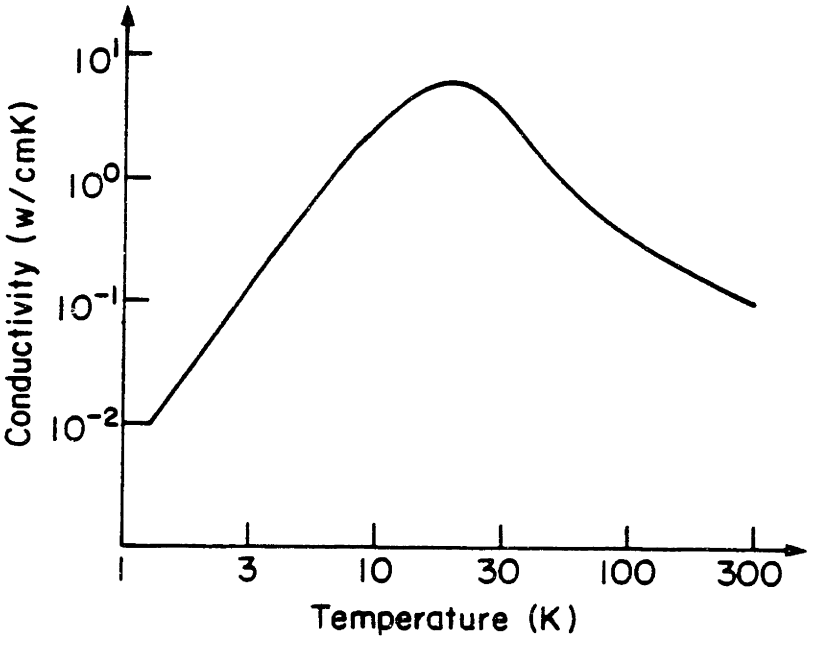

Fig. 3.4.5 Thermal Conductivity of GGG

Axial conduction through the parallel tube core was first estimated by assuming a single crystal 3.8 cm in diameter and 30 cm long (specified by Table (3.3.1)) connecting the 10 K and 4 K reservoirs. Fig. (3.4.5) shows the thermal conductivity for GGG plotted versus temperature. The conductivity can be approximately related to the temperature in the range from 2-20 K by the following equation[24].

$$k_{GGG} = 0.596\,T^{2.84}\ \mathrm{W\,m^{-1}\,K} \tag{3.4.4}$$

The axial conduction through the solid GGG core can be found by integrating the Fourier equation between the appropriate boundaries.

$$\int_0^{0.3\,\mathrm{m}} \dot{Q}\,dx = \int_{4.2\,\mathrm{K}}^{10\,\mathrm{K}} k(T)A\,dT \tag{3.4.5}$$

The resulting conduction calculated is 3.9 W To reduce the axial heat leak to an acceptable level it was proposed that the parallel tube core be constructed as a composite of GGG wafers interleved with thin discs of a low conductivity thermal barrier material (Fig. (3.4.6)).

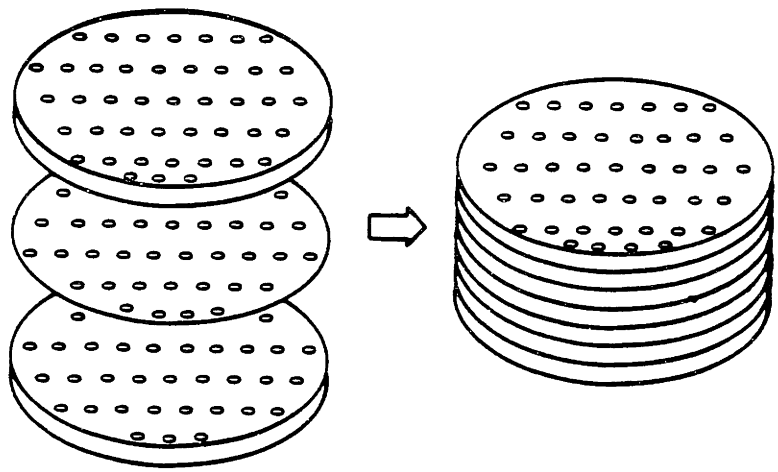

Fig. 3.4.6 Composite construction of parallel tube core

Just as with the effects of entrained helium, the heat capacity of the thermal barriers must be held to a minimum to avoid degrading refrigeration performance. Fig. (3.4.7) shows a model for evaluating the performance of the thermal barriers.

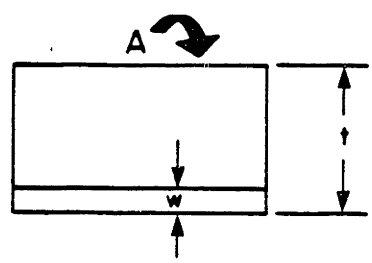

Fig. (3.4.7) Interleved GGG and thermal barriers

A unit cell of the composite of total thickness t contains a thermal barrier of thickness w and thermal conductivity k_B. The quantity ϵ is defined as the ratio w/t and

represents the ratio of barrier volume to total volume. The thermal resistance of the unit cell is

$$\frac{t-w}{k_{GGG}} + \frac{w}{k_B}. \tag{3.4.6}$$

The effect of the contact resistance between the barrier material and the GGG wafers is neglected. If it is assumed that $w \ll t$ then Eq. (3.4.6) can be simplified.

$$\frac{t(k_B - \epsilon k_{GGG})}{k_B k_{GGG}} \tag{3.4.7}$$

Finally, if the core is finely divided into many cells, then in the limit, the conduction can be expressed by an integral.

$$\int_0^{\ell} \frac{\dot{Q}}{A} dx \int_{T_C}^{T_H} \frac{k_{GGG} k_B}{\epsilon k_{GGG} + k_B} dT \tag{3.4.8}$$

The thermal boundary material was assumed to be Nylon for the purpose of this estimate. Eq. (3.4.9) approximates Nylon's conductivity between 4 and 10 K[25].

$$k_B = 0.0017\, T^{1.36}\ \mathrm{W\,m^{-1}\,K^{-1}} \tag{3.4.9}$$

If the ratio of barrier material to magnetic refrigerant is assumed to be 5%, the axial conduction through the core is reduced to 0.01 W.

The rough design for the tube core called for 0.08 mm holes on 0.37 mm centers. Three ideas for fabrication of such wafers were considered: conventional drilling of the holes using some form of numerically controlled machine, laser drilling using a numerically controlled YAG laser, or casting the core about thin wires then sawing into discs and then etching out the wires to form the holes. Conventional drilling was ruled out immediately because of the small size and high precision required. Laser drilling was attractive because the high pulse speed of the laser could machine the discs rapidly. Laser drilling was rejected because of the high cost and the tendency for laser drilled holes to taper and blow out on the back side (like a BB hole in glass). The third approach was never given serious consideration because of its great complexity and the lower thermal conductivity of cast GGG.

Regardless of how the hole pattern was created in the discs, assembly of the individual discs into the complete core would be difficult. One source of difficulty in the assembly is the high accuracy required to line up the holes in adjacent discs. A second assembly problem is how to bond the thermal barrier pieces to the discs without obstructing the flow passages. The parallel tube core design was rejected because of the difficulties anticipated in its construction.

Parallel plate geometry

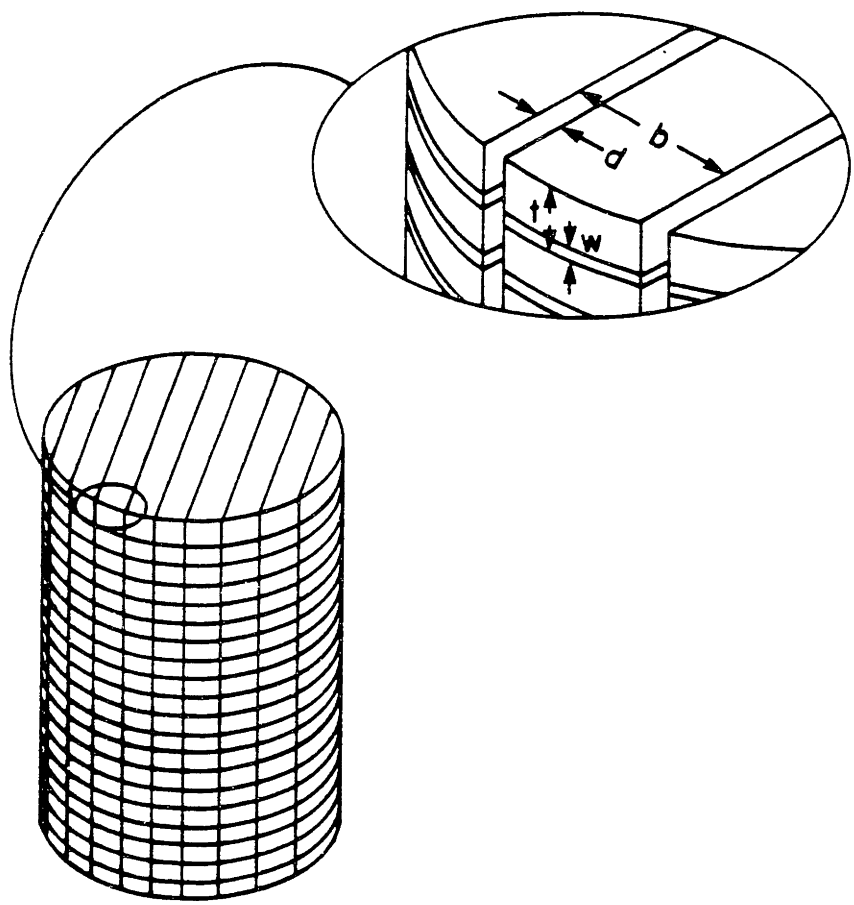

Fig. (3.4.7) Parallel plate core

Fig. (3.4.7) shows the parallel plate geometry. Parallel channels of width d are separated by a distance b. The parallel plate core, like the parallel tube core, requires the presence of thermal barriers of thickness w separated by distance t to

maintain axial conduction at an acceptable level. Although simpler to fabricate than the parallel tube core, the parallel plate core also allows independent variation of the porosity and the channel width.

Construction of the parallel plate core starts with a series of GGG wafers which are bonded together with thin discs of thermal barrier material between them. Next, the composite cylinder is sawn lengthwise into parallel slabs which are then reassembled into a cylinder with thin spacers separating them on the edges to provide the parallel flow passages. Appendix 3 explains in detail the fabrication of the core.

The complete internal geometry of the parallel plate regenerator core is specified by the four variables t,w,d,b. The variables were selected to minimize the applicable loss mechanisms subject to the author's interpretation of reasonable construction limitations. The dimensions t and w determine the amount of axial conduction, the entrainment loss due to barrier material, and in part the fluid-to-wall heat transfer loss. The other two dimensions, d and b, control the fluid friction loss, the amount of helium entrainment, and share in the determination of the fluid-to-wall heat transfer irreversibility. The coupling between the two sets of variables is the fluid to wall heat transfer, d and b, determine the magnitude of the heat transfer coefficient, but t and w determine how efficiently it is used. This independence of function allows the variables to be selected in two separate groups.

Selection of d and b

The channel width d, and the channel spacing b, might vary at different locations within the core in an optimal design. However, to simplify the construction of the experiment, uniform slot width and spacing are used. The loss of refrigeration performance due to helium entrainment was discussed earlier and quantified by Eq. (3.4.3), subject to the approximations of mutual equilibrium and linear temperature profiles.

$$\frac{\Delta S_{mag}\,|_{nonflow}}{\Delta S_{mag}\,|_{T}} = \frac{\rho \epsilon A \ln \frac{T_f}{T_i}}{m_s \frac{dT}{dx}/T} \tag{3.4.3}$$

The porosity ϵ of the core shown on Fig. (3.4.7) is approximated by d/b for b much smaller than the core diameter. It was decided to limit the refrigeration loss due to entrainment calculated by Eq. (3.4.3) to 10%. This requires that ϵ is kept below 4%. The second equation used to determine the values of d and b comes from trading off the losses due to fluid friction and heat transfer.

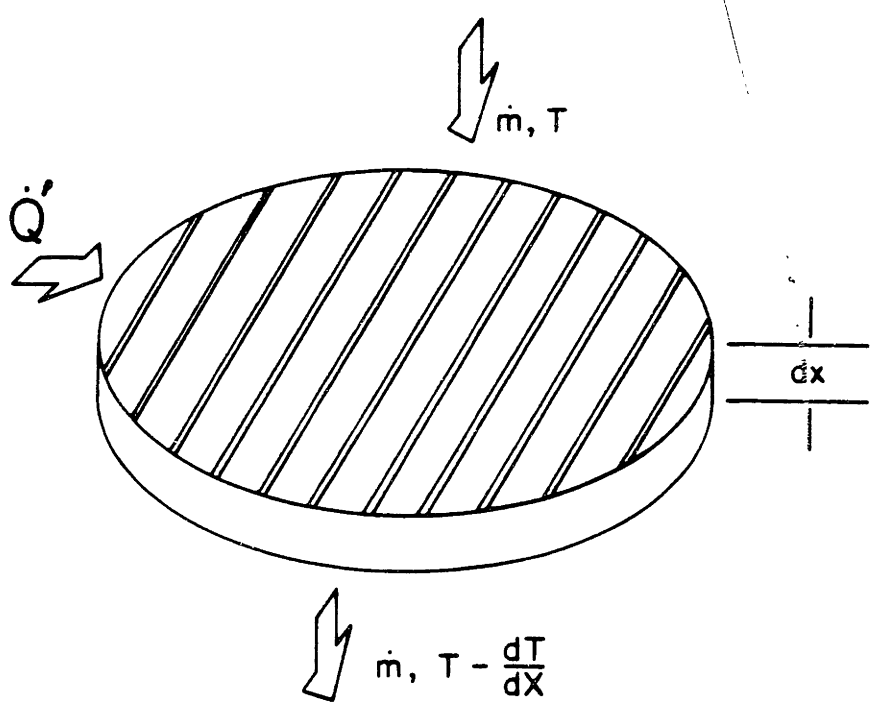

Fig. 3.4.8 Differential Section of Regenerator Core

Fig. (3.4.8) shows a regenerator core section of differential length with a helium stream of $\dot{m}$ flowing through it. The energy balance for the stream is

$$\dot{m}\frac{dh}{dx} = \dot{Q}'. \tag{3.4.10}$$

The rate of heat transfer per unit length is $\dot{Q}'$ and h is the enthalpy of the stream. The entropy balance for the stream, assuming it is being heated, follows.

$$\dot{m}\frac{ds}{dx} - \frac{\dot{Q}'}{T + \Delta T} = \frac{d\dot{S}_{irr}}{dx} \tag{3.4.11}$$

In Eq. (3.4.11), T is the local stream temperature, ΔT is the stream-to-wall temperature difference, s is the stream entropy and $\dot{S}_{irr}$ is the rate of entropy generation. The next equation is the $T\,ds$ relation for the stream in terms of enthalpy.

$$\frac{ds}{dx} = \frac{1}{T}\frac{dh}{dx} - \frac{1}{\rho T}\frac{dP}{dx} \tag{3.4.12}$$

In Eq. (3.4.12), P is the pressure and ρ is the density. Equations (3.4.10-12) can be combined to express the entropy generation rate in terms of the pressure gradient, the heat flux rate, and the stream-to-wall temperature difference.

$$\frac{d\dot{S}_{irr}}{dx} = \dot{Q}'\left(\frac{1}{T} - \frac{1}{T+\Delta T}\right) - \frac{\dot{m}}{\rho T}\frac{dP}{dx} \tag{3.4.13}$$

The heat flux rate $\dot{Q}'$, and the stream-to-wall temperature difference ΔT, are related by the heat transfer rate equation.

$$\dot{Q}' = \hbar\alpha\Delta T \tag{3.4.14}$$

In Eq. (3.4.14), $\hbar$ is the convective heat transfer equation and α is the heat transfer area per unit length. Equations (3.4.13) and (3.4.14) can be combined to give a single equation:

$$\frac{d\dot{S}_{irr}}{dx} = \hbar\alpha\left(\frac{\Delta T^2}{T(T+\Delta T)}\right) - \frac{\dot{m}}{\rho T}\frac{dP}{dx}. \tag{3.4.15}$$

The next step is to specify the transport properties of the core in terms of the variables d and b. The pressure gradient for fully developed, laminar, constant property flow in the parallel plate regenerator core can be expressed in terms of d and ϵ,

$$\frac{dP}{dx} = -\frac{3\pi\dot{m}\mu}{2\rho R^2\epsilon d^2}, \tag{3.4.16}$$

where, μ and ρ are the viscosity and density of the working fluid, and R is the radius of the core.

The estimation of the heat transfer involves some assumptions about the variables t and w. If t and w are chosen correctly, axial conduction will be negligible and the heat transfer condition will be best approximated by constant wall flux.

$$\hbar = 4.1\frac{k}{d} \tag{3.4.17}$$

The property k is the conductivity of the helium stream. The heat flux is related to the isothermal magnetic entropy swing by a simple energy balance.

$$\dot{Q}' = \hbar\alpha\Delta T = (T - \Delta T)\overline{\dot{s}_{mag}}\rho_{GGG}(1-\epsilon)A \tag{3.4.18}$$

The heat transfer area per unit length α can be expressed in terms of d and ϵ for the parallel plate regenerator core.

$$\alpha = \frac{16R^2\epsilon}{\pi d} \tag{3.4.19}$$

Substitution of equations (3.4.16-19) into Eq. (3.4.15) expresses the entropy generated during a flow process due to pressure drop and fluid to wall heat transfer in terms of ϵ and d.

$$\frac{d\dot{S}_{irr}}{dx} = \frac{\pi^3(\overline{\dot{s}_{mag}}\rho_{GGG}(1-\epsilon)Rd)^2}{65.1k^2\epsilon} + \frac{3\pi\dot{m}^2\mu}{2\rho^2R^2T\epsilon d^2} \tag{3.4.20}$$

Eq. (3.4.20) contains two terms. The pressure drop term depends on $1/d^2$, while the heat transfer term depends on d^2. This implies a minimum entropy generation for some value of d. To obtain a crude estimate of optimal value of d for the purpose of design, the derivative of Eq. (3.4.20) with respect to d was calculated. The physical properties of the magnetic refrigerant and the working fluid were evaluated at 5 K and the other design variables were taken from Table (3.3.1). The results suggested that the optimal channel width is less than 0.002 mm. Fig. (3.4.9) shows the rate of entropy generation at 5 K due to fluid friction and fluid to wall heat transfer plotted versus the channel width.

A channel width of 0.1 mm was selected because of concern that the tolerance of the channels (approx. 0.025mm) would lead to serious flow maldistribution if

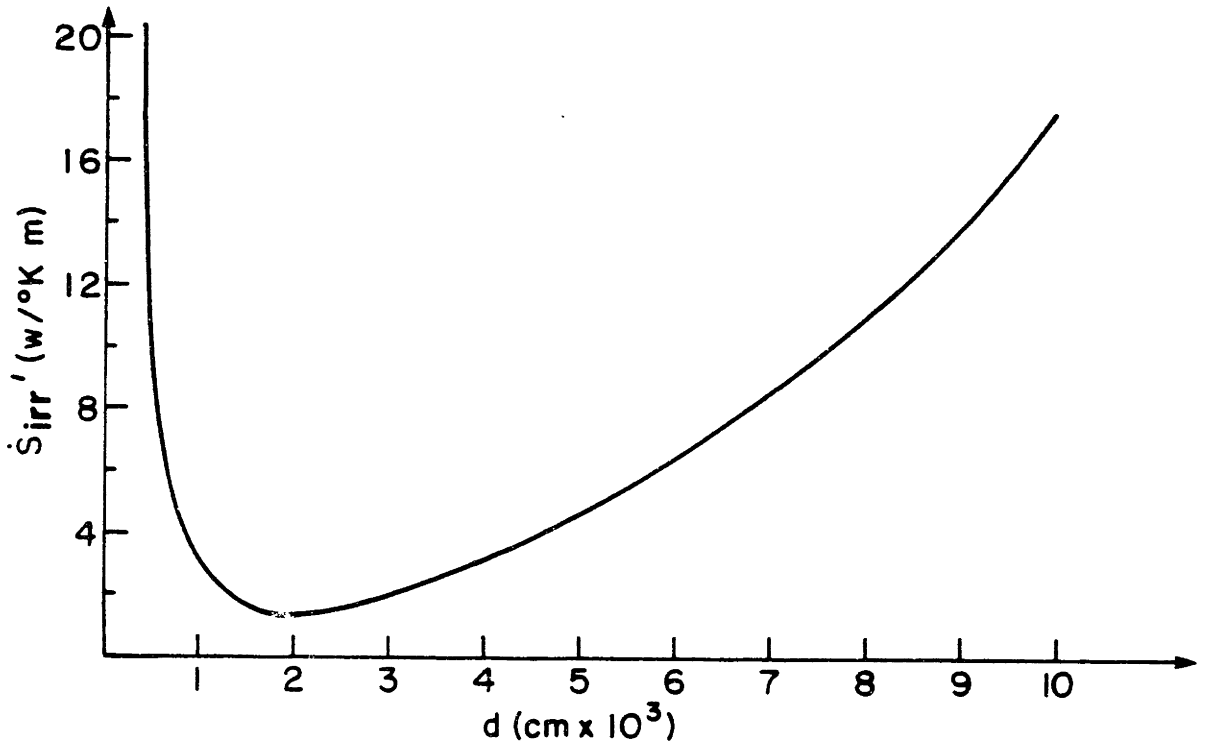

Fig. (3.4.9) Entropy generation vs d at $5\,K$

narrower channels were chosen and because smaller passages would require thinner plates. The slot spacing b required to keep the porosity at 4% for 0.1 mm passages is 02.5 mm. Thinner plates would be very difficult to handle and process.

Selection of t and w

The thermal barrier thickness w and the segment thickness t were selected to minimize axial conduction, to promote the most efficient heat transfer between working fluid and wall, and to avoid the entrainment of excess non-active heat capacity material in the core.

The core will be idealized as a series of isothermal segments separated by adiabatic barriers. This assumption is valid if the internal conduction resistance of the segments is much smaller than the boundary resistances. The final portion of this section will examine this and the other assumptions made in the analysis.

The heat transfer irreversibility assosciated with the thickness of the isothermal segment can be calculated from the simple model shown in Fig. (3.4.10).

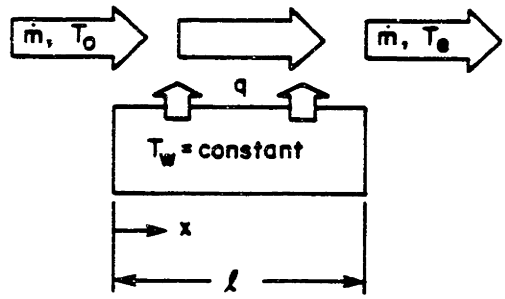

Fig. 3.4.10 Isothermal wall segment

Fig. (3.4.10) shows fluid, with constant specific heat c_p, being heated from entering temperature T_0 to exiting temperature T_e while flowing by an isothermal wall of temperature T_w. The entropy generated by this heat transfer process is

$$\dot{S}_{irr}\,|_{\text{const } T_w} = \dot{m}c_p\left(\ln\frac{T_e}{T_0} - \frac{T_e - T_0}{T_w}\right) \tag{3.4.21}$$

The heat transfer rate equation determines the relationship between the local helium temperature and the wall temperature.

$$T_w - T(x) = \frac{T_e - T_0}{(1 - e^{-N})}e^{-\frac{\hbar P x}{\dot{m}c_p}} \tag{3.4.22}$$

The dimensionless quantity N is defined as $(\hbar\,\alpha\,\ell)\,/\,(\dot{m}c_p)$, α is the heat transfer area per unit length, and $\hbar$ is the heat transfer coefficient. The wall temperature is found by evaluating the rate equation at the entrance to the segment.

$$T_w = \frac{T_e - e^{-N}T_0}{1 - e^{-N}} \tag{3.4.23}$$

The irreversibility can now be expressed in terms of entering and exiting temperatures of the fluid and the properties of the surface and fluid.

$$\dot{S}_{irr}\,|_{\text{const } T_w} = \dot{m}c_p\left(\ln\frac{T_e}{T_0} - \frac{(T_e - T_0)(1 - e^{-N})}{T_e - NT_0}\right) \tag{3.4.24}$$

If, instead of being heated by a single isothermal wall of length ℓ, the fluid were heated by two separate isothermal walls each of length $\ell/2$ shown on Fig. (3.4.11),

then approximately

$$\dot{m}c_p\left(\frac{(1-e^{-N})^2(T_e-T_0)^2}{4(T_e-e^{-N}T_0)^2}\right)$$

less entropy would be generated.

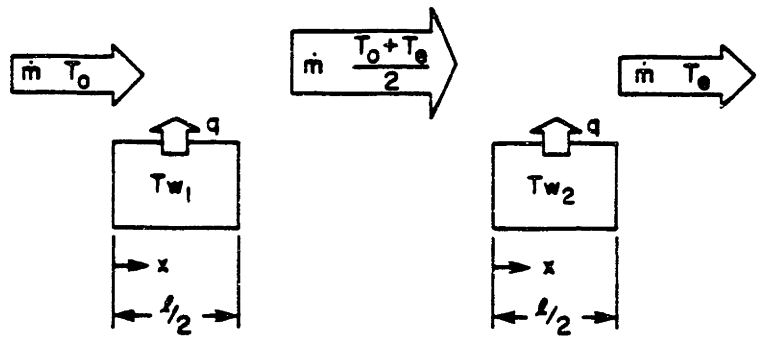

Fig. 3.4.11 Two isothermal segments

The entropy production decreases for thinner and thinner segments until the limit of constant wall-fluid ΔT is reached. The entropy production for the constant ΔT case is given by Eq. (3.4.25) .

$$\dot{S}_{\text{const }\Delta T} = \dot{m}c_p\left(\ln\frac{T_e}{T_0} - \ln\left(\frac{T_e + \frac{T_e-T_0}{N}}{T_0 + \frac{T_e-T_0}{N}}\right)\right) \tag{3.4.25}$$

Fig. (3.4.12) shows qualitatively how the entropy production is reduced by lowering the average stream-to-wall temperature difference from the one-segment case to the two-segment case and finally to the constant-wall-flux case.

The number of segments required to approximate the constant ΔT case for this specific design is shown on Fig. (3.4.13). The figure shows a plot of the ratio entropy generation for a constant wall temperature segment at the cold end of the core to an equivalent length segment with constant ΔT, as a function of the total number of segments in the core. The heat transfer coefficent is calculated based on laminar flow in the 0.1mm wide flow passages. The core diameter, core length, and mass-flow rate come from Table (3.3.1). Fig. (3.4.13) indicates that the constant ΔT approximation is valid above 40 segments (7.6 mm = t).

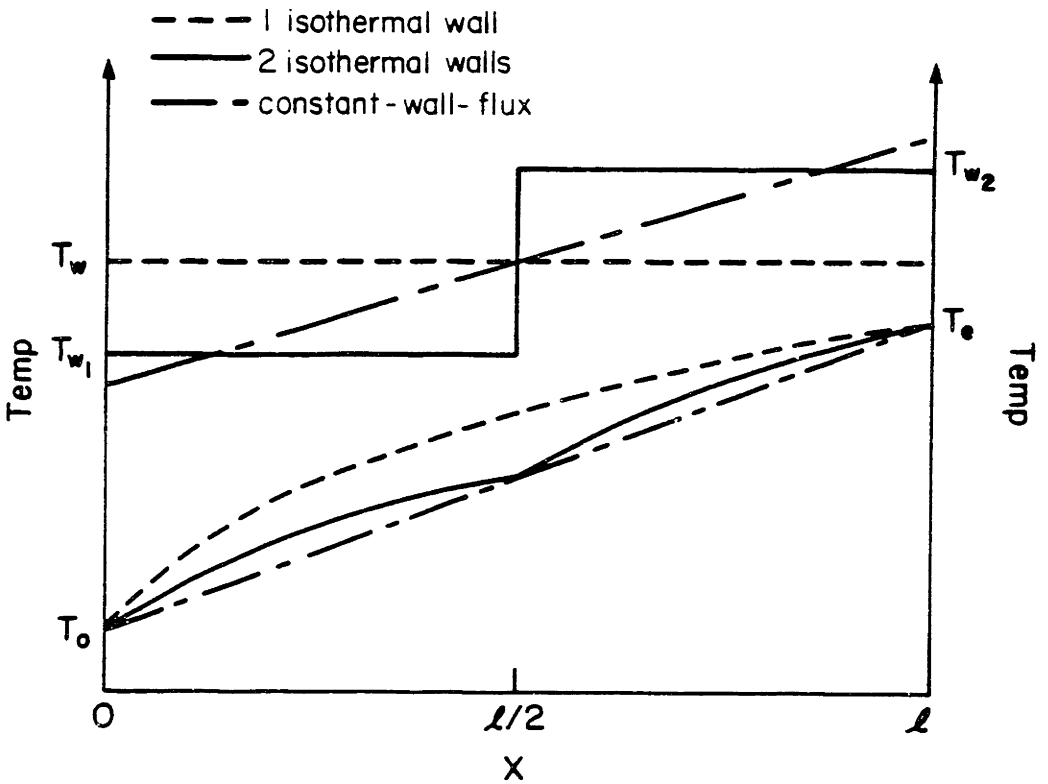

Fig. (3.4.12) Comparison of average stream-to-wall ΔT

Axial conduction through the composite regenerator core can be calculated by Eq. (3.4.8). Fig. (3.4.14) shows the axial conduction heat leak plotted versus the ratio of barrier thickness to segment thickness ϵ_B.

The heat capacity of the thermal barrier material causes a loss of refrigeration analagous to the loss of refrigeration produced by helium in the void space of the regenerator core. An equation analagous to Eq. (3.4.3) can be written to describe the loss of refrigeration due to the heat capacity of the thermal barrier material.

$$\frac{\Delta S_{barrier}}{\Delta S_{isothermal}} = \frac{\rho_B c_B \epsilon_B \ln \frac{T_f}{T_i}}{m_s c_p \frac{dT}{dz}/T} \tag{3.4.26}$$

The subscripted variables ρ_B, c_B, and ϵ_B refer to the density, specific heat, and filling factor of the thermal barrier material. The ratio T_f/T_i is the ratio of final to initial temperatures of an adiabatic process. The variables c_p, $\frac{dT}{dz}$, and T all refer to the local helium condition during a flow process. The maximum loss of refrigeration is calculated by evaluating Eq. (3.4.26) for a Carnot cycle at the hot

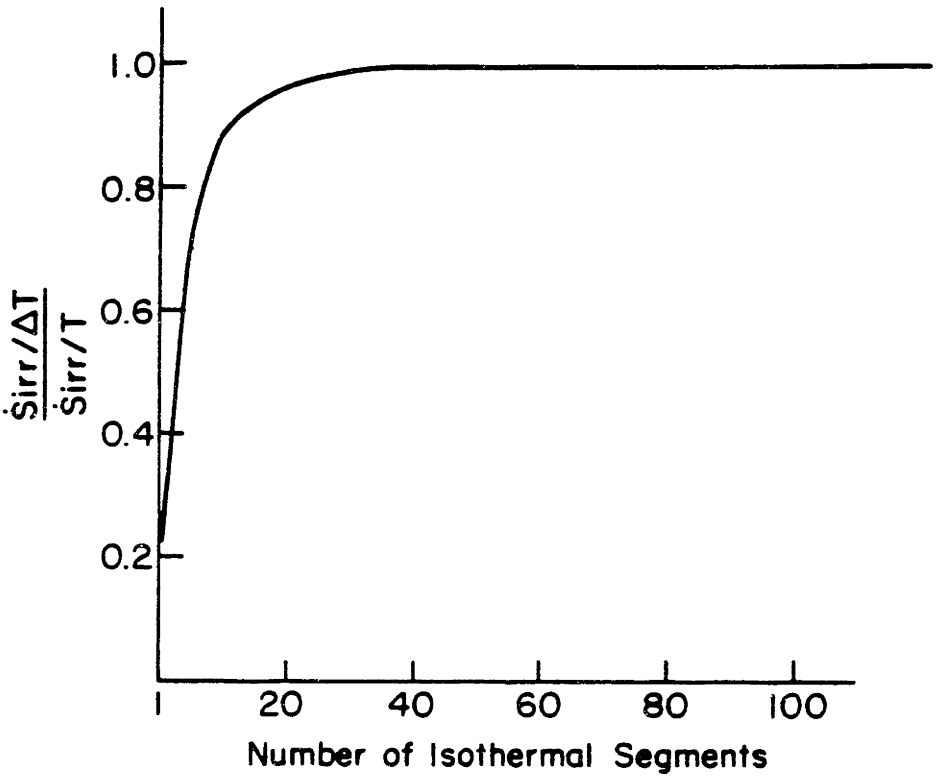

Fig. (3.4.13) Entropy generation versus number of segments

end of the regenerator. Fig. (3.4.15) shows the results of the loss calculation as a function of ϵ_B with Nylon's properties assumed for the thermal barriers.

The final selection of the variables t and w was influenced largely by manufacturing considerations. The minimum thickness for a thermal barrier was assumed to be 0.1mm, the approximate glueline thickness of an epoxy joint. For the purposes of handling and machining the GGG, a wafer thickness, $t - w$, of 2.5 mm is convienient. The resulting axial conduction from Fig. (3.4.14) is less than 0.015W and Fig. (3.4.13) shows the heat transfer condition is well approximated as constant wall flux. Finally, Fig. (3.4.15) indicates that the dimensionless entrainment loss is about 1.5%.

The internal geometry of the parallel plate regenerator core is now completely specified: $d = 0.1$mm, $b = 02.5$mm, $t = 02.5$mm, and $w = 0.1$mm. The selection of these variables made use of several simplifying assumptions which will now be

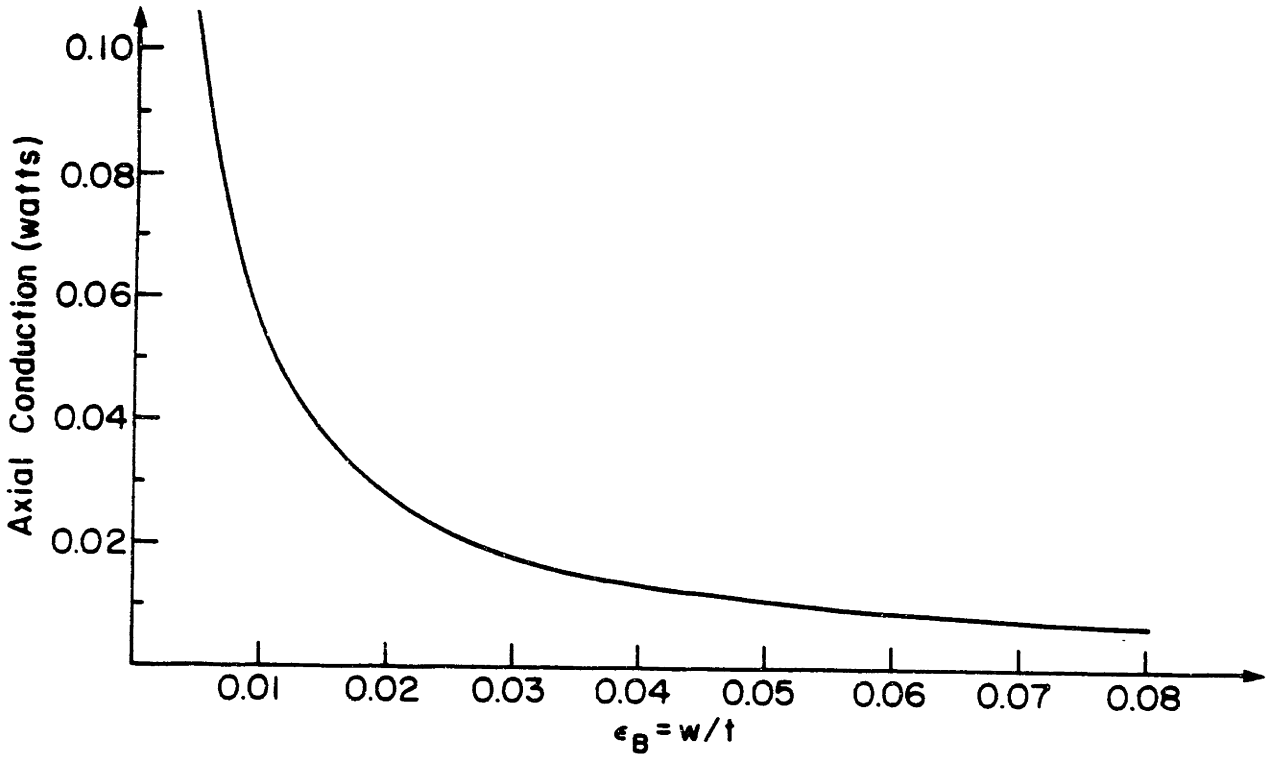

Fig. (3.4.14) Axial conduction heat leak

reviewed.

Many of the design relationships used employed the assumption of constant properties; although this assumption is not accurate, it serves to provide order of magnitude relationships between the variables. The actual properties were included in the numerical simulations done by Gallagher[22].

The heat transfer and fluid friction correlations were made on the assumption of laminar fully developed flow. The Reynolds number for the parallel plate geometry is

$$N_R = \frac{m_s \pi}{8\mu\epsilon R^2 \tau_T}. \tag{3.4.27}$$

and evaluates to 870 for the design selected. From a standpoint of heat transfer, the asssumption of fully developed flow is conservative and for the specific design fluid friction turned out to be very small.

The assumption was made that the axial segments of refrigerant were isothermal separated by adiabatic barriers, which is true if the internal conduction re-

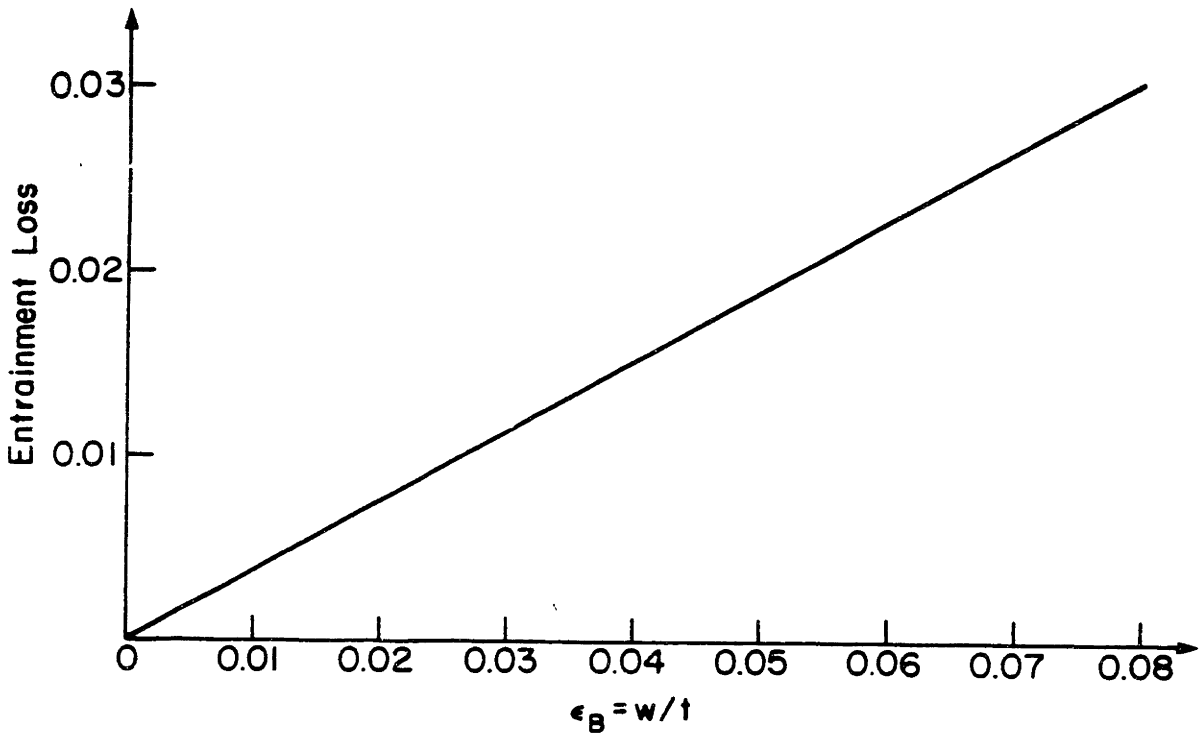

Fig. (3.4.15) Dimensionless barrier entrainment loss

sistance of the wafers $R_{GGG_{internal}}$ is much smaller than the convection boundary resistance R_{conv} and the thermal barrier conduction resistance $R_{barrier}$.

$$R_{GGG_{internal}} = \frac{2t}{k_{GGG}b} = 3.4 \text{ cm K W}^{-1} \tag{3.4.28}$$

$$R_{conv} = \frac{d}{4.1k_{He}t} = 12.1 \text{ cm K W}^{-1} \tag{3.4.29}$$

$$R_{barrier} = \frac{2w}{k_{barrier}b} = 68 \text{ cm K W}^{-1} \tag{3.4.30}$$

Heat transfer irreversibility internal to the salt was neglected compared to the convection boundary. This is true if the transverse conduction resistance in the refrigerant $R_{GGG_{trans}}$ is much smaller than R_{conv}.

$$R_{GGG_{trans}} = \frac{b}{2k_{GGG}t} = 0.86 \text{ cm K W}^{-1} \tag{3.4.31}$$

The flow processes were assumed steady for the purposes of design. This assumption is not true because the rate of magnetic refrigeration is not steady with a constant field variation and because the temperature profiles after a nonflow process do not coincide with those for a flow process. The irreversibility assosciated with the transient behavior of the core may be severe if the thermal response time of the core is long. A well-designed core should have a short thermal response time relative to the duration of the flow process. The lumped parameter time constant for the core provides an estimate for the thermal response of the core.

$$\tau_{nat} = \frac{\rho_{GGG} c_{GGG} (\epsilon - \epsilon^2) b^2}{7.5 k_{He}} \tag{3.4.32}$$

The specific heat for the GGG is estimated as the zero-field specific heat at 5 K. The value of τ_{nat} is 0.04 s which is approximately 100 times smaller than the time of a flow process.

Chapter 4 The Experiments

This chapter describes the preliminary experiments which have successfully demonstrated the concept of magnetically active regeneration. Section 4.1 describes the experimental apparatus in terms of its functional subsystems. The procedures for conducting the experiments are briefly discussed in section 4.2. The required quantities of cryogens, make-up gas requirements, and cool-down times are also included in section 4.2. Section 4.3 discusses the results from the preliminary experiments. Data was collected for three modes of operation: helium circulation between the reservoirs without magnetic field change, field changes without helium circulation, and helium circulation between the reservoirs while the magnetic refrigerant was subjected to field changes. The data reduction techniques , sources of experimental error, and the sensitivity of the system to variations in operating conditions are discussed. Section 4.3 concludes with suggestions for further study.

4.1 Experimental Apparatus

Fig. (4.1.1) shows a schematic of the experimental apparatus. The schematic can be organized in five subgroups based on function: gas handling, temperature control, magnetic field, helium dewar, and regenerator core. The design of the regenerator core was discussed in Chapter 3 and its construction detailed in Appendix 3.

Gas Handling System

The components of the gas handling system shuttle the 3-atm supercritical helium back and forth through the regenerator core. The two components of the gas handling system are the displacer (Fig. (4.1.2)) and the compensator (Fig. (4.1.3)).

The displacers position is controlled by a stepper-motor-driven ball-screw. A Compaq Plus^{TM} computer sends position commands to a translator which converts the commands to 6 A current pulses in the switching sequence required to drive the

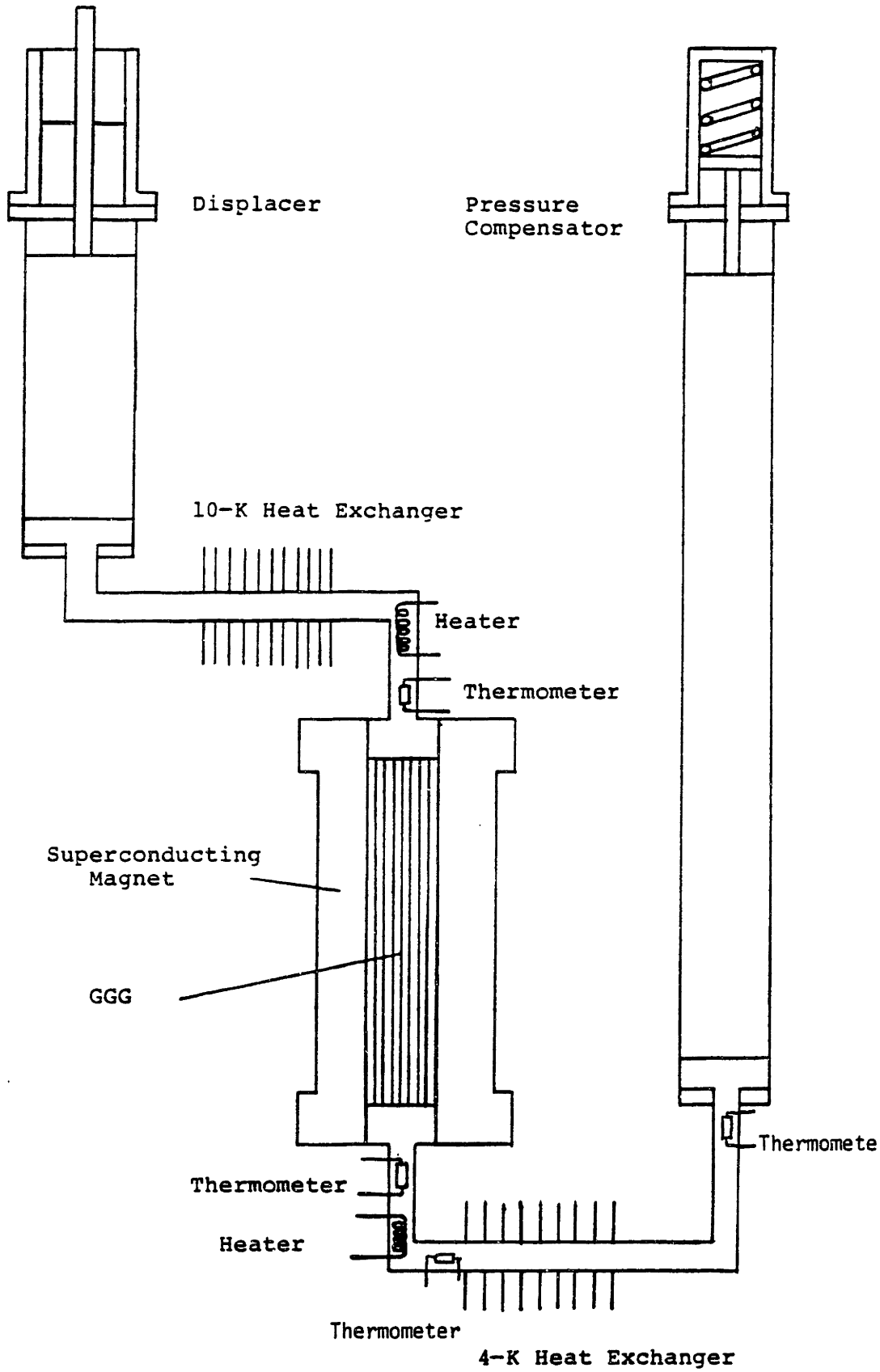

Fig. 4.1.1 Configuration of the Magnetic Refrigerator

windings of the stepper-motor. Position commands can also be relayed manually to the stepper-motor from the control panel.

The swept volume of the displacer is 620 cm^3 which is required to contain the shuttle mass (4.6 g) at 15 K and 3 atm. The displacer stroke of 7.6 cm was chosen to limit the shuttle losses[24-5] which are proportional to the square of the stroke. The displacer cylinder length of 68 cm was selected as a compromise between providing a large liquid helium reservoir for the experiment and reducing axial conduction heat leak. The large displacer bore of 10.2 cm (required to provide the swept volume) caused two difficulties. The large cross-sectional area of the displacer (81 cm^2) required to provide the swept volume led to high actuation force and large axial conduction through the displacer piston. To reduce the 570 lb force needed to move the displacer against the working gas both the rod and the piston were sealed and helium regulated at slightly below the working pressure of the refrigerator was introduced on top of the piston. The backing-gas reduces the actuation force sufficiently that a stepper motor with 400 in-oz of running torque can drive the displacer at acceptable rates. The backing gas has the additional advantage of minimizing the load on the seals at the top of the piston. The axial conduction through the displacer piston was reduced by constructing it as a hollow evacuated linen phenolic unit with aluminized mylar radiation shields inside. The piston was glued together with a low temperature epoxy. The external surface of the displacer piston was sealed with the same epoxy then wet sanded to run smoothly in the 0.9 mm wall stainless steel cylinder.

The compensator is a passive element designed to maintain the refrigerator system pressure at 3 atm while the displacer moves the shuttle mass between the hot and cold reservoirs. The task of pressure regulation is simplified because the pressure drop through the core is 4% of the system pressure. The compensator (Fig. (4.1.3)) is a free floating piston exposed to the working gas on one side and pressure regulated backing-gas on the warm side, an auxillary spring (not used in the preliminary experiments) is available as a mechanical aide. Friction is minimized by the use of a Bellofram rolling diaphragm for the main seal, the piston rod is

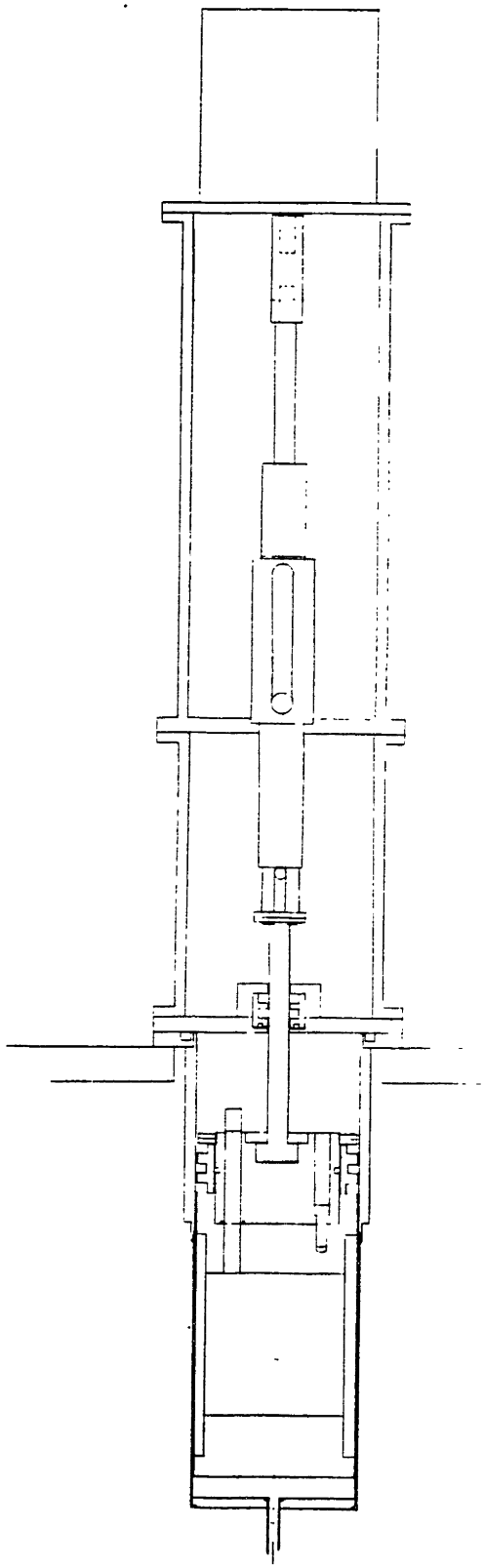

Fig. 4.1.2 Displacer Assembly

sealed with a small diameter O-ring with minimal drag. The compensator piston is 3.8 cm in diameter and 1.02 m long. It is made from molded linen phenolic and like the displacer runs in a 0.9 mm thick type 304 stainless steel cylinder. The smaller bore of the compensator reflects the factor of 10 decrease in the volume required by the shuttle mass at the cold end of the regenerator. The compensator length was selected so that its working volume would always be immersed in 4.2 K liquid helium.

The working volume is charged through a separate valve and regulator. When running experiments the charging valve is closed and a fixed mass of helium is maintained in the working volume of the experiment. A mechanical bourdon tube type pressure gauge connected to the warm end of the charging line monitors the working gas pressure at all times. A 60 psig pressure relief valve is connected to the charging line to prevent accidental over-pressurization of the system.

Magnet System

The magnet system for the magnetic refrigerator consists of a superconducting solenoid, vapor-cooled current leads, a computer-controlled current supply, and a magnet protection system. The components of the magnet system are shown schematically on Fig. (4.1.4).

Superconducting Magnet

The superconducting solenoid designed for this experiment has a bore of 4.4 cm and a total length of 34.5 cm. Within the 30.5 cm active length of the magnet the field is uniform within 6% from end to center. The magnet is designed to be operated in an AC mode and therefore is wound in an open fashion with spacers providing cooling between adjacent layers of wire. The AC losses produced operating the magnet with a triangular current waveform between the amplitudes of 15 A and 105 A at 0.08 Hz are approximately 1.5 W.

The losses are almost entirely due to hysteresis within the 9μm diameter niobium-titanium superconducting filaments. The hysteresis loss is directly proportional to the filament diameter. Niobium-titanium superconductor with a 0.5 μm

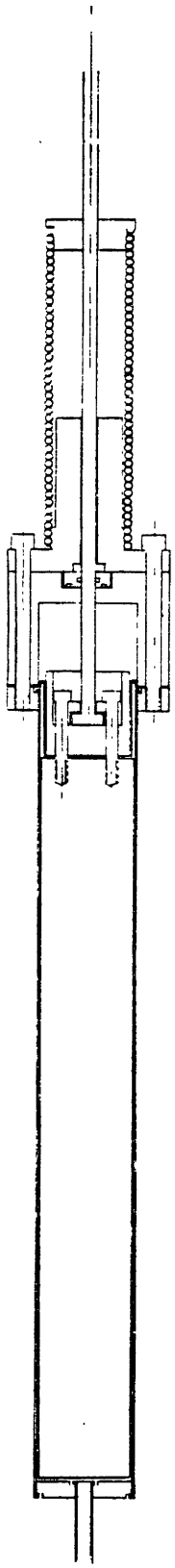

Fig. 4.1.3 Compensator Assembly

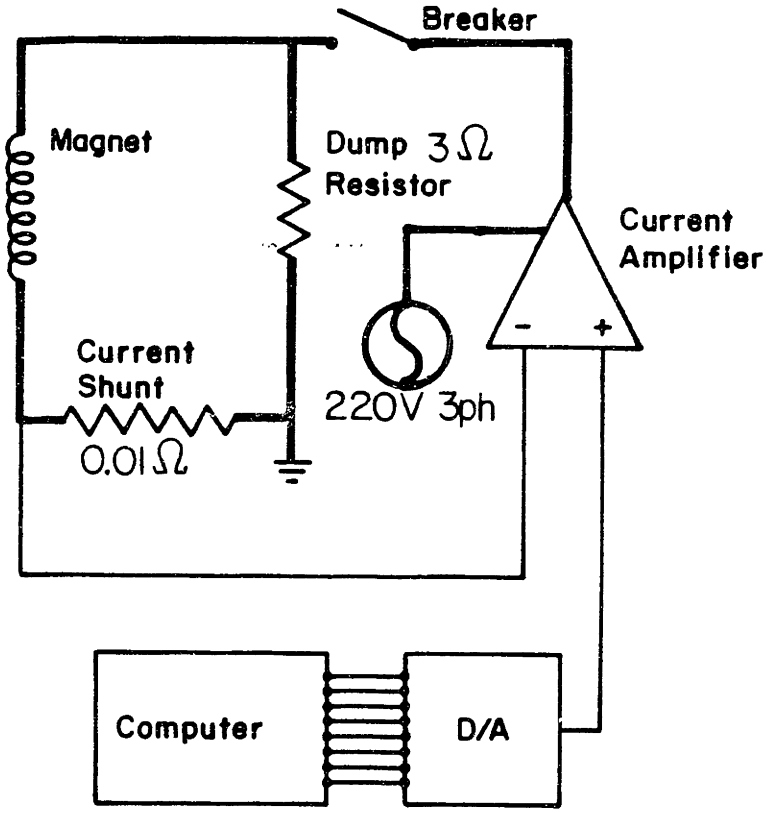

Fig. 4.1.4 Magnet System Schematic

diameter filaments is commercially available[26]. The use of 0.5 μm filament wires would reduce the loss due to hysteresis nearly 20 fold. Details of the design of the superconducting solenoid including loss calculations, field predictions, heat transfer estimates, and specific dimensions are given in Appendix 2. The experimental measurement of the AC loss, the field profile, and the inductance of the magnet are reported by Chin in Ref. 27.

Operation of the Magnet

The current is delivered to the magnet via two vapor-cooled current leads connected at the top of the dewar to 0000-gage copper leads completing the circuit to the current supply. The current supply is a 12-KVA 3-phase induction-motor driving a compound wound DC generator. The motor generator was originally constructed as a welder in the 1930's. The DC machine was modified by disconnecting the series winding and attaching the shunt winding to linear amplifier. An Aerotech model 4020B linear amplifier provides separate excitation to the field of the DC generator. It controls the current through the magnet via current feedback from

the 0.01Ω current shunt in series with the magnet. Fig. (4.1.4) shows a schematic of the magnet control system. The combination of the servo-amplifier and the motor generator is represented by the block labeled current amplifier. The heavy traces on the figure represent the power leads (including both the room temperature and the vapor-cooled leads). The lighter traces represent signal level paths.

Current commands are sent from the Compaq-Plus^{TM} computer. Current commands are output from the computer as 8 bit binary words then converted to analog signals and input to a transistor line driver connected to the remote amplifier. The digital to analog converter circuit contains logic which requires the computer to send a zero current command before opening communication to the magnet controller. The purpose of this precaution is to prevent accidentally quenching the magnet with a step current command.

Magnet Protection

The magnet protection system consists of a 200 amp AC circuit breaker, and a 3 Ω dump resistor. Most small magnets are self protected by the voltage/current characteristics of their power supplies: that is, as the normal zone propagates and the magnet resistance increases the droop of the power supply's V-I characteristic keeps the current at a safe level. The motor-generator can source up to 90 V at the magnet's maximum current of 125 A which could destroy the magnet in the event of a quench. A panel mounted control opens the circuit breaker forcing the magnet to ramp down on the dump resistor (the panel control and the circuit breaker are represented by the block labeled breaker on Fig. (4.1.4)). Gallagher[28] has constructed an automatic quench detection circuit which senses resistive voltages in the magnet. The ciruit uses a center tap in the magnet and a bridge network to cancel out inductive voltages. The dump resistor is always in the circuit but draws less than 8 A during normal operation.

Core Container

The regenerator core is separated from the superconducting solenoid by a thermally isolating pressure tight, magnetically transparent container (Fig. (4.1.5)). The container which houses the regenerator core is a vacuum jacket composed of

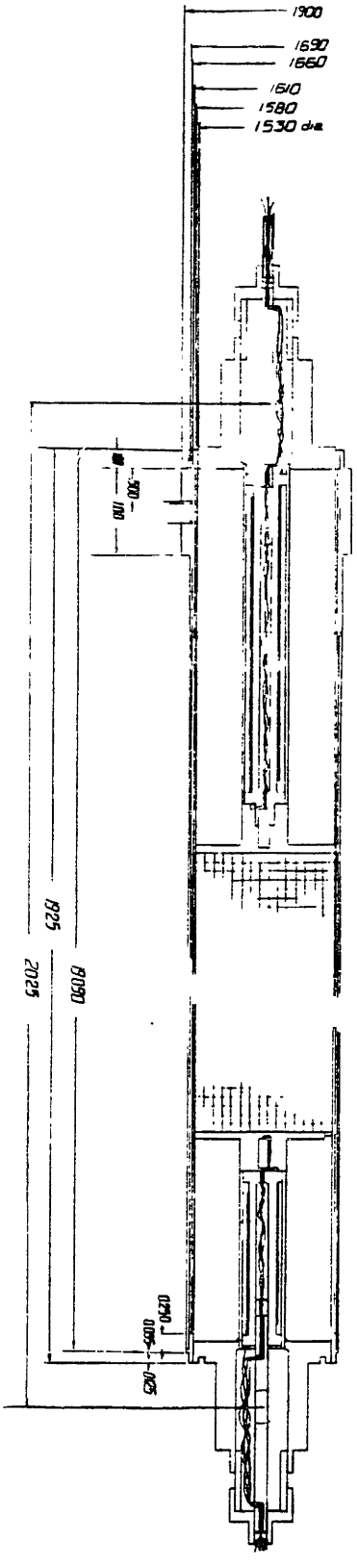

Fig. 4.1.5 Core Container Section

two concentric 0.38 mm thick type 304 stainless steel cylinders. The total radial thickness of the vacuum jacket is less than 1.5 mm. The vacuum space in the jacket is connected to a room temperature pressure-relieving pump-out valve. A fine strand of helically wound monofilament in the vacuum space prevents buckling. The magnet, wound on a 1.5 mm thick linen phenolic coil former, slides onto the outside of the vacuum jacket. Eddy current heating in the walls of the container is negligible at the 0.08-Hz operating frequency.

Temperature Control

At either end of the regenerator core the supercritical helium entering the core is conditioned by temperature controllers. The purpose of the temperature controllers is to simulate constant temperature reservoirs of adjustable temperature. The controllers at both ends of the core are very similar. The temperature controller at the warm end will be described in detail then the features unique to the cold-end controller will be presented.

Warm-End Temperature Controller

The warm-end temperature controller components are: a temperature sensing element, a heat exchanger, a control heater, and a control circuit. Fig. (4.1.6) shows a schematic of the warm end temperature controller.

During a hot blow working fluid exits the top of the regenerator core at a temperature higher than the hot-reservoir temperature. The effluent is then cooled as it passes through the heat exchanger and into the displacer. Once the displacer reverses direction, commencing a cold blow, fluid again passes through the heat exchanger now lowering its temperature below the desired hot reservoir temperature. The temperature is measured at the entrance to the core and the control circuit commands the control heater to add sufficient heat to correct the fluid temperature to the set point. The temperature sensor is a Lake Shore Cryotronics carbon-glass resistance thermometer model CGR1-20000. A CGR was chosen for its greater sensitivity (compared to the more economical carbon resistors) at temperatures around 10 K. The resistance of the sensor is measured using a 4-wire technique.

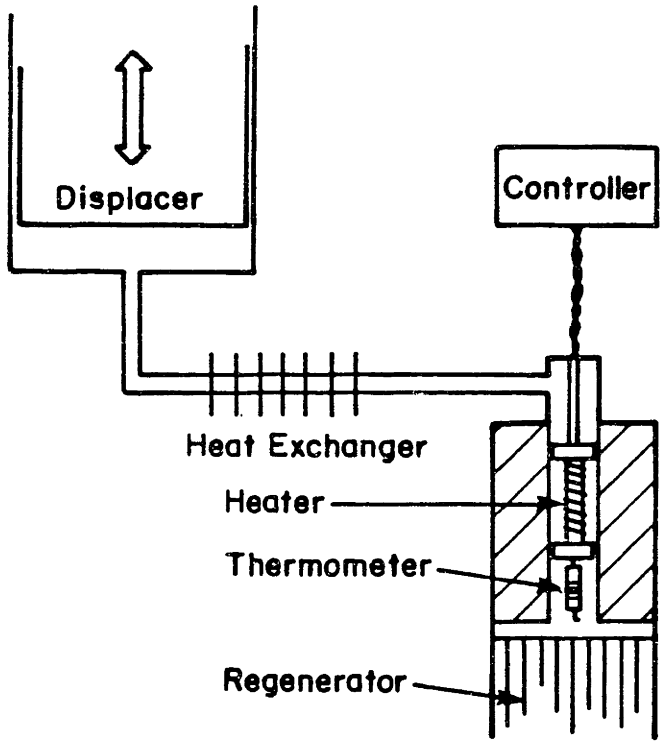

Fig. 4.1.6 Temperature Controller Schematic

A Lake Shore precision current source runs 20 μA through the element while the voltage is measured through separate voltage taps.

The heater (Fig. (4.1.5)) is a 3 Ω. resistor constructed from a length of 0.51 mm diameter type 304 stainless steel wire wound on a spool of epoxy fiberglass composite. The spool is inserted into the 1.1 cm ID flow passage so that all the helium is forced to flow in the 0.76 mm annulus between the heater and the wall. The stainless steel wire is sheathed in a loose woven sock of Nomex^{TM} fibers which provides electrical insulation while minimizing impairment of heat transfer from the wire. The Nomex^{TM} insulation has the additional advantage that if the heater is accidentally turned on at room temperature, the insulation will not be harmed. Stainless steel (type 304) was chosen for the resistor because its resistivity is independent of temperature and because of its relatively low resistivity for an alloy. Because the resistivity is low compared to other alloys a resistor made from the same diameter wire with the same total resistance will have lower heat generation per unit length (and accordingly greater length) at a given excitation. Therefore, if the heat

transfer is fixed, then the lower resistivity material will have a lower stream-to-wall temperature difference.

The heat exchanger for the hot-end temperature controller consists of two parts, one exchanging heat with boiling 4.2 K helium the other utilizing sensible heat from the boil-off vapor of the experiment. The boiling heat exchanger is a single 0.88 mm wall, 1.27 cm OD 304 stainless steel tube immersed in the liquid helium bath. The vapor heat exchanger is a Lytron model 5110. It is an aluminum cross-counterflow core with extended surface on both sides. The heat exchanger was modified by adding an aluminum-to-stainless steel friction-welded transition joints (manufactured by Oxford Instruments) to connect it to the stainless steel plumbing on either side of the heat exchanger.

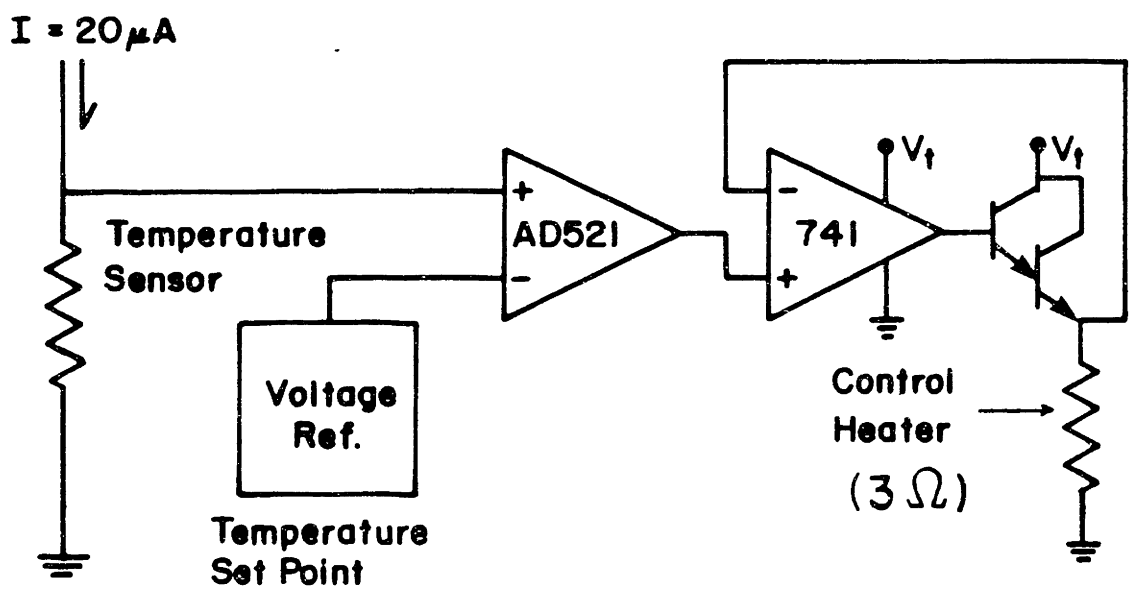

Fig. 4.1.8 Temperature Control Circuit

The control circuit is a simple analog proportional controller whose basic structure is shown on Fig. (4.1.7). The output of the carbon glass resistor is compared to an adjustable voltage reference using an Analog Devices Model 521 instrument am-

plifier. The output of the instrument amplifier is input to a single ended unity gain power amplifier consisting of an op-amp driving a Darlington pair. The power amplifier is single ended so that negative inputs corresponding to sensor temperatures greater than the set point do not cause the heater to energize. The gain of the instrument amplifier is variable thereby allowing gain adjustment of the proportional control. The control circuit contains an additional safety feature which automatically shuts off the heater if it has been on continuously for several refrigeration cycles.

Cold-End Temperature Controller

The cold-end temperature controller differs from the warm end in its component specifications and an additional feature of the control circuit. The cold end temperature control circuit contains an additional interlock which prevents the cold blow effluent from being heated by the control heater. Instead the cold blow mass flux refrigerates the liquid helium bath through a heat exchanger. The cold-end heat exchanger is constructed from 3 parallel 3.2 mm diameter by 0.89 mm wall copper tubes approximately 30 cm long. The temperature sensor at the cold end of the regenerator core is a carbon resistor connected for a 2-wire measurement. A spare resistor is mounted next to the sensor for redundancy. The control heater at the cold end is identical in construction to the hot end but has a slightly lower resistance. The detailed design and experimental performance of the warm-end temperature controller are given in a thesis by Heffernan[29].

Dewar

The experiment runs immersed in a pool of 4.2 K liquid helium whose height is maintained above the top of the superconducting magnet and below the vapor cooled heat exchanger. The helium dewar, shown on Fig. (4.1.8), which contains the experiment has an ID of 204 mm and an inside length of 1.6m. The dewar is constructed with two independent vacuum spaces separated by a liquid nitrogen reservoir. The inner cylinder is demountable and can stand alone.

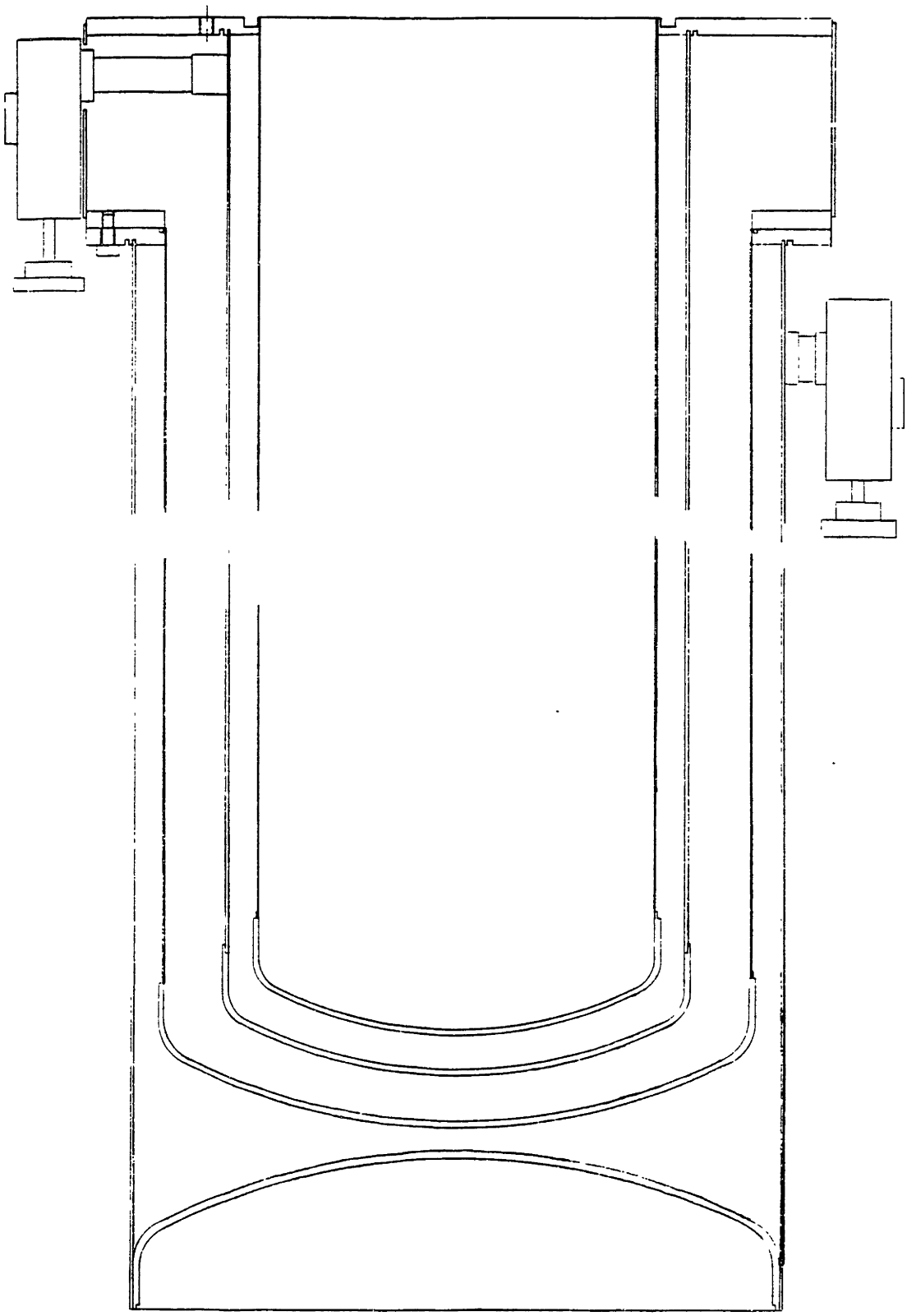

Fig. 4.1.8 Magnetic Refrigerator Dewar

4.2 Procedure for the Preliminary Experiments

The procedures of the preliminary experiments are discussed in this section. For these early trials the temperature controllers were not used and the pressure compensator was manually assisted.

Purging the System

The evening before conducting an experiment the vacuum spaces of the experiment are roughed to a pressure of approximately 10×10^{-3} torr. These vacuum spaces include the two vacuum jackets on the helium dewar, the helium transfer tube, and the spare helium transfer tube. The vacuum space in the displacer piston and the vacuum insulation surrounding the regenerator core cryo-pump during cool-down.

The morning of an experiment the first task is to purge the refrigerator working space and charge it with helium. Purging is accomplished by charging the system to rated pressure with helium then bleeding down to several psig. The purging process is repeated about six times. The working space is then left connected to regulated 4 psig helium throughout the cooldown precedure.

77 K Precooling

The helium dewar nitrogen jacket is filled with liquid nitrogen concurrent with the purging of the working volume. Once the working volume is purged the helium space is precooled with liquid nitrogen. Nitrogen is introduced to the helium space through the transfer tube sheath. The transfer tube sheath is a 13 mm diameter 0.38 mm wall tube which extends from the top flange of the experiment to within 2.5 cm of the bottom of the dewar. Precooling proceeds until the liquid nitrogen level reaches the bottom of the vapor cooled magnet leads (as witnessed by liquid ejecting from their tops). Resistance of the magnet serves as another indicator of the progress of the cooldown. The resistance of the magnet drops by a factor of 8 from room temperature to liquid nitrogen temperature.

Liquid Helium Transfer

The precoolant is voided from the experiment by plugging the vapor vents on the leads and pressurizing the dewar with nitrogen gas through the main vapor

vent in the top flange, forcing liquid nitrogen to exit via the transfer tube sheath. The residual liquid nitrogen in the bottom of the dewar is voided by inserting a thin probe through the sheath which reaches the bottom of the dewar and injecting warm helium gas. It is extremely important to remove all liquid nitrogen before transferring helium into the experiment. If any appreciable quantity of nitrogen remains its high heat of fusion will prevent cool-down to liquid helium temperature. Precooling the experiment and maintaining the level in the liquid nitrogen jacket for a days worth of experiments requires about two 160$\mathcal{L}$ containers of liquid nitrogen.

Transfer of helium commences directly after voiding the experiment of precoolant. A 100 liter storage dewar of liquid helium serves for a day's experiments. Approximately 40 liters of helium are required to cool the experiment to 4.2 K and fill the dewar to the bottom of the vapor heat exchanger. A 76 cm helium liquid level gauge is mounted in the experiment so that it indicates 100% just below the vapor heat exchanger. The experiment can be run until the level gauge drops to 60% which is approximately 1 cm above the top of the magnet. About 10 liters of helium are in the space between 60% and 100% on the level gauge. Topping off the dewar with helium through the transfer tube sheath can be accomplished with a minimum loss of helium.

Charging the System

Once the dewar is filled with helium, the working volume is charged to 3 atm with the displacer at the bottom of its stroke. The charging valve is then closed. The backing-gas pressure is concurrently brought up to a pressure of 28 psig. It is necessary to maintain the backing-gas pressure at a level below the working pressure to avoid reversing the convolution of the rolling diapragm seal. The backing-gas is supplied by a standard 180ft^3 gas bottle (1800 psi charge) and will usually last for a day of experiments. The backing gas cylinder can be replaced without contamination of the experiment if required.

Control of the Experiment

The motion of the displacer and the magnet current are controlled by the Compaq Plus^{TM} computer. A program was written which allows keyboard input

of the current and displacer waveforms. Before starting the cycle the computer initializes the magnet at the minimum field selected for the run and positions the displacer at the bottom of its stroke, thus placing the shuttle mass in the cold end of the refrigerator. The computer continues to operate the cycle under the selected conditions until it recieves a keyboard interrupt which causes the computer to exit the cycle by returning the displacer to the bottom of its stroke and ramp the magnet down to zero current.

Experimental measurements

The experimental data was collected by an Acro Systems Model 900 data acquisition system. The Acro recieves an instruction from the Compaq computer to begin data collection once an experimental run starts. The Acro internally stores the data until the run is over then relays the data to the host computer over the RS232 asynchronous communications port at 9600 baud. Six experimental measurements were made during the preliminary experiments. Each measurement was made five times per second. The six analog signals are converted to 12-bit digital words using dual slope integration which, though slower than successive approximation, provides superior noise rejection. The voltages of the following six sensors were measured: the carbon glass resistor, the carbon resistor at the base of the regenerator core, the carbon resistor at the regenerator side of the cold end heat exchanger, the carbon resistor at the compensator side of the cold end heat exchanger, the current shunt in the magnet lead, and the LVDT (linear variable differential transducer) mounted on the compensator piston rod. The resistance thermometers were all excited with 20 μA. The locations of the various resistance thermometers are shown of Fig. (4.1.1). The carbon glass sensor was measured using the four wire technique. All the carbon resistors were measured with two wires. The voltage of the Allen Bradleys were on the order of milivolts; the carbon glass on the order of tens of milivolts. The current shunt output ranged to approximately 1V and the LVDT signal level was several volts.

Working pressure was the other experimental variable monitored. The reading

of the bourdon tube pressure gauge was recorded at the beginning of each run. The working pressure as measured from the hot end fluctuated approximately 1/3 atm throughout the run.

Results of the Preliminary Experiments

This section begins with a brief description of the data reduction techniques then examines the results from the three types of experiments performed. The section concludes with some brief comments on how to improve the performance of the cycle and suggestions for further work.

Data Reduction and Error Estimates

For the preliminary experiments the only data reduction performed was that necessary to determine the refrigeration power to the cold reservoir and the heat rejection to the hot reservoir. To calculate these quantities the enthalpy fluxes to the reservoirs must be ascertained. The specific enthalpy at either end of the regenerator core was calculated based on the temperature measured by the local sensor and an assumed 3/,atm pressure. The mass flux was calculated based on the change in compensator working volume. The state of the working fluid within the compensator was assumed to be 3 atm 4.2 K The temperature measured by the carbon resistor located at the exit of the compensator showed this temperature to be between 3.8 K and 4.2 K for the runs reported in this chapter. It will be shown the mass flux is not very sensitive to uncertainty in this temperature. The pressure as indicated by the mechanical (room temperature) gauge was 3 ± 0.3 atm. The rate of volume change was inferred from the LVDT output and its accuracy far exceeds the other experimental measurements. The uncertainty in the massflow can be estimated using the method of Kline and McClintock[30] assuming the uncertainty resides in the density. Eq. (4.3.1) expresses the uncertainty in density ω_ρ in terms of the uncertainty in temperature ω_T, and the uncertainty in pressure ω_P.

$$\omega_\rho = \sqrt{\left(\left(\frac{\partial \rho}{\partial P}\right)_T \omega_P\right)^2 + \left(\left(\frac{\partial \rho}{\partial T}\right)_P \omega_T\right)^2} \qquad (4.3.1)$$

The partial derivatives $(\partial\rho/\partial P)_T$ and $(\partial\rho/\partial T)_P$ are calculated by central difference approximations from the helium tables[31] as $3.14\times10^{-3}\,\mathrm{g\,cm^{-3}\,atm^{-1}}$ and $1.38\times10^{-2}\,\mathrm{g\,cm^{-3}\,K^{-1}}$ respectively. The uncertainty in density calculated from Eq. (4.3.1) is $2.8\times10^{-3}\,\mathrm{g\,cm^{-3}}$ representing an uncertainty of $\pm2\%$ on the nominal value of $.138\,\mathrm{g\,cm^{-3}}$. Neglecting the uncertainty in the volume measurement the uncertainty in mass flux leaving the compensator is also $\pm2\%$

The mass flow at points remote from the compensator depends on the rate of change in mass storage between the compensator and the point of interest. If the hot and cold blows were steady processes then the mass flow would be constant throughout the system. The difference in local mass flow, relative to the mass flow leaving the compensator, results from the volume of the plumbing between the point and the compensator and the change in density with time of the helium within. As an example, consider the error in mass flow of helium entering the cold end of the regenerator relative to the mass flow leaving the compensator. The volume of the plumbing between the compensator and the base of the regenerator core is approximately 27 $\mathrm{cm^3}$ if this volume were to change temperature uniformly between 4.0 K and 2.5 K, at constant 3 atm pressure, during a cold blow a mass storage of 0.32 g would result. The resulting error in mass flow at the base of the regenerator relative to the compensator mass flow would be 7%.

The error in mass flow at the hot end of the regenerator core is larger because of the additional mass contained in the core and because of the larger density variation with increasing temperature. Again, as a pessimistic estimate, if the density-averaged temperature of the entrained helium in the core dropped 1 K from an initial value of 6 K (a density swing of almost 3-fold) the total mass flow error including the error in the cold end plumbing would be almost 30%.

The enthalpy fluxes per cycle to the hot and cold reservoirs were calculated by numerical integration of the data. During a time step of 0.3 s the mass transported between the reservoirs was calculated by the difference in compensator volume and

an assumed working fluid state of 3 atm and 4.2 K. The enthalpy leaving or entering a reservoir was calculated by trapazoidal rule averaging of the enthalpies at the begining and end of a time step for each of the reservoirs, assuming a pressure of 3 atm. The net enthalpy fluxes per cycle were divided by the cycle time in order to express the enthalpy fluxes as average power per cycle.

Results

The magnetic refrigerator was operated in three modes during the preliminary experiments: cycling of the magnetic field without circulation of helium through the core, circulation of working fluid through the core without magnetic excitation, and circulation of working fluid through the core combined with excitation of the magnet. Results from each mode of operation will be discussed. For each run, the experiment was operated for approximately 30 cycles at a speed of 0.1 hz. Cyclic steady state was achieved after 3 or 4 cycles for most operating conditions.

Field Sweep Without Flow

Fig. (4.3.1) shows typical data from a nonflow magnetic field cycling run. The data shown are the seventh, eighth, and ninth cycles of the run. The purpose of cycling the magnetic field without flow circulation was to investigate the effect of magnetic field on the carbon-resistor temperature sensors and to observe for buoyancy driven circulation of the working fluid. The resistance of carbon sensors increases with field and is relatively independent of power rating or nominal room temperature resistance[32-3]. The field effect is inversely proportional to temperature and is significant only for temperatures below approximately 15 K. Reference (32) reports a 2% increase in the resistance of a carbon resistor when the field is increased from 1 T to 4 T at 4.2 K. A resistence increase of 2% at 4.2 K would cause the sensor to indicate a temperature of about 4.15 K. The data of Fig. (4.3.1) indicate that the temperatures fluctuations observed are not the direct result of applied magnetic field because the lowest temperatures occur at low applied field and the sensor at the higher temperature has the larger variation in indicated temperature.

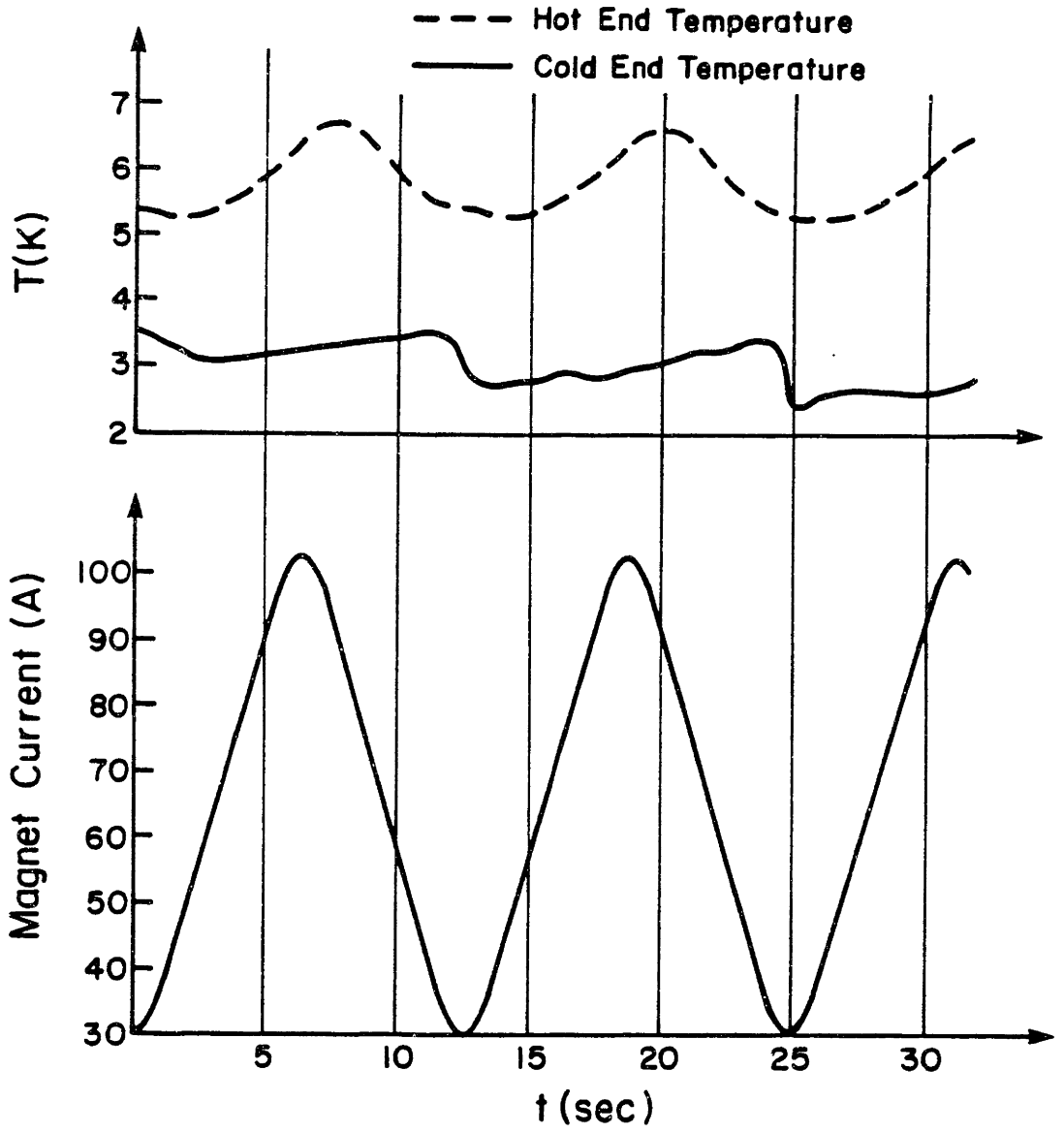

Fig. 4.3.1 Data from a No-Flow Field Cycling Run

During magnetization the temperature increases at the hot end of the regenerator core while the cold-end temperature variation is slight. The cold end temperature drops rapidly at the end of a demagnetization. These temperature variations are most probably explained by two coupled phenomena. The mass of helium entrained in the regenerator core is a strong function of the core's temperature. When the cores temperature drops mass is sucked inside and as the temperature rises mass is expelled. The resulting variation in entrained mass results in a "breathing" phenomenom. Coupled with the breathing effect is a bouyancy driven circulation. Helium is cooled during a demagnetiztion causing it to sink downwards into warmer. lower density fluid below. The converse occurs when helium is heated during a magnetization. The cold end temperature shown of Fig. 4.3.1 gradually decreases through the three cycles shown. The temperature continued to decrease until reaching nearly 2.1 K. The continued lowering of the cold end temperature indicates that the "breathing" and "chimney" effects coupled to produce net refrigeration. It is not possible to quantify the magnitude of the heat pumped because the associated mass flow cannot be accurately estimated.

Passive Regenerator Experiments

Fig. (4.3.2) and Fig. (4.3.3) show results typical of experiments where helium was cycled through the regenerator cure without cycling the magnetic field. These experiments were conducted to provide a baseline for comparison with the active regenerator data. Fig. (4.3.2) shows the first three cycles of the run and Fig. (4.3.3) shows the $20^{\underline{th}}$ through $23^{\underline{rd}}$ cycles of the same run. The displacer and compensator strokes were both 3.8 cm during the run.

Fig. (4.3.4) shows the motion of the shuttle mass as represented by the traces on figures (4.3.2) and (4.3.3) with a schematic representation of the experiment showing the corresponding portions of the cycle. When the trace is at its maximum value all the shuttle mass is in the hot-end of the experiment and conversely at its minimum the trace indicates the shuttle mass is in the cold reservoir. The slope of the trace is proportional to the instantaneous mass flow through the regenerator

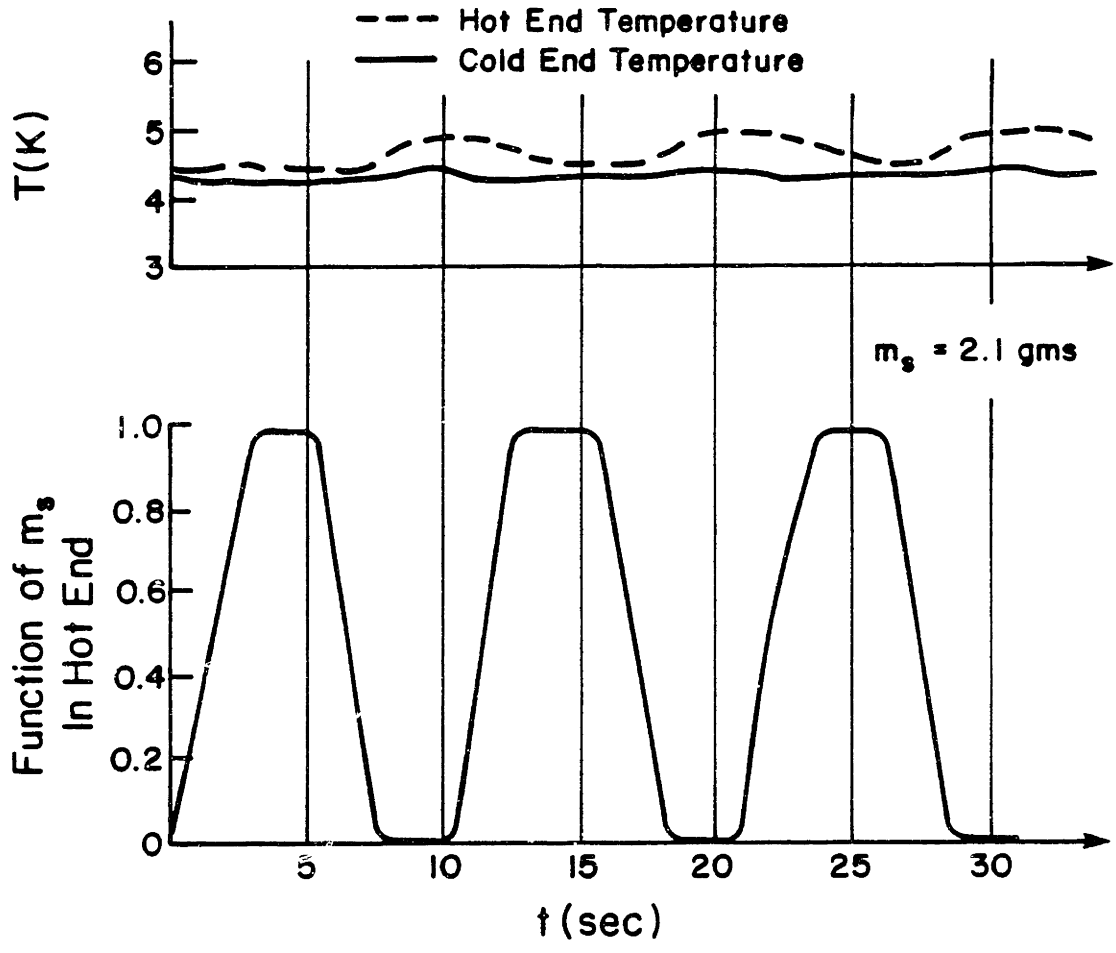

Fig. 4.3.2 Initial Cycles of a Passive Regenerator Experiment

core.

The run which is used for illustration contained 32 cycles. Averaged over all 32 cycles 0.02 W were rejected at the cold end and 1.3 W at the hot-end. Initially the hot and cold end temperatures are within 0.1 K of each other as shown on Fig. (4.3.2). As cycling starts the temperatures diverge and fluctuate cyclically. A cycling steady state is achieved by approximately 10 cycles (Fig. (4.3.3)). In the cycling steady state the hot-end temperature is hotter than the cold-end temperature by an average of approximately 0.6 K. In addition, the temperature of the cold and the hot end rise and fall in phase with each other with the same period as the mass flow cycle. The peak temperatures are reached when the shuttle mass is all in the cold reservoir. The magnitude of the warm end temperature oscillation is approximately 0.4 K, roughly twice the magnitude of the cold end fluctuation.

External heat leaks could not explain the data because the temperatures of both reservoirs rose above the ambient temperature of 4.2 K. Viscous heating within the core was estimated using the relationship for steady laminar flow.

$$\frac{\partial T}{\partial x} = \left(\frac{8\mu\bar{v}}{d^2\rho c} \right) \tag{4.3.2}$$

The temperature gradient due to viscous heating is $(\partial T/\partial x)$, the variables ρ, μ, and c refer to the density, viscosity, and specific heat of the working fluid. The passage half-width is d and the mean fluid velocity is $\bar{v}$. Eq. (4.3.2) predicts fluid friction will generate less than 1×10^{-3} K temperature rise through the core.

Compression Effect

Because the hot and cold temperatures rise and fall in phase a pressure cycling effect was suspected. The experiment is designed to operate with the hot reservoir at 10 K and the cold reservoir at 4.2 K. If the system pressure is maintained at 3 atm there is a 10-fold difference in density as the working fluid shuttles between the reservoirs. The cross-sectional area of the displacer is nearly eight times the area of the compensator so that the two pistons will have aproximately the same stroke lengths when operating at the design conditions.

The hot and cold reservoir temperatures for the run being discussed differed by

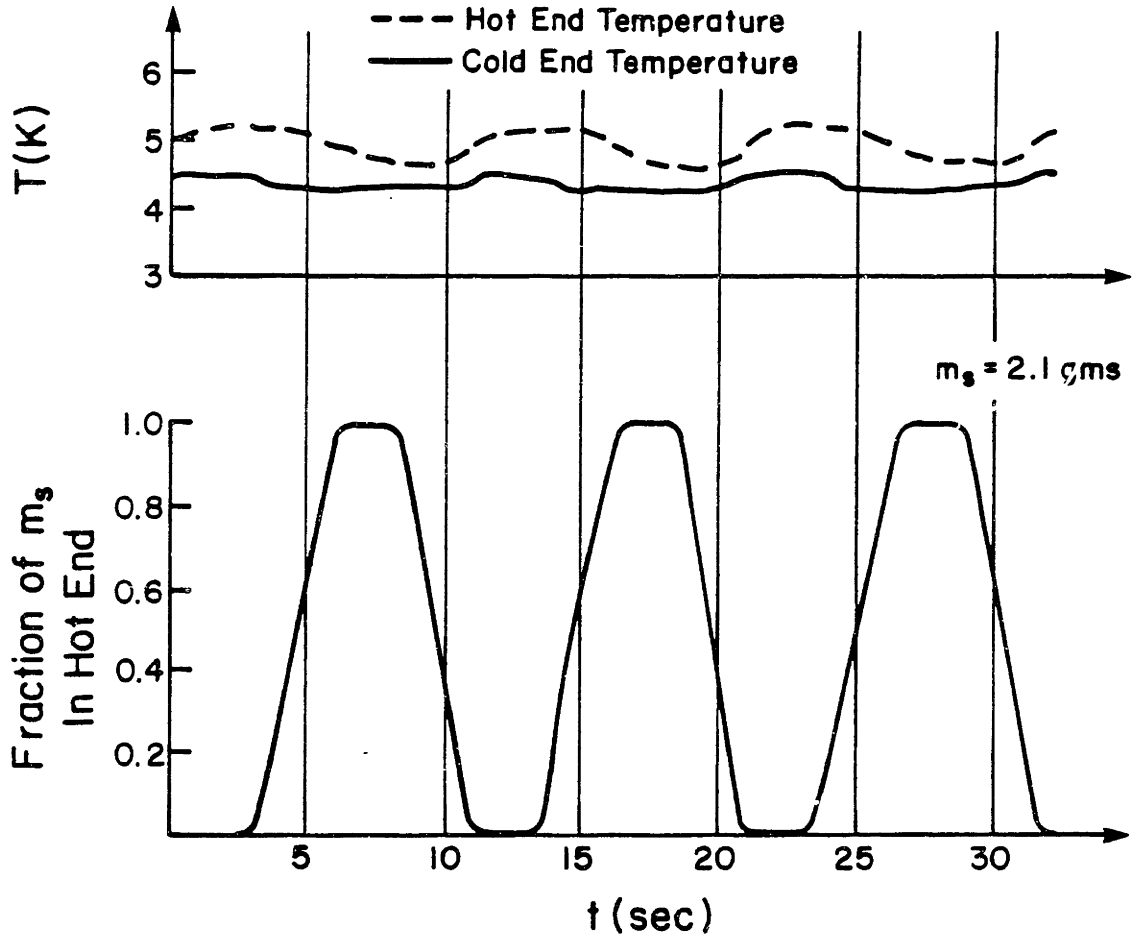

Fig. 4.3.3 Later Cycles of a Passive Regenerator Experiment

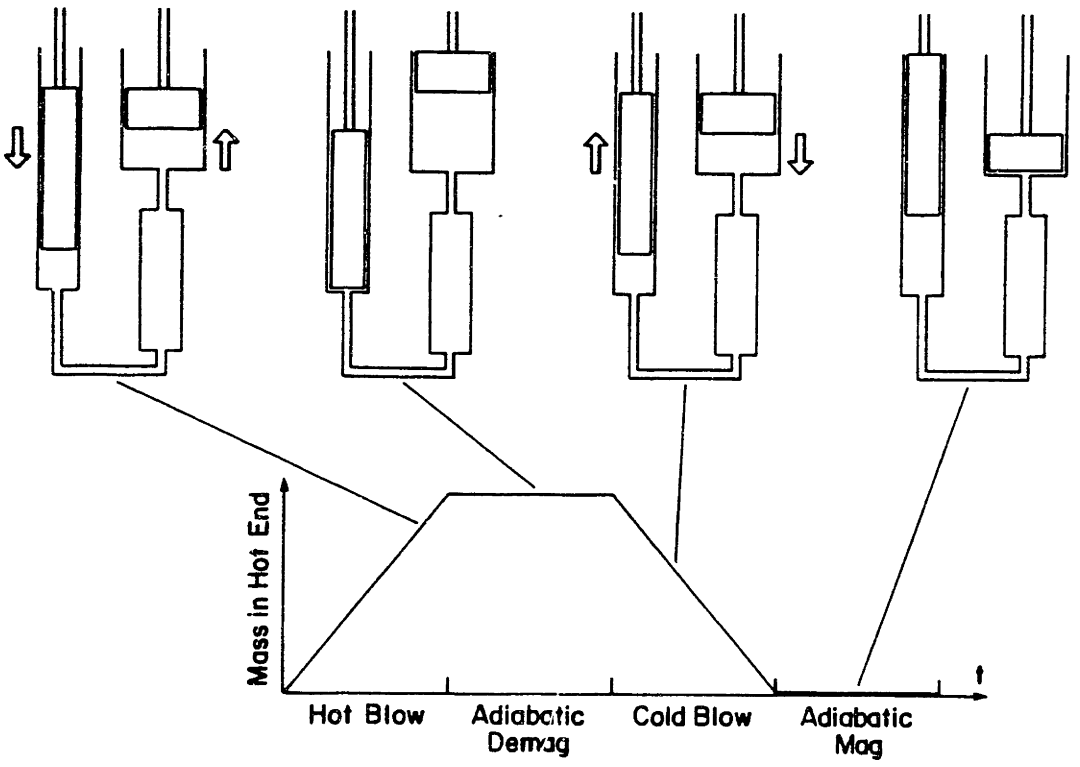

Fig. 4.3.4 Interpretation of Mass Flow Data

less than 1 K, however both the displacer and compensator were stroked 3.8 cm. The resulting change in system volume from the top of the dispacer stroke (Fig. (4.3.4), second frame) to bottom of displacer stroke (Fig. (4.3.4), fourth frame) is 265 cm^3, which far exceeds the volume change required by the 1 K temperature swing. The total system volume must be calculated to estimate the compression effect. Table (4.3.1) shows the distribution of volume in the working space of the refrigerator. The total system volume with the displacer piston at the bottom of its stroke and the compensator 3.8 cm from the bottom is 850 cm^3, this was the minimum volume for the run.

As a zeroth-order estimate on the compression effect, the entire gas volume was assumed to start at the maximum volume and 4.5 K then compress isentropically to the minimum volume. This estimate predicted a final pressure of over 75 atm and a

Table 4.3.1 Distribution of Refrigerator Working Volume

Component	Volume [cm^3]
10 K heat exchanger tubes	106
10 K heat exchanger headers	147
hot-end plumbing	60
regenerator core	14
compensator working volume	58
compensator clearance volume	62
displacer clearance volume	91
displacer dead volume	205
charging line *etc.*	78
total	856

temperature of approximately 8 K. The other extreme is to estimate the compression effect as isothermal which would result in a final pressure of 60 atm. Since the indicated charging pressure never varied more than ± 0.3 atm, this presented a mystery. The most obvious explanation would be to assume a leak in the compensator or displacer seals allowing working gas to escape through the backing gas regulator. However, no leaks could be found in the system.

A more involved analysis was performed which separated the working fluid into two parts; one which had a high temperature and thus high compressibility, and the other part having low temperature. The high temperature volume consisted of the charging line and the gap volumes of the displacer and compensator. The rest of the volume was assumed cold. The two volumes were modeled as going through separate isentropic compressions but coupled by mechanical equilibrium. This analysis was also unable to predict the experimental results.

It appeared from the experimental data that a large compliance must exist somewhere in the system. The compliance of the system would be greatly increased if the $3,100\,cm^3$ vacuum space inside the hollow displacer piston (Fig. (4.1.2)) were connected to it. The compliance would be increased not only because of the large additional volume but also because the volume would be relatively warm.

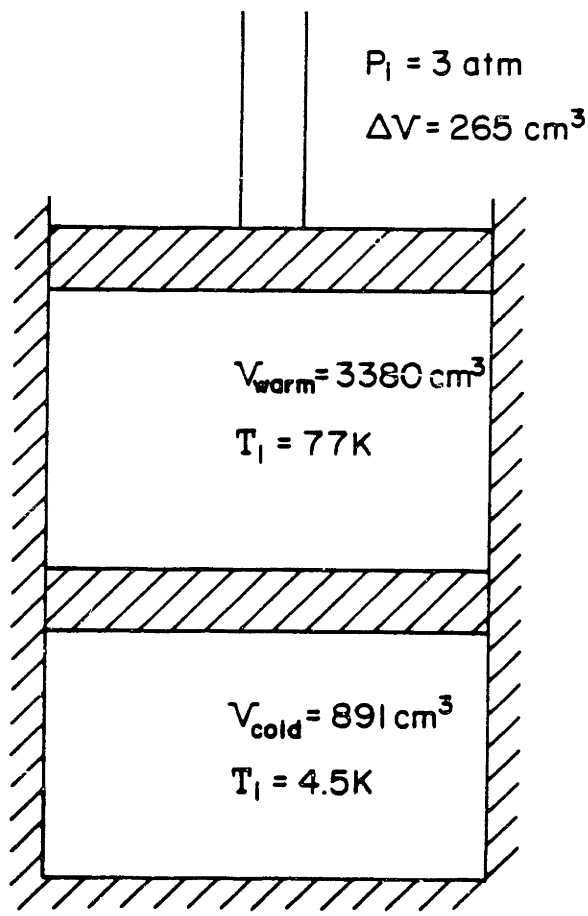

Fig. 4.3.4 Two Part Model of Working Volume

The system model used to evaluate the effect of connecting the displacer vacuum volume to the working volume is shown on Fig. (4.3.4). The initial warm volume is 3389 cm^3. The warm volume gas is assumed to have an initial temperature of 77 K. The cold volume starts at 891 cm^3 and 4.5 K. The two volumes, initially in equilibrium at 3 atm, are compressed isentropically by 265 cm^3 while maintaining mechanical equilibrium between the two. The resulting cold temperature swing is approximately 0.15 K and the pressure swing is about 0.5 atm. Obviously this extremely crude model cannot be expected to show quantitatively accurate results. However, the qualitative results are convincing. The hot-warm end temperature measured in the experiment had larger temperature fluctuations than the cold-end. This is probably due to the rapid increase in compressibility for temperatures above 5 K. Furthur support for the rudimentary analysis came when the experiment was disassembled and a large leak from the dispacer internal volume to the cold space was revealed.

Active Regenerator Experiments

This section discusses the experiments conducted with circulating helium and time-varying magnetic field. The results from the preliminary experiments are very encouraging. Steady refrigeration powers of .372 Watts at 3.87 K and 0.402 Watts at 3.78 K have been produced from sink temperatures of 5.7 K and 5.5 K respectively. Cycling steady state was arrived at after only four or five cycles. The performance of the device was very sensitive to the timing of the magnetic field changes and much less sensitive to variations in the mass flow.

The same magnetic field waveform was used throughout the first experiments (Fig. (4.3.5)); a constant slope form ramping from 1 T to 4 T in 5.25 seconds then back to 1 T in the next 5.25 seconds. This waveform was chosen because it was the fastest design sweep rate for the magnet†.

† The magnet has run at 0.5T/sec between 2 T and 5 T which could extract more cooling from the magnetic refrigerant.

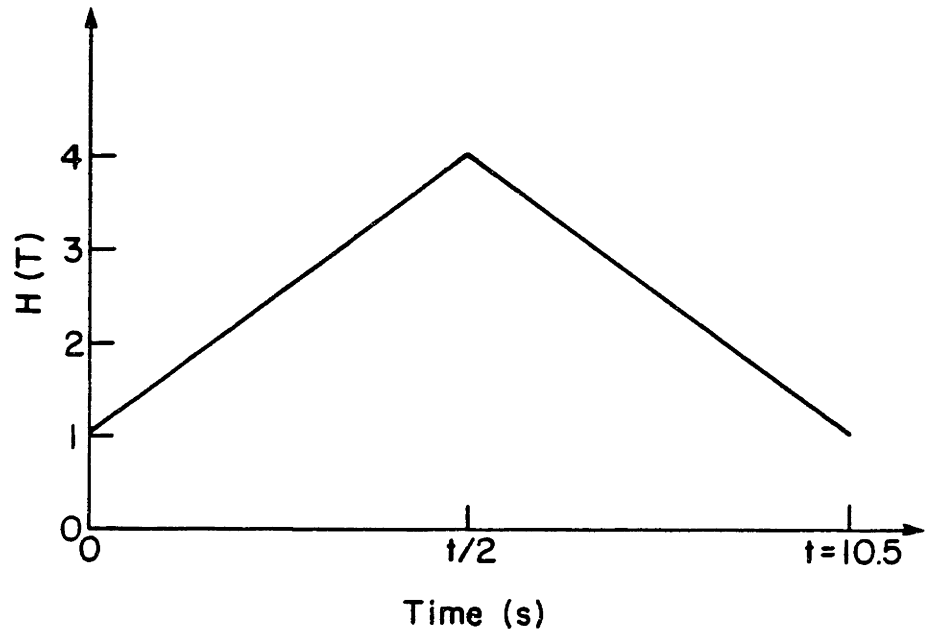

Fig. 4.3.5 Magnetic Field Waveform for the First Experiments

Two runs produced refrigeration. In one the displacer and compensator stroke were both 3.8 cm, in the other they were 5.1 cm. In both runs the magnetization and demagnetization half cycles were divided into flow and nonflow processes of equal duration. Fig. (4.3.6) shows the mass and field waveforms for the low mass flow run and Fig. (4.3.7) shows the equivalent waveforms for the high mass flow run.

The mass waveforms (dashed traces) on Figs. (4.3.6) and (4.3.7) depict the amount of shuttle mass, in grams, present in the hot reservoir. The dashed trace represents the amount of the shuttle mass present in the warm reservoir. The mass in the hot reservoir is assumed to be the complement of the mass in the cold reservoir, which is calculated by the compensator volume and an assumed state of 3 atm and 4.2 K. The average mass flow rates during the flow processes for the two runs were $1.1\,g\,s^{-1}$ and $2.0\,g\,s^{-1}$ respectively. Fig. (4.3.8) shows the $20^{\underline{th}}$ through $23^{\underline{rd}}$ cycles out of the 33 cycles in the $2.0\,g\,s^{-1}$ run. The plot shows the magnet current amount of shuttle mass in the hot reservoir and temperatures of the helium

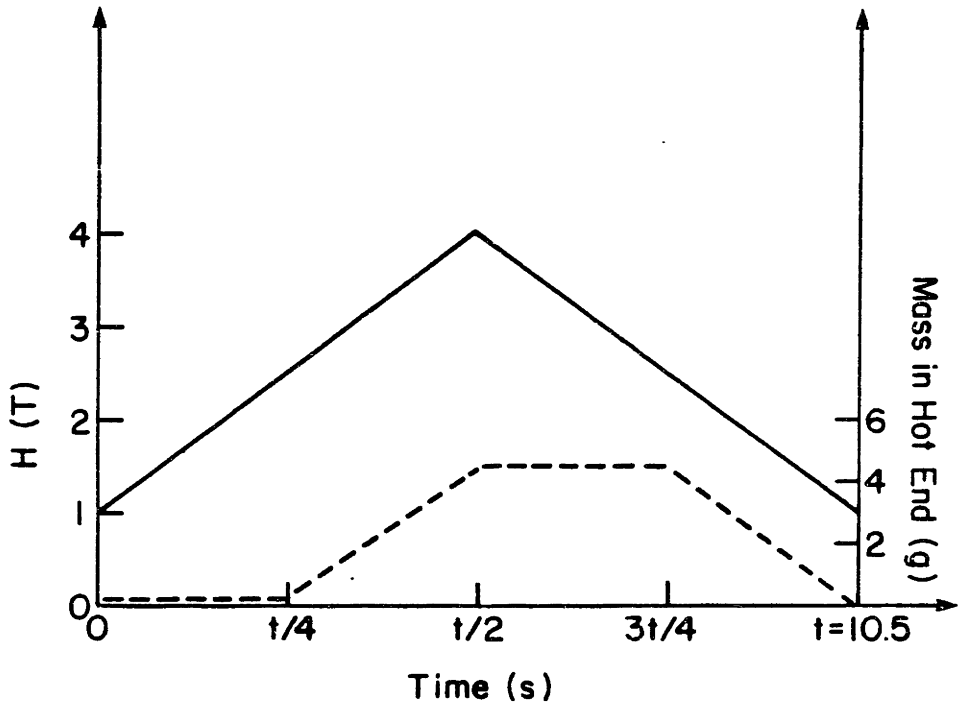

Fig. 4.3.6 Mass and Field Waveforms for $m_s = 4.5$g

at either end of the core.

The refrigeration provided to the cold reservoir and heat rejected to the hot reservoir were calculated (as described for the zero-field experiments) by converting the temperature data to enthalpy and numerically integrating the enthalpy fluxes for each cycle, for each end of the core. The net refrigeration to the cold reservoir is calculated as the enthalpy entering the cold end of the regenerator on a hot blow less the enthalpy exiting the cold end of the core during a cold blow. The net rejection is the enthalpy exiting the hot end of the core on a hot blow less the enthalpy returned to the hot end of the regenerator on a cold blow.

As can be seen from Fig. (4.3.8) the reservoir temperatures were not steady throughout the cycle. The cold-end reservoir temperature was estimated as the steady temperature of 3 atm helium which would transport the same enthalpy to the bottom of the regenerator core during a hot blow (flow from cold reservoir to hot reservoir during magnetization) as the actual stream.

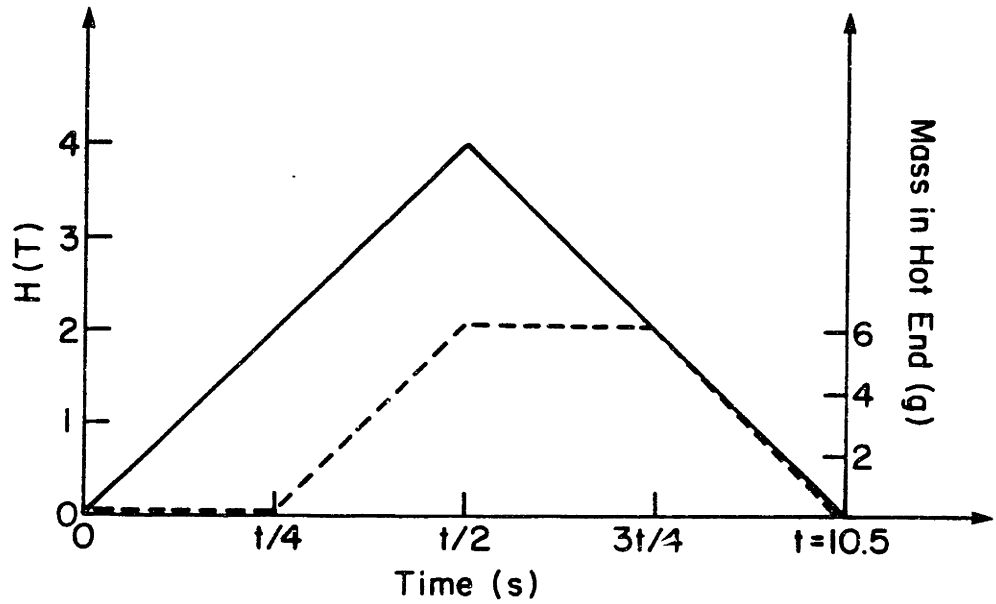

Fig. 4.3.7 Mass and Field Waveforms for $m_s = 6.25$g

$$T_{cold} = T_{cold}\left(\left(\frac{\int h\,dm}{m_s}\right)_{mag}, P\right) \tag{4.3.3}$$

Similarly the hot-reservoir temperature is approximated as the steady temperature, which at 3 atm would carry the same enthalpy as the cold-blow stream as it enters the top of the core.

$$T_{hot} = T_{hot}\left(\left(\frac{\int h\,dm}{m_s}\right)_{demag}, P\right) \tag{4.3.4}$$

The calculations were performed on the last 29 cycles of the 33 cycle 2.0 g s^{-1} run. The first 4 cycles of the run had not established a cyclic steady state. The results of the analysis show an average of 0.39 W of refrigeration provided to a cold reservoir whose average temperature is 3.9 K. Average power of 3.0 W was rejected to a 5.7 K warm reservoir.

Sources of Error

The actual performance of the magnetically active regenerator differs from the

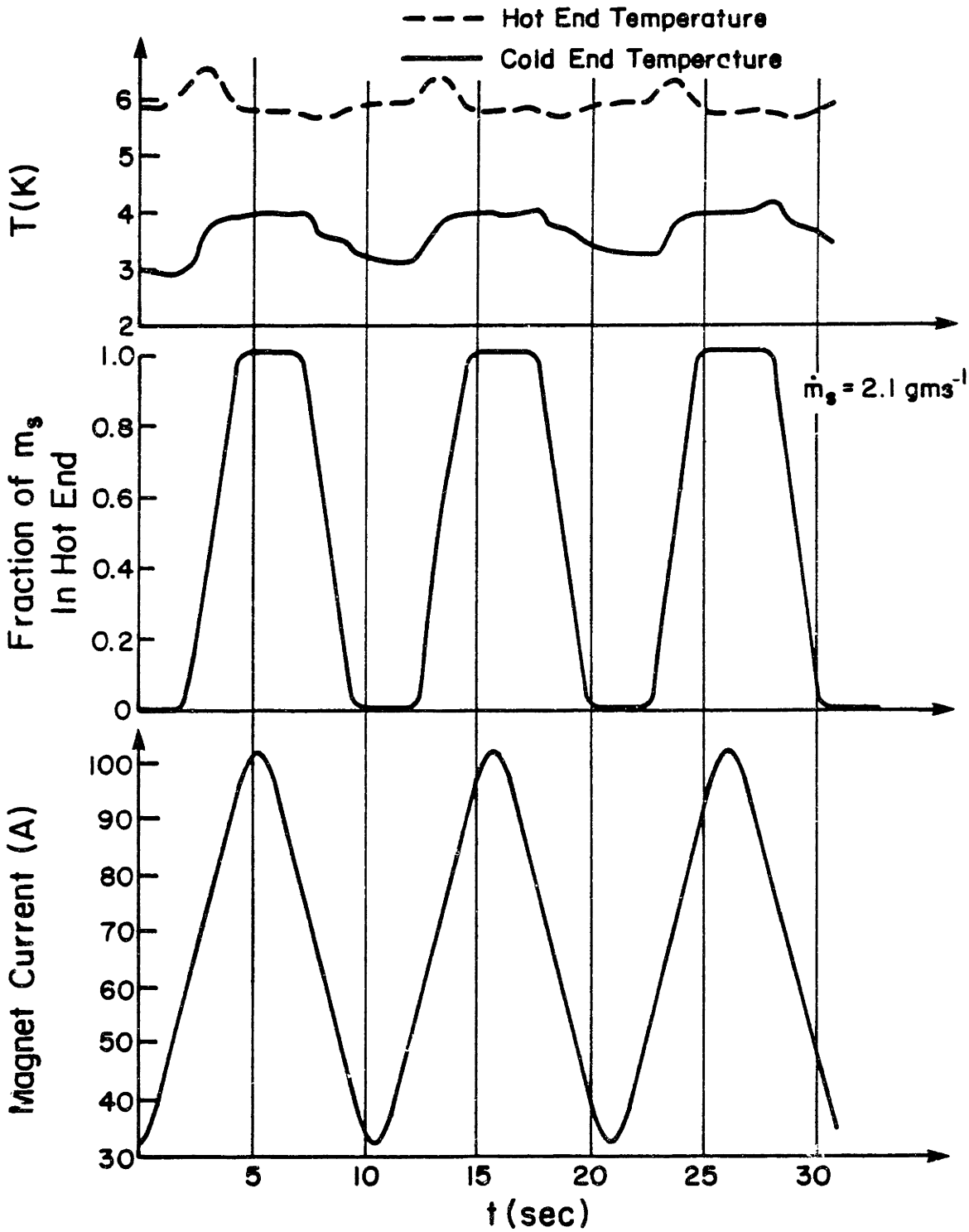

Fig. 4.3.8 Data from the 2.0 g s^{-1} run

results presented. The causes for the disparities can be grouped into two categories: one source is errors in measurement and calculation, the second is corruption of the experimental quantities by phenomena extrinsic to the experiment.

Compression Effect

An example of the latter is the compression phenonmenon discussed in the nonflow experiments. The mechanical work input produced by the motion of the displacer and compensator is out of phase with the magnetic work input to the regenerator core. As a result, the compression effect tends to heat the working fluid on a cold blow and cool it on a hot blow. Consequently, the compression phenomenon lowers the refrigeration produced by the magnetic effect. It is not possible to simply quantify the compression effect contribution to the measured results because of its complicated interaction with the magnetic work mode. The loss of refrigeration due to the compression effect is probably small. The refrigeration loss measured in zero-field experiments with the same mass flow was 0.02 W as reported earlier. The greater temperature difference between the reservoirs in the active field experiments makes a larger density difference between the hot and cold reservoirs and therefore reduces the compression work.

Interpretation of Temperature Data

Sensor errors are examples of the former class of inaccuracies in interpreting the data. Two sources of temperature measurement errors are magnetoresistance of the carbon temperature sensors and transient thermal sensor lag.

Field Effect

As mentioned earlier, the resistance of the carbon sensors increases with the applied field. Therefore, the indicated temperature measured in magnetic field is lower than the actual temperature. Lake Shore Cryotronics, the manufacturer of the carbon glass thermometer used to measure the hot end temperature, predicts a field dependent error of 0.05 K at 5 K and 4 T (actual temperature = 5.05 K, indicated temperature = 5.00 K). The magnetic field error increases with field and decreases rapidly with increasing temperature, becoming insignificant at temperatures above 10 K.

Because the hot blow takes place at higher average field than the cold blow (Fig. (4.3.6) and Fig. (4.3.7)), the indicated hot-blow temperatures are underestimated more than the indicated cold-blow temperatures. Helium's enthalpy increases monotonically with temperature. Therefore, the actual net rejection is larger than the indicated rejection and similarly the net actual refrigeration is larger than the indicated refrigeration.

Time Lag

Another source of error in the interpretation of time-dependent temperature data is sensor lag. Fig. (4.3.9) shows the $29^{\underline{th}}$ through $31^{\underline{st}}$ cycles of the 37 cycle $1.0\,g\,s^{-1}$ run. The temperature data on this figure shows that both the hot and cold temperatures are unsteady particularly during the flow processes. If the sensor's transient response is slow, the temperature will not be accurately recorded.

The finite thermal response time of the resistance thermometers can be approximated as a first-order lag. The published data for sensors similar to the CGR in helium vapor at 4.2 K indicate time constants varying from 32 ms to 200 ms[34]. If the actual temperature surrounding the probe varies linearly with time then the error between the measured signal and the actual temperature is

$$T_{actual} - T_{measured} = \dot{T}\tau(1 - e^{-(\frac{t}{\tau})}). \qquad 4.3.5$$

where $\dot{T}$ is time rate of temperature change of the environment and τ is time constant of the probe. Eq. (4.3.5) assumes the probe and fluid are initially in equilibrium.

The ramp-following error for the hot-end temperature data of the $1.0\,g\,s^{-1}$ run (Fig. (4.3.9)) was estimated by Eq. (4.3.5) assuming an average value of $\dot{T}$ of $0.24\,k\,s^{-1}$. The ramp following error reaches a maximum after three or four time constants of between 0.008 K and 0.05 K depending on the value of τ. The temperature data on Fig. (4.3.9) shows that the hot and cold temperatures both rise during a hot blow and both fall during a cold blow. The lag of the sensors causes the indicated hot blow temperatures to be lower than the actual hot blow temperatures and the indicated cold blow temperatures to be higher than the actual cold blow

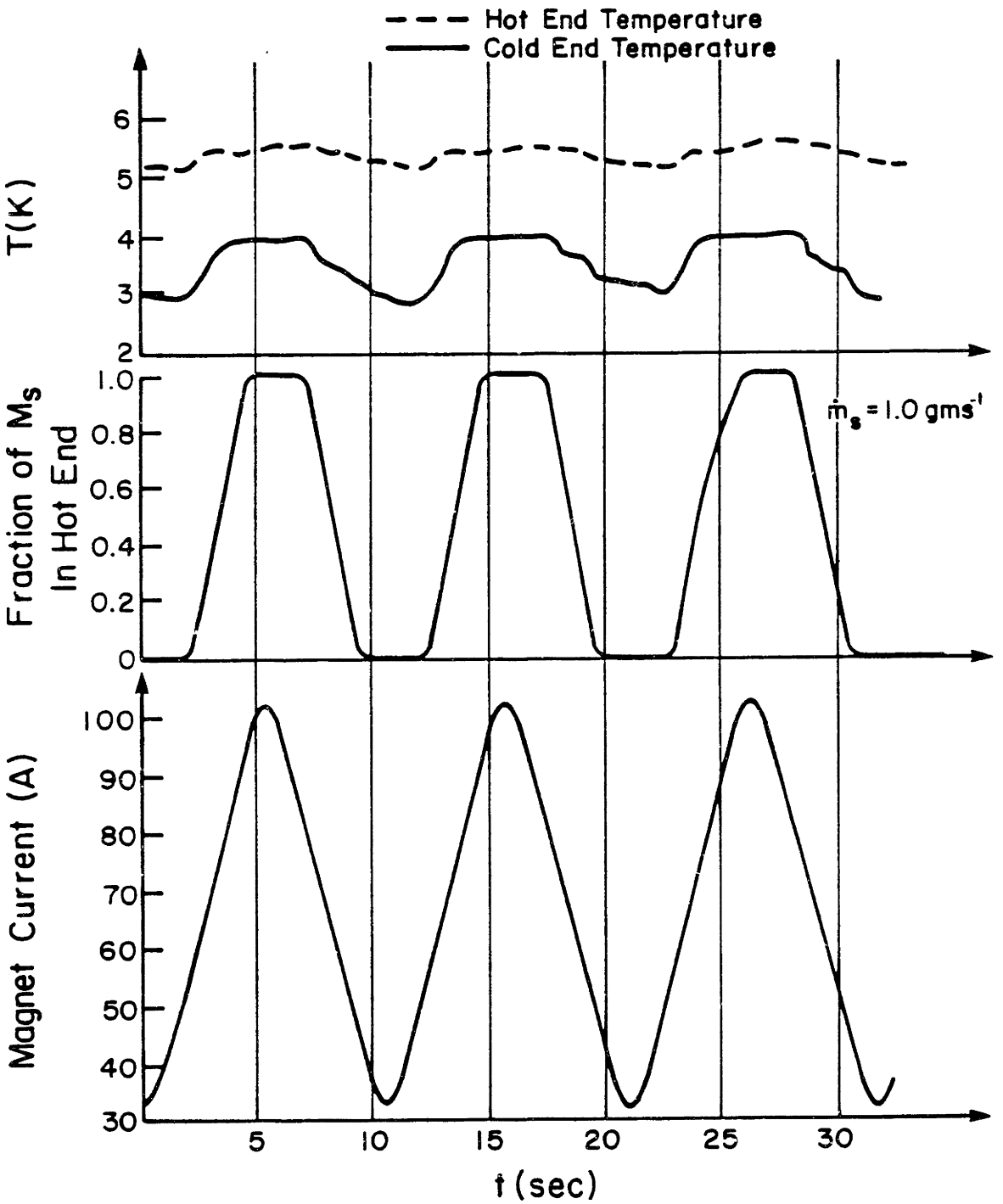

Fig. 4.3.9 Data From The $1.0\,g\,s^{-1}$

temperatures for both thermometers. The cold end thermometer has smaller sensor lag than the hot end thermometer because the 1/8 W resistors have smaller time constants due to their smaller size and higher density fluid environment. Like the effect of magnetoresistance, the sensor lag causes the calculated refrigeration and rejection both to be smaller than the actual values.

Specific Heat

The temperature errors produced either by magnetic field or by sensor lag are amplified in the calculation of the rejection and refrigeration by the multiplicative factor of the specific heat. The temperature error is particularly large in the calculation of the heat rejection for both the $1.0\,\mathrm{g\,s^{-1}}$ and $2.1\,\mathrm{g\,s^{-1}}$ runs where hot end temperatures are in the region of extremely high specific heat occurring above the saturation dome. The refrigeration calculation is less sensitive because of the faster transient response of the transducer and because of the lower specific heat at the cold end.

Corrected Data

Table (4.3.2) shows the calculated refrigeration, rejection, bath temperatures, and efficiencies for the $1.0\,\mathrm{g\,s^{-1}}$ and $2.0\,\mathrm{g\,s^{-1}}$ runs. The calculations are presented for both the raw data and for data which has been corrected for sensor lag and magnetoresistance.

The magnetoresistance was corrected using a linear approximation based on the manufacturer's data, with H expressed in tesla.

$$T_{\mathrm{actual}} = T_{\mathrm{measured}} \left(1 + 0.01 \frac{H}{4} \right) \qquad 4.3.6$$

The sensor lag was estimated assuming a $0.24\,\mathrm{k\,s^{-1}}$ temperature slew rate and sensor time constants of 200 ms and 32 ms for the hot and cold sensors respectively. The sensor lag for the hot sensor may be even larger than this estimate because the hot sensor leads (Fig. (4.3.10)) may influence the measured temperature more than the probe housing. The sensor leads are insulated from the flow by the heater spool. The efficiencies in Table (4.3.2) are calculated by Eq. (4.3.7).

Table 4.3.2 Refrigeration Performance

	$\dot{M} = 1.0\,[g\,s^{-1}]$		$\dot{M} = 2.1\,[g\,s^{-1}]$	
item [units]	raw data	corrected data	raw data	corrected data
T_{cold} [K]	3.78	3.84	3.87	3.92
T_{hot} [K]	5.51	5.51	5.71	5.71
$\dot{Q}_{rej}$ [W]	0.27	1.6	2.7	3.8
$\dot{Q}_{ref}$ [W]	0.40	0.41	0.37	0.43
η	2.1	0.36	0.21	0.16

$$\eta = \frac{Q_{refrigeration}/Q_{rejection}}{T_{hot}/T_{cold}} \qquad 4.3.7$$

The uncorrected efficiency of 2.1 for the $1.0\,g\,s^{-1}$ run is thermodynamically impossible. The crude corrections for magnetoresistance and transducer lag reduce this efficiency to 0.36. Although neither correction is larger than 0.05 K, the high specific heat at the hot-end temperature makes the calculation of $\dot{Q}_{rej}$ sensitive to small changes in temperature. The uncorrected efficiency for the $2.0\,g\,s^{-1}$ run is 0.21 while the corrected efficiency is 0.16. The $2.0\,g\,s^{-1}$ run is less effected by the correction because the specific heat at its hot reservoir temperature of 5.7 K is much lower than the corresponding specific heat for the $1.0\,g\,s^{-1}$ run.

Increasing the Performance of the Device

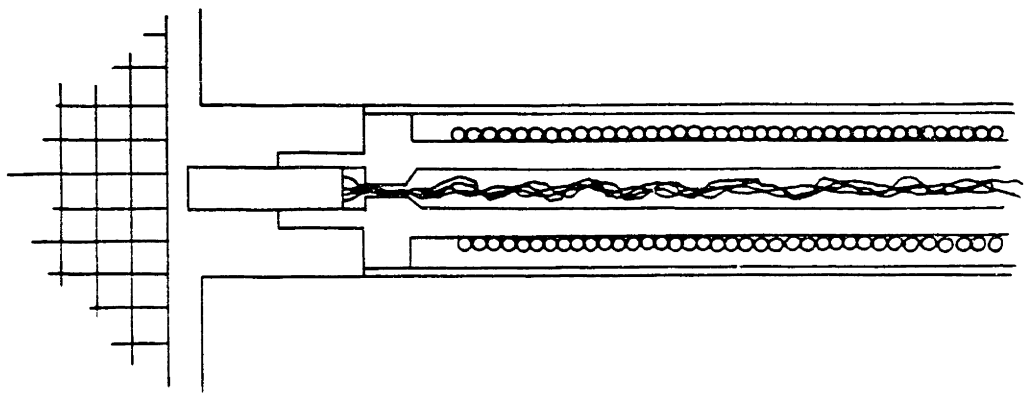

Fig. 4.3.10 Hot-End Temperature Transducer Mounting

The performance of the magnetic refrigerator demonstrated in the early experiments could be increased with several simple modifications to the apparatus. The mechanical work resulting from motion of the compensator and displacer was discussed in conjunction with the passive regenerator experiments earlier in this section. The mechanical work input is out of phase with the magnetic work. For example, as energy is removed from the system as magnetic work, energy is introduced to the system in the form of mechanical compression work. The interaction between the magnetic and mechanical work modes reduces the refrigeration. The mechanical compression loss could be eliminated by matching the strokes of the compensator and displacer to accomodate the actual density variation of the shuttle mass as it flows between the hot and cold reservoirs. Either sealing the leak in the displacer or implementing active control of the compensator could solve the problem.

The desired phasing between the mass flow and the magnetic field was not achieved in the preliminary experiments because of unanticipated lag in the magnet

controller.The computer program. which controls the input to both the displacer drive controller and the magnet controller, sent signals with the desired phasing to both controllers. The displacer drive stepper motor controller is an open loop circuit with nearly instantaneous response. However the magnet control loop has a lag of approximately one second. The computer program did not account for this delay. hence the magnet lagged the mass flow by about one second. The effects of this delay are illustrated by Fig. (4.3.11). The data of Fig. (4.3.11) are from a run identical to the $1.0\,g\,s^{-1}$ active regeneration experiment discussed previously except with a 1.5 s long nonflow process instead of a 3 s long one. The lag in the magnet controller caused the nonflow magnetization process to occur at the beginning of the cold blow instead of the end thus heating the core before the cold blow. Similarly the nonflow demagnetization was shifted so that it cooled the core before the hot blow. The run shown in Fig. (4.3.11) produced a net refrigeration of -1.35 W to the cold reservoir.

The magnet lag problem was present in all the preliminary runs. The $1.0\,g\,s^{-1}$ and $2.1\,g\,s^{-1}$ runs discussed earlier produced refrigeration only because their nonflow processes were longer and thus less effected by the lag in the field. The performance of the refrigerator would be greatly improved by elimination of the magnet lag. It is quite simple to eliminate the problem by having the software anticipate the lag and alter its outputs accordingly.

The reservoir temperatures during the preliminary experiments were unsteady both because of the mechanical compression phenomena and the fact that the temperature controllers were not functioning in these experiments. The unsteady reservoir temperatures cause larger stream-to-wall temperature differences in the core reducing system performance. Gallagher[22] has estimated the effect of magnet lag and unsteady reservoir temperatures using a numerical simulation of the magnetically active regenerator.

Conclusions

The results presented in this chapter demonstrate the successful implementa-

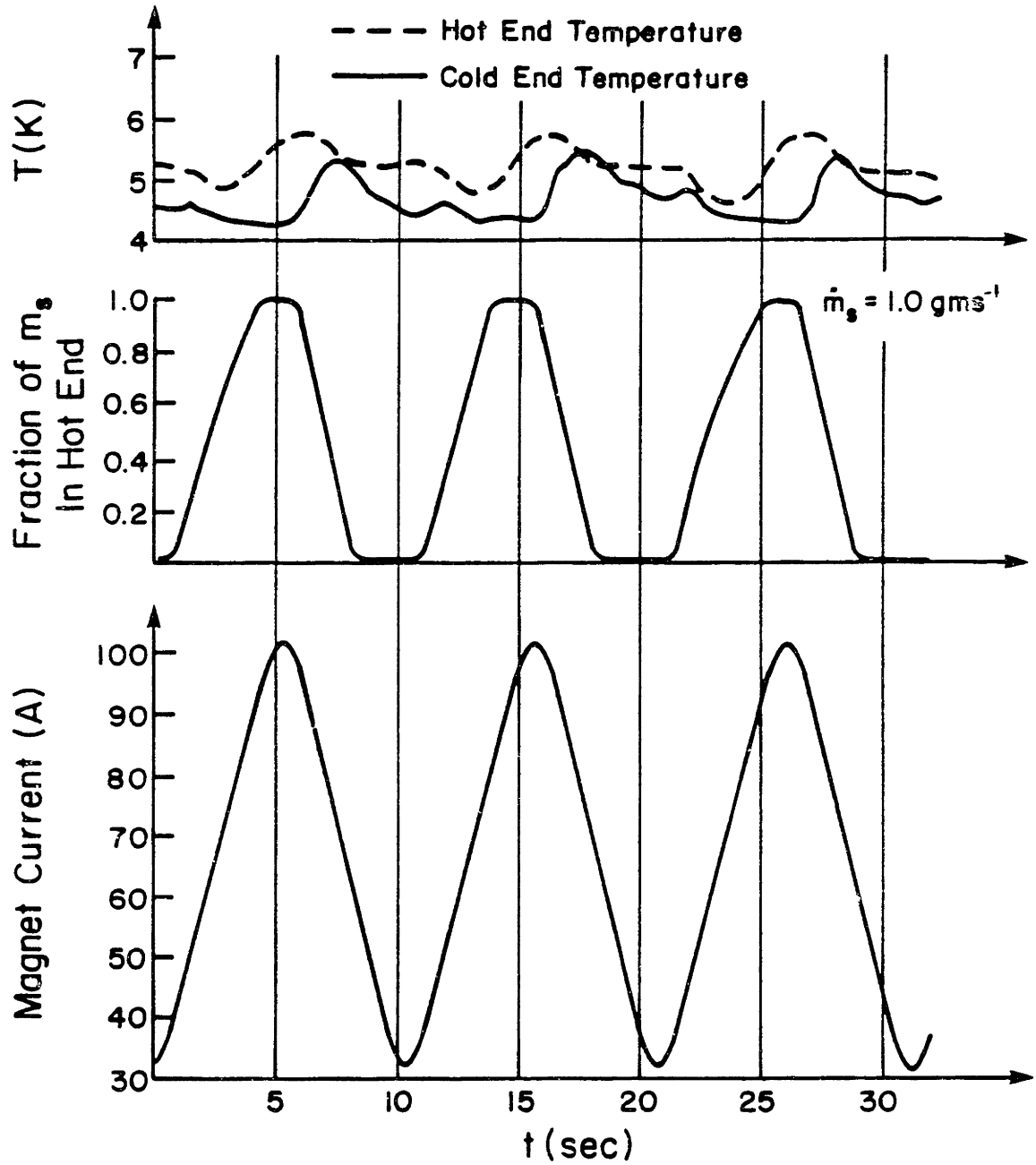

Fig. 4.3.11 Run Illustrating Loss of Performance due to Magnet Lag

tion of magnetically active regeneration. The performance of the experiment could be improved considerably by several simple modifications: elimination of the mechanical compression effect by improved compensator design, elimination of magnet lag by computer compensation, and use of the reservoir temperature controllers.

The experimental uncertainty could be greatly reduced by determining the temperature transducer lag via an *in-situ* measurement. The lag of the warm end transducer if found to be excessive could be easily reduced by changing its mounting design.

Further experiments must be carried out to establish the performance of the apparatus as a function of mass flow, relative timing of the processes, and temperature span of the cycle. Alternate cycles to the Carnot cycle may be more effective in obtaining the maximum useful refrigeration for GGG. The hybrid cycle shown on Fig. (4.3.12) replaces the isothermal demagnetization process of the Carnot cycle with an isofield process. The refrigeration for the hybrid cycle is greater for the same maximum and minimum field because it removes the same amount of entropy at a lower average temperature.

The preliminary nonflow field cycling experiments have suggested the possibility of a magnetic refrigerator with no moving parts. Buoyancy-driven circulation of the working fluid during magnetic field oscillations coupled with the "breathing" effect of the core generated by the changing density of entrained helium during magnetization and demagnetization produced refrigeration. Further investigation of this phenomenon is necessary to determine the amount of refrigeration and the best techniques to enhance the effect.

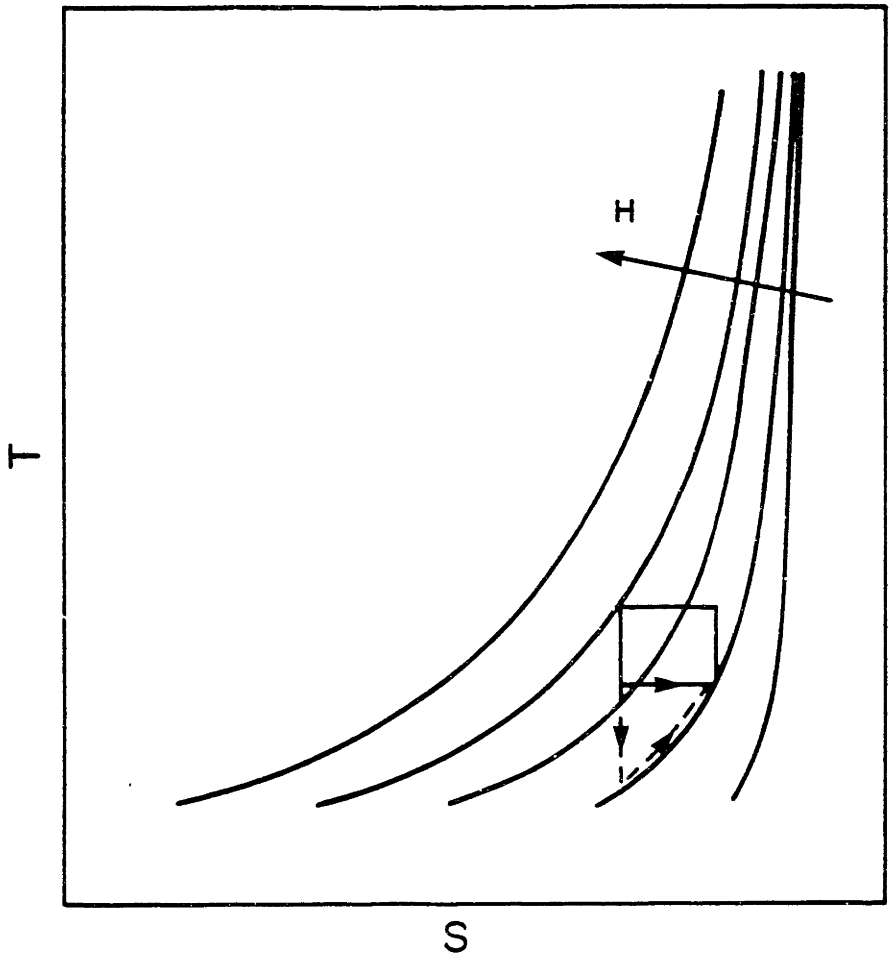

Fig. 4.3.12 Modification of Carnot Cycle for More Efficient Use of GGG

Appendix 1 Thermodynamics of a Magnetic Substance

The purpose of this appendix is to list some useful thermodynamic relationships for a magnetic substance, and to compare these relations with those of a compressible substance.

The $T\,dS$ relation for a magnetic substance was defined in Chapter 1 (Eq. (1.1.7)) and is repeated here.

$$dU = T\,dS + \mu_0 V H\, d\mathcal{M} \tag{A1.1}$$

Comparing Eq. (A1.1) with the $T\,dS$ equation for a compressible sustance,

$$dU = T\,dS - P dV, \tag{A1.2}$$

a useful analogy is revealed. The magnetic field intensity H is analagous to the pressure P of the compressible substance and likewise, the quantity $\mu_0 V\,\mathcal{M}$ is the analogue of -V.

In the remainder of this appendix the Maxwell relations and specific heats at constant magnetization and constant field intensity for the magnetic substance will be derived. At the end of the appendix the results will be summarized and presented with the analagous quantities for a compressible substance.

Beginning with Eq. (A1.1) the first Maxwell relation can be derived by noting that the differential dU can be expressed as a function of the independent variables S and $\mathcal{M}$. V

$$dU = \left.\frac{\partial U}{\partial S}\right|_{\mathcal{M}} dS + \left.\frac{\partial U}{\partial \mathcal{M}}\right|_{S} d\mathcal{M} \tag{A1.3}$$

The coefficients of the independent differentials in Eq. (A1.1) and Eq. (A1.3) must be equal, therefore

$$\left.\frac{\partial U}{\partial S}\right|_{\mathcal{M}} = T, \tag{A1.4}$$

and,

SOME TEXT ON THE FOLLOWING PAGE(S) IS
ILLEGIBLE ON THE ORIGINAL MATERIAL.

$$\left.\frac{\partial U}{\partial \mathcal{M}}\right|_S = \mu_0 V H. \qquad (A1.5)$$

Because the order of differentiation in the second-order mixed partial derivatives of U is irrelevant for surfaces with continuous first derivatives,

$$\frac{\partial^2 U}{\partial S\, \partial \mathcal{M}} = \frac{\partial^2 U}{\partial \mathcal{M}\, \partial S}. \qquad (A1.6)$$

The property expressed by Eq. (A1.6) can be applied to Eqs. (A1.4) and (A1.5) to derive the first Maxwell relation.

$$\left.\frac{\partial T}{\partial \mathcal{M}}\right|_S = \mu_0 V \left.\frac{\partial H}{\partial S}\right|_{\mathcal{M}} \qquad (A1.7)$$

The $T\,dS$ relation, Eq. (A1.1), can be transformed using the Legendre transformations to derive the remaining Maxwell relations. The magnetic enthalpy,

$$\mathbf{H}_{mag} = U - \mu_0 V H \mathcal{M}, \qquad (A1.8)$$

transforms the $T\,dS$ equation into the following form.

$$d\mathbf{H}_{mag} = T\,dS - \mu_0 V \mathcal{M}\, dH \qquad (A1.9)$$

Applying the technique used to derive Eq. (A1.6) the second Maxwell relation can be derived.

$$\left.\frac{\partial T}{\partial H}\right|_S = -\mu_0 V \left.\frac{\partial \mathcal{M}}{\partial S}\right|_H \qquad (A1.10)$$

The Helmholtz function,

$$F = U - TS, \qquad (A1.11)$$

transforms the $T\,dS$ equation to

$$dF = -S\,dT + \mu_0 V H\, d\mathcal{M}. \qquad (A1.12)$$

The Maxwell relation derived from the Helmholtz function is

$$-\frac{\partial S}{\partial \mathcal{M}}\bigg|_T = \mu_0 V \frac{\partial H}{\partial T}\bigg|_{\mathcal{M}}. \tag{A1.13}$$

Finally, the magnetic Gibbs function,

$$G_{mag} = U - TS - \mu_0 V H \mathcal{M}, \tag{A1.14}$$

provides the full Legendre transpose.

$$dG_{mag} = -S\,dT - \mu_0 V \mathcal{M}\,dH \tag{A1.15}$$

The final Maxwell relation is

$$\frac{\partial S}{\partial H}\bigg|_T = \mu_0 V \frac{\partial \mathcal{M}}{\partial T}\bigg|_H. \tag{A1.16}$$

The specific heat at constant magnetization is defined by

$$c_{\mathcal{M}} = T\left(\frac{\partial S}{\partial T}\right)_{\mathcal{M}}. \tag{A1.17}$$

The specific heat at constant magnetization can be expressed in terms of the other state variables by writing dU as a function of the independent variables T and $\mathcal{M}$.

$$dU = \frac{\partial U}{\partial T}\bigg|_{\mathcal{M}} dT + \frac{\partial U}{\partial \mathcal{M}}\bigg|_T d\mathcal{M} \tag{A1.18}$$

The $T\,dS$ equation can now be rewritten.

$$dS = \frac{1}{T}\left\{\frac{\partial U}{\partial T}\bigg|_{\mathcal{M}} dT + \left(\frac{\partial U}{\partial \mathcal{M}}\bigg|_T - \mu_0 V H\right) d\mathcal{M}\right\} \tag{A1.19}$$

The differential dS can be expressed in terms of the independent variables $\mathcal{M}$ and T.

$$dS = \frac{\partial S}{\partial \mathcal{M}}\bigg|_T d\mathcal{M} + \frac{\partial S}{\partial T}\bigg|_{\mathcal{M}} dT \tag{A1.20}$$

Equating the coefficients of dT in Eqs. (A1.19) and (A1.20) yields an expression for $c_{\mathcal{M}}$ in terms of the internal energy.

$$c_{\mathcal{M}} = T\left(\frac{\partial S}{\partial T}\right)_{\mathcal{M}} = \left.\frac{\partial U}{\partial T}\right|_{\mathcal{M}} \tag{A1.21}$$

Recasting dU and $d\mathcal{M}$ in Eq. (A1.1) in terms of independent variables H and T defines the specific heat at constant field intensity.

$$c_H = T\left(\frac{\partial S}{\partial T}\right)_H = \left(\left.\frac{\partial U}{\partial T}\right|_H - \mu_0 V H \left.\frac{\partial \mathcal{M}}{\partial T}\right|_H\right) \tag{A1.22}$$

The results of these derivations are summarized in Table (A1.1).

Table A1.1 Summary of Appendix 1

Magnetic Substance	Compressible Substance
H	P
$\mu_0 V\, d\mathcal{M}$	$-dV$
$dU = T\,dS + \mu_0 V H\, d\mathcal{M}$	$dU = T\,dS - P dV$
$\left.\frac{\partial T}{\partial \mathcal{M}}\right\|_S = \mu_0 V \left.\frac{\partial H}{\partial S}\right\|_{\mathcal{M}}$	$\left.\frac{\partial T}{\partial V}\right\|_S = -\left.\frac{\partial P}{\partial S}\right\|_V$
$\left.\frac{\partial T}{\partial H}\right\|_S = -\mu_0 V \left.\frac{\partial \mathcal{M}}{\partial S}\right\|_H$	$\left.\frac{\partial T}{\partial p}\right\|_S = \left.\frac{\partial V}{\partial S}\right\|_P$
$-\left.\frac{\partial S}{\partial \mathcal{M}}\right\|_T = \mu_0 V \left.\frac{\partial H}{\partial T}\right\|_{\mathcal{M}}$	$\left.\frac{\partial S}{\partial V}\right\|_T = \left.\frac{\partial P}{\partial T}\right\|_V$
$\left.\frac{\partial S}{\partial H}\right\|_T = \mu_0 V \left.\frac{\partial \mathcal{M}}{\partial T}\right\|_H$	$\left.\frac{\partial S}{\partial P}\right\|_T = -\left.\frac{\partial V}{\partial T}\right\|_P$
$c_{\mathcal{M}} = \left.\frac{\partial U}{\partial T}\right\|_{\mathcal{M}}$	$c_V = \left.\frac{\partial U}{\partial T}\right\|_V$
$c_H = \left.\frac{\partial U}{\partial T}\right\|_H - \mu_0 V H \left.\frac{\partial \mathcal{M}}{\partial T}\right\|_H$	$c_P = \left.\frac{\partial U}{\partial T}\right\|_P + P \left.\frac{\partial V}{\partial T}\right\|_P$

Appendix 2 Design of the Superconducting Solenoid

This appendix describes the design of the superconducting solenoid. The appendix's four sections describe: the geometry of the coil required to produce a given field, the power-supply requirements to operate the magnet at design specifications, the losses resulting from AC operation of the magnet, and the heat transfer requirements to dissipate the AC losses.

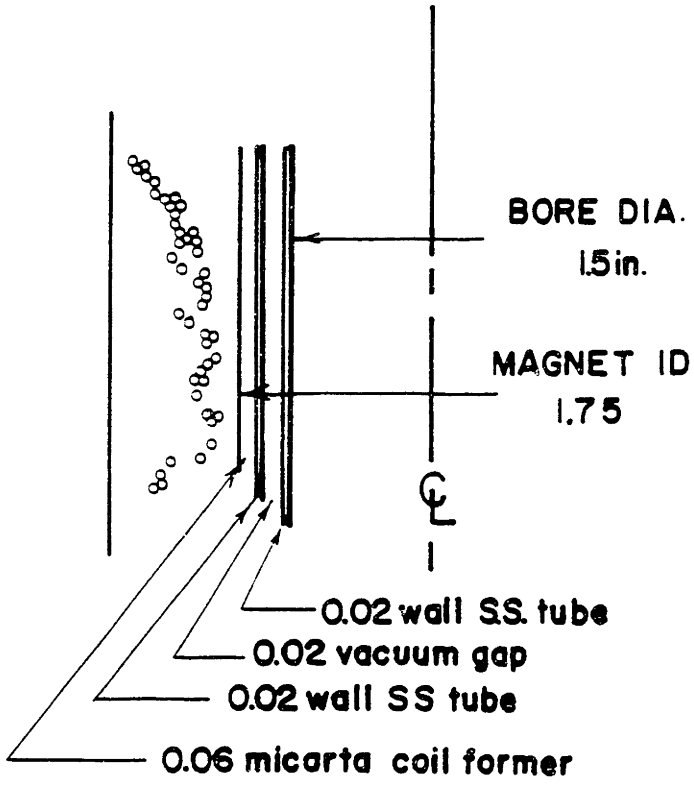

Fig. A2.1 Cross Section of Solenoid

The design of the magnet was restricted both by performance specifications and by geometric constraints. The magnet was required to produce a field uniform to within 5% in a volume defined by the outside diameter of the coil former (2.22 cm) and the length of the regenerator core (30.5 cm). The radial thickness of the coil former and the regenerator core vaccuum jacket within it were kept to a minimum to use as so that a maximum of the available magnetic field would be occupied

by the magnetic refrigerant (Fig. (A2.1)). The magnet was required to ramp at $\pm 0.5\,\mathrm{T\,s^{-1}}$ between 1 T and 4 T as shown by the waveform on Fig. (A2.2).

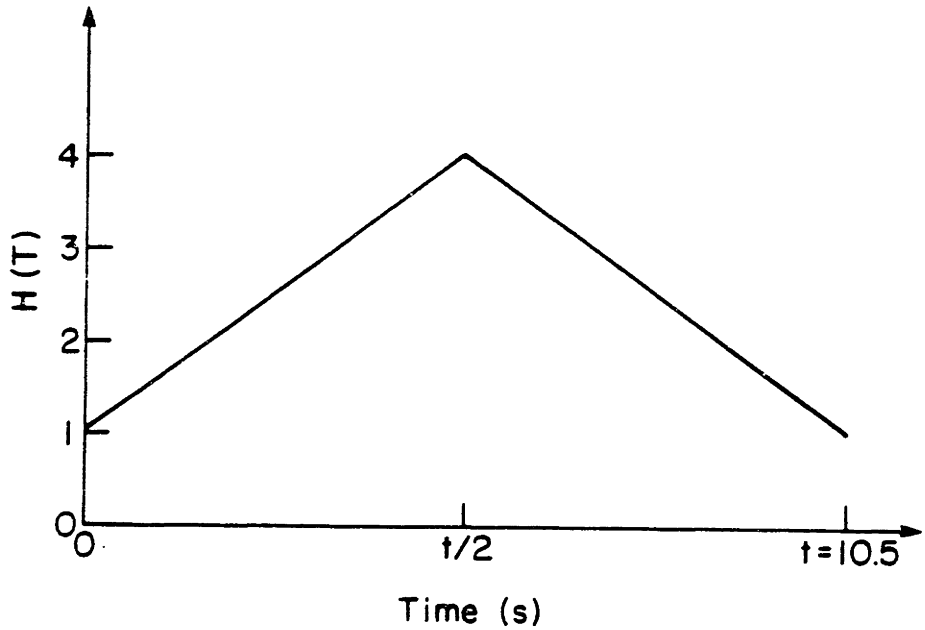

Fig. A2.2 Field Requirements for the Solenoid

The superconductor available for the solenoid was produced by the MCA corporation of Waltham, MA. It is a formvar-insulated niobium-titanium superconductor with a diameter of 0.69 mm. The superconductor has a copper-to-superconductor ratio of 1.8 and contains 2000 filaments of niobium-titanium each 9 μm in diameter. The twist pitch of the filaments is 8 mm. The wire has a critical current of 240 A at 5 T and 4.2 K. The superconductor cost \$ 0.49 per meter in Februrary of 1984.

Geometry of the Solenoid

The superconductor current density and the packing factor of the windings must be determined before designing the magnet. Because of the heat generated by the AC losses the coil was designed with internal cooling passages between the layers as opposed to the fully potted design typical of most small magnets. The

packing factor λ for a winding with wire diameter D and cooling passage width t, as shown on Fig. (A2.7), is

$$\lambda = \frac{(\frac{\pi D^2}{4})}{D(D+t)}. \qquad (A2.1)$$

The value of λ calculated by Eq. (A2.1) for a wire diameter of 0.68mm and an arbitrarily selected channel width of 100μm is 0.68. A packing factor of 0.6 was used in the design calculations to allow for unplanned spaces in the winding. To select an operating current density for the superconductor the designs of AC magnets of similar ratings found in reference (35) were examined. Based on these designs a current density, based on filament area, of 80,000 A cm^{-2} was selected. The overall current density J for the composite superconductor is found by dividing the filament based current density by the total area of the composite. The overall current density for this superconductor with its 1.8:1 ratio between copper matrix and niobium-titanium filaments is 28,500 A cm^{-2}.

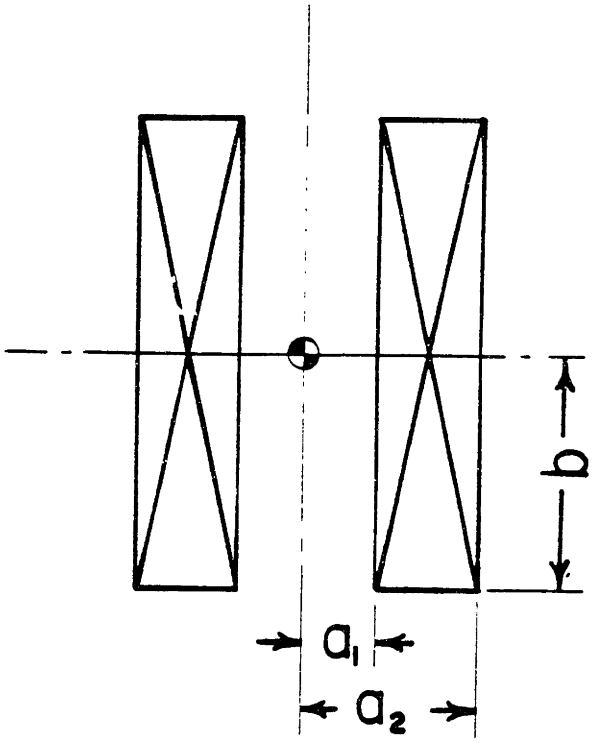

Fig. A2.3 Geometry of Center Section of Solenoid

Fig. (A2.3) shows the geometry used to describe a constant current density solenoid in reference (36). The bore radius of the solenoid a_1, the outer radius of the solenoid a_2, and its half-length b can be non-dimensionalized by the following two relations:

$$\alpha = \frac{a_2}{a_1}, \tag{A2.2}$$

$$\beta = \frac{b}{a_1}. \tag{A2.3}$$

Since the values of b and a_1 are already known β can be evaluated. The central field H_0 (in Oersted) can be expressed in terms of the current density in $\mathrm{A\,cm^{-2}}$, the magnet bore radius in cm, and the nondimensional variables λ, α, and β.

$$\frac{H_0}{J\lambda a_1} = \frac{4\pi\beta}{10} \ln\left(\frac{\alpha + \sqrt{\alpha^2 + \beta^2}}{1 + \sqrt{1 + \beta^2}} \right) \tag{A2.4}$$

Eq. (A2.4) can be used to find the value of α required to produce a center field of 40×10^3 Oersted (equivalent to an air-core magnetic induction of 4 T). The outer radius of the solenoid computed by Eq. (A2.4) is 4.1 cm. Eq. (A2.5) expresses the number of turns N required to wind the magnet in terms of the wire diameter, packing factor, and the gross geometry of the solenoid.

$$\frac{N\pi D^2}{4} = \lambda(a_2 - a_1)2b \tag{A2.5}$$

The length of the wire required ℓ_{wire} is a function of the mean radius $\bar{r}$ and the dimensions of the solenoid.

$$\ell_{wire} = 2\pi\bar{r}N \tag{A2.6}$$

Eqs. (A2.5) and (A2.6) predict that the main section of the magnet will require 9,317 turns of wire with a total length of 1.85 km.

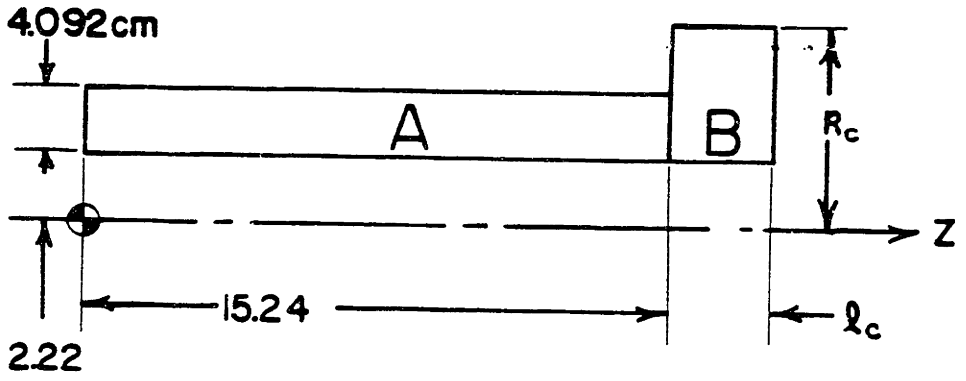

Fig. A2.4 Geometry of Compensating Coils

The next step in the design was to design the compensating coils which abut the main solenoid at either end as shown on Fig. (A2.4). The purpose of the compensating coils was to improve the homogeneity of the field in the active length of the magnet. To design the compensating coils the field intensity along the axis was calculated as a function of ℓ_c the length of the compensating coil, and R_c the outer radius of the compensation coil; the inner radius of the coils was assumed to be the same as that of the main coil. The Biot-Savart integral was used to calculate the field along the axis.

$$H_z(z) = \frac{1}{4\pi} \int_{a_1}^{R_c} \int_{b}^{b+\ell} \frac{\lambda J r^2 2\pi r \, dr \, dz'}{(r_{r'r}^2 + (z' - z)^2)^{3/2}} \qquad (A2.7)$$

The field at the end of the main section was calculated by superposition of the fields due to the main section and the compensating windings. The contribution of the compensating windings was calculated using the Biot-Savart integral presented previously. The contribution of the main section was aproximated using the long solenoid approximation that the end-field is half the center field. Eq. (A2.7) was evaluated numerically for various combinations of R_c and ℓ_c; values of 6 cm and 2 cm respectively were chosen. The resulting notch-type magnet has a field uniform within 6% in the active region. Each compensating coil contains 1,234 turns

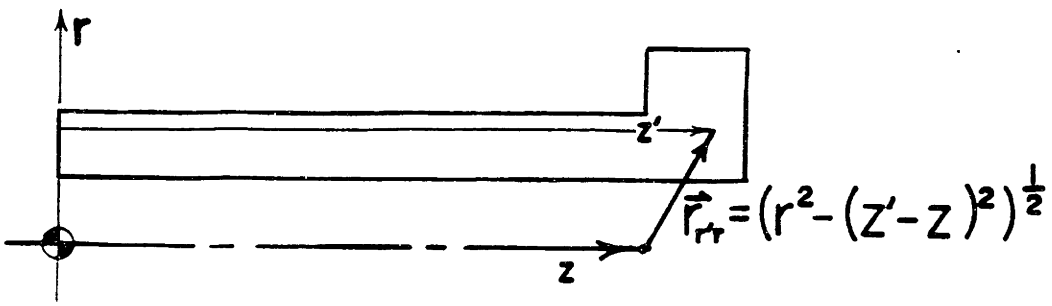

Fig. A2.5 Model Used For Evaluating Biot-Savart Integral

of superconductor, as calculated by Eq. (A2.5) and requires 0.32 km of wire (Eq. (A2.6)).

Power Supply Requirements

In order to estimate the power supply requirements, the inductance of the magnet must be calculated. The total inductance of the magnet was approximated as the sum of the self-inductances of the three individual components. The effects of mutual inductance were ignored and the susceptability of the paramagnetic core was ignored. The inductance was calculated by the formula in reference (36), defined as Θ.

$$L = a_1 N^2 \Theta(\alpha, \beta) \qquad (A2.8)$$

Eq. (A2.8) calculates the inductance of the main coil as 0.39 H and the inductance of each compensating coil as 0.17 H. A rough approximation of the total inductance of the magnet, given by the sum of the self-inductances, is 0.72 H. The voltage required to ramp the magnet up and down the linear waveform of Fig. (A2.2) is simply that required to change the current in an ideal inductor.

$$V = L\frac{di}{dt} \tag{A2.9}$$

Eq. (A2.9) predicts that a bipolar power supply capable of sourcing up to ±9.5 V for the full current range of the magnet is required to produce the waveform of Fig. (A2.2). The current requirement for the power supply is calculated by multiplying the current density J by the area of the wire.

$$I_{max} = J\frac{\pi D^2}{4} \tag{A2.10}$$

The current calculated by Eq. (A2.10) is 105 A.

AC Losses in the Superconductor

The hysteresis loss W_{hl} in Joules per cycle is calculated using the simple Kim model by the equation presented in reference (35).

$$W_{hl} = \frac{d\mu_0 I_0 H_0 \ell_{total}}{2} \ln\left(\frac{H_{max} + H_0}{H_{min} + H_0}\right) \quad . \tag{A2.11}$$

In Eq. (A2.11), H_{max} is the maximum field instensity, H_{min} is the minimum field intensity, ℓ_{total} is the total length of wire in the magnet, d is the filament diameter, I_0 is the zero field critical current, and H_0 is a material property of the superconductor. H_0 is the field at which the zero-field critical-current has been reduced by half. The Kim model predicts the following relationship between critical-current I_c and field.

$$I_c = \frac{I_0 H_0}{H + H_0} \tag{A2.12}$$

Eq. (A2.11) is subject to several assumptions. First, the superconducting filaments must be fully penetrated by the magnetic flux. Full penetration will be guaranteed if $H_{max} \gg J_c \frac{d}{2}$ where J_c is the superconductor critical current density. Second, the excitation frequency of the magnet must be slow enough relative to the relaxation time of the composite superconductor so that the inner filaments are not shielded by the outer ones. This requirement can be expressed by the inequality $\omega_{cyc} \ll \frac{1}{\tau}$ where ω_{cyc} is the angular frequency of the excitation and τ is defined below.

$$\tau = \frac{\mu_0}{2}\left(\frac{\ell_p}{2\pi}\right)^2 \frac{1}{\rho_c} \qquad (A2.13)$$

In Eq. (A2.13) ℓ_p is the twist pitch of the superconducting filaments and ρ_c is the composite resistivity of the superconductor defined by the following equation.

$$\rho_c = \rho_{cu}\left(\frac{w}{w-d}\right) \qquad (A2.14)$$

The quantity ρ_c in Eq. (A2.14) is the resistivity of the copper matrix. The dimension w is the separation distance of the superconducting filaments. Fig. (A2.6) shows the assumed hexagonal array geometry used to approximate the dimension w.

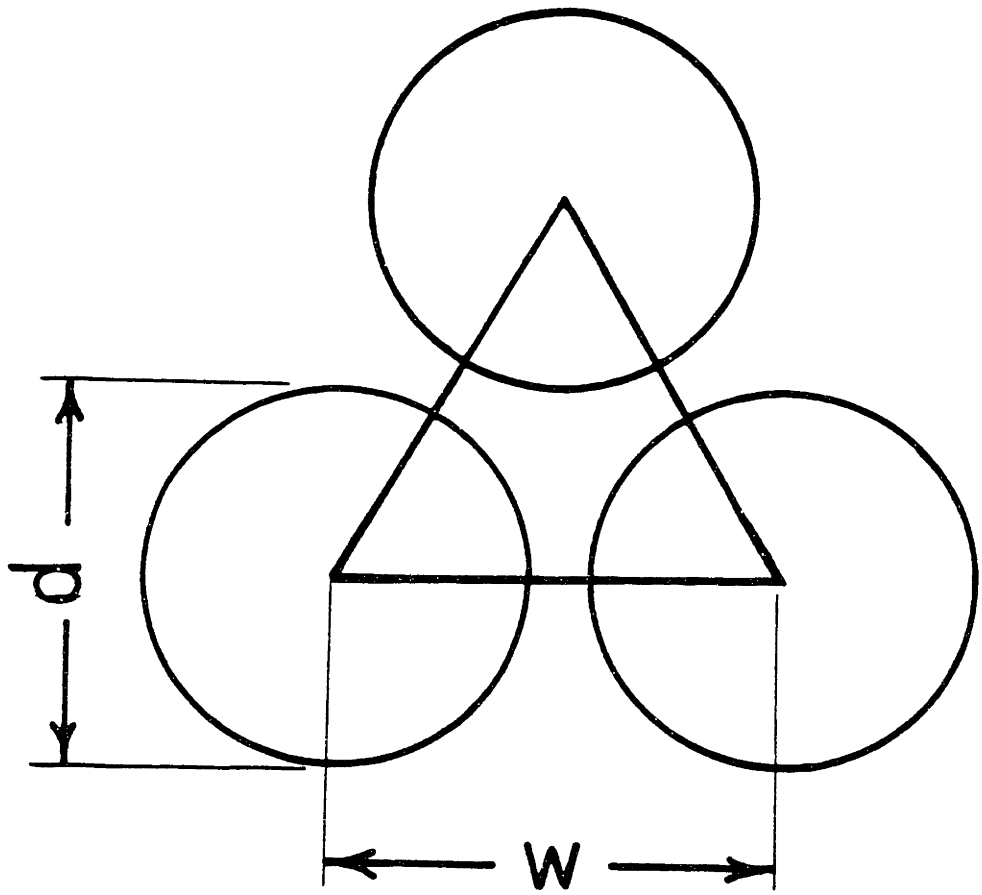

Fig. A2.6 Hexagonal Array of Superconducting Filaments

$$w = \sqrt{\frac{\pi(1+\Lambda)d^2}{4\cos(\frac{\pi}{6})}} \qquad (A2.15)$$

The quantity Λ in Eq. (A2.15) is the copper-to-superconductor ratio.

The two assumptions required to use Eq. (A2.11) are valid for this design because the maximum field H_{max} ($40 \times 10^4\,\mathrm{A\,cm^{-1}}$) is much larger than the minimum full flux penetration criterium $\frac{d}{2}J_c$ ($100\,\mathrm{A\,cm^{-1}}$, assuming a superconductor critical current density of $2 \times 10^8\,\mathrm{A\,cm^{-2}}$). The second assumption is also valid because the inverse of the relaxation time of the composite wire $\frac{1}{\tau}$ ($393\,\mathrm{s^{-1}}$) is much greater than the angular frequency of the excitation ω ($0.52\,\mathrm{s^{-1}}$). To evaluate Eq. (A2.11) the material property I_0 had to be determined. This was done using the Kim model approximation (Eq. (A2.12)) with an assumed value of H_0 of 10^4 Oersted, typical for niobium-titanium superconductors, and the manufacturer's critical current data (240 A at 50,000 Oersted). The resulting hysteresis loss calculated was 15.0 Joules per cycle or, operating at a frequency of 0.085 Hz, 1.25 W.

For the case where $\omega \ll \frac{1}{\tau}$ the eddy current losses $\dot{W}_e$ can be approximated in MKS units by the following equation from reference (35).

$$\dot{W}_e = \frac{\mu_0 (H_{max} - H_{min})^2 \omega^2 \tau \ell_{total} \pi D^2}{64} \qquad (A2.16)$$

Eq. (A2.16) predicts an eddy current loss of 0.29 W.

One other loss mechanism was considered which was the loss due to self-field W_{sf}. This loss is approximated in reference (35) by the equation

$$\frac{W_{sf}}{W_{hl}} \approx 0.65 \left(\frac{D}{d} \right)^2 . \qquad (A2.17)$$

Eq. (A2.17) predicts that the self-field loss is less than 4% of the hysteresis loss.

Heat Transfer Analysis

Fig. (A2.7) shows the geometry of the flow passages used in the heat transfer analysis. The figure shows two concentric layers of the winding separated by spacers of thickness t, angular width ϕ, and angular separation θ. The heat flux resulting from the AC losses must be dissipated in the cooling channels of the magnet. The resulting heat flux in the cooling channels $\dot{Q}''$ in terms of the wire diameter D and geometry of Fig. (A2.7) is

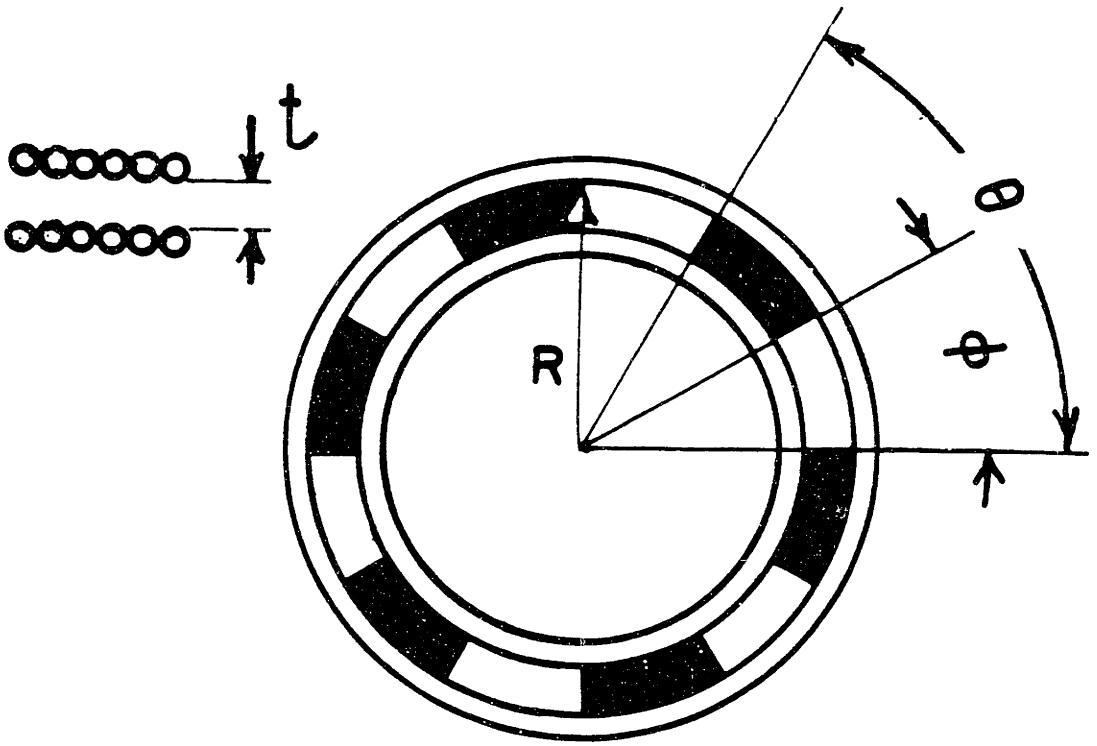

Fig. A2.7 Variables for Heat Transfer Analysis

$$\dot{Q}'' = \frac{w''' D}{4}\left(\frac{\theta}{\varphi}\right). \qquad (A2.18)$$

In Eq. (A2.18) w''' is the specific power dissipated by the coil. The critical heat flux for boiling helium in vertical channel flow is a difficult number to determine and depends strongly on geometry and surface conditions. Reference (37) gives the range of critical heat flux for saturated 4.2K helium as 0.35 W cm^{-2} to 0.45 W cm^{-2}. The heat flux predicted by Eq.(A2.18) is 9.3×10^{-5}W/cm^2, for an assumed value of (ϕ/θ) of 0.5, so it is not likely that cooling will be a problem.

Table (A2.1) summarizes some of the more important results from this appendix. Reference (27) presents the experimentally measured field profile, inductance, and AC losses of the magnet. The actual air-core inductance of the magnet is 1.2 H the other data in table (A2.1) is within 15% of the actual values.

Table A2.1 Magnet Data

Variable	Definition	Value [units]	Eq. or Constraint
a_1	magnet bore radius	2.22 cm	magnet size
a_2	main section outer radius	4.1 cm	A2.4
b	main section half-length	15.25 cm	regenerator core
R_c	comp. coil outer radius	6.0 cm	A2.7
ℓ_c	comp. coil length	2.0 cm	A2.7
ℓ_{total}	total wire length	2.49 km	A2.6
L	magnet inductance	0.72 H	A2.8
W_{hl}	hysteresis loss	1.25 W	A2.11
$\dot{W}_e$	eddy current loss	0.29 W	A2.16
t	interlayer spacing	100 μm	magnet cooling
I_{max}	max mag current	105 A	A2.10
V	magnet voltage	$\pm$9.5 V	A2.9

Appendix 3 Fabrication of The Regenerator Core

This appendix describes the materials and processes used to fabricate the regenerator core.

The GGG used to construct the regenerator started as a series of single crystals known as boules. The boules were ground into cylinders 38.1 mm $\pm$0.05 mm in diameter. Using an ID saw the cylinders were cut into discs 2.54 mm thick. The as-sawn surface finish of the discs (similar to a light sandblast finish) proved excellent for epoxy bonding. After the sawing operation, the faces of the disc were out of parallel by less than 0.1 mm across the diameter which obviated further processing.

Two manufacturers supplied the rough sawn GGG discs: Litton Industries Airton Division of Morris Plains NJ, and Materials Progress of Santa Rosa CA. At the time of this writing, GGG prices ranged between $3.00 and $3.50 per gram in single crystal disc form. Asingle disc of the GGG used in the experiment weighs 20.7 g.

The second step in the fabrication of the regenerator core was the lamination of the discs into cylinders 10 discs high. As described in Chapter 3 the purpose of laminating the discs is to reduce the axial conduction through the core.

The discs were laminated in groups of ten because this was the largest number that could be comfortably machined and handled at once. Initially, the discs were laminated with a wet-lay-up of fiberglas cloth and epoxy in each joint. It was thought that the fiberglas cloth would further reduce axial conduction and improve the strength of the joints by controlling the glue line thickness. The units glued together in this fashion delaminated when they were subsequently machined. It is possible that the coolant used in the machining process wicked into the fiberglas and weakened the joint. The remaining units laminated with the fiberglas were debonded with Miller-Stephenson epoxy stripper. The discs were then relaminated without fiberglas cloth and cured under 15 psi interface pressure at 65°C. The crystals laminated in this manner were machined without incident.

Micro Measurements M-Bond AE-15 epoxy system was chosen to laminate the crystal wafers because of its low thermal conductivity and its good cold strength.

Other cryogenic epoxies such as stycast 2850-CR are designed with fillers which enhance thermal conduction. The AE-15 epoxy had been used to mount strain-gages in cryogenic pressure transducers. The mechanical strength of AE-15 was tested by laminating two quartz wafers with it and temperature cycling the sample from room temperature to 77 K repeatedly. No cracking or delamination occurred.

At this stage of construction the regenerator core consisted of 12 segments each consisting of 10, 02.54 mm thick, 38.1 mm in diameter wafers laminated together with M-Bond AE-15 epoxy. Each segment was then sawn into 0.254 cm wide strips parallel to the cylinder axis. A high-speed diamond saw with full-flood cooling was used to cut the strips. The saw kerf of 1 mm only allowed 11 or 12 strips to be cut from a segment. The sawing and the subsequent lapping of the crystals were done by the Optikos Corporation of Cambridge MA.

The 12 segments had now each been sawn into 11 or 12 strips 2.54 mm thick and varying widths depending on the chord length where they were sawn (Fig. A3.1). The 12 segments were then concatenated in groups of three. The matching strips from each segment were glued end-to-end to form strips 30 wafers long. The strips were glued together on a surface plate, with gaps beneath the joints, with AE-15 epoxy. The long strips were then trimmed of excess epoxy and lapped flat and parallel.

The helium flow passages were created by stacking the strips back together in the sequence they were sawn from the segments but with shims at the edges providing a small gap between adjacent strips. 3M type 75 electrical tape, a 0.09 mm thick polyester film coated on both sides with a thermosetting adhesive, was used as the shimming material (Fig. (A3.2)).

G-10 (a fiberglas-epoxy composite) header plates were then fixed to each end of the core section. These plates were used in both the potting operation and the section-to-section joints. The plates (Fig. (A3.3)) are made from two G-10 discs. One disc is 0.3 mm thick and 38.1 mm in diameter. This disc is mounted concentrically on a 2.4 mm thick disc 45 mm in diameter with a thick sheet of paper between them. The paper would later be split to separate the two pieces.

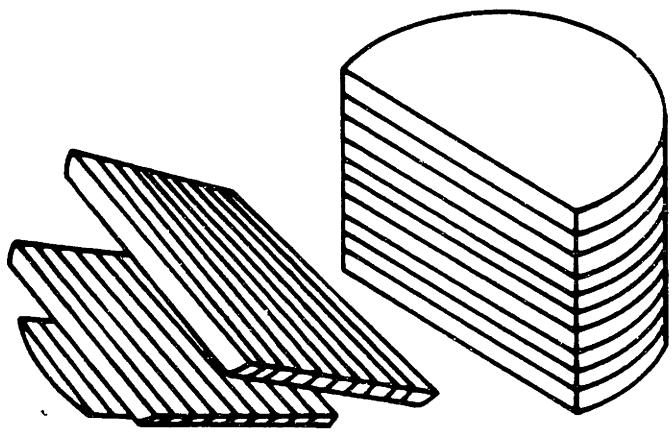

Fig. A3.1 Sawing Strips from Laminated Segment

Once laminated, a hole was cut through both header plates which followed the contour of the flow passages (Fig. (A3.4)). The header plates were then aligned to the core using a special jig to assure that the header plates on either end of a core sectiuon remain parallel.

The plates were cemented with the thin G-10 wafer next to the core by thin beads of Devcon 5-minute epoxy gel (Fig. (A3.5)). The glue joint covered only the edges of the crystal filled with the shimming material so that the flow passages would not be obstructed (Fig. (A3.6)). The high viscosity (consistency of bath tub calk) of Devcon epoxy gel prevented it from being drawn into the flow passages by capillary action.

The outsides of the core sections were then painted with AE-15 epoxy in order to seal the shimmed joints and the header connections. The header plates were useful for preventing the low viscosity epoxy from wicking into the flow passages. The core sections were leak checked using the jig shown on Fig. (A3.7) by pres-

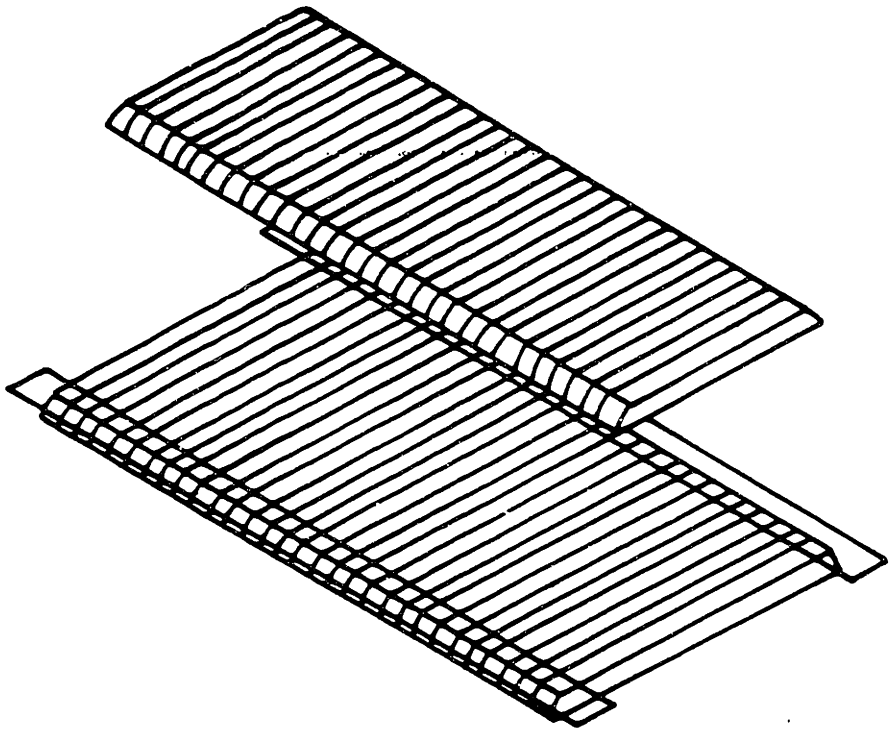

Fig. A3.2 Reassembly of Thirty Wafer Long Strips with Shims

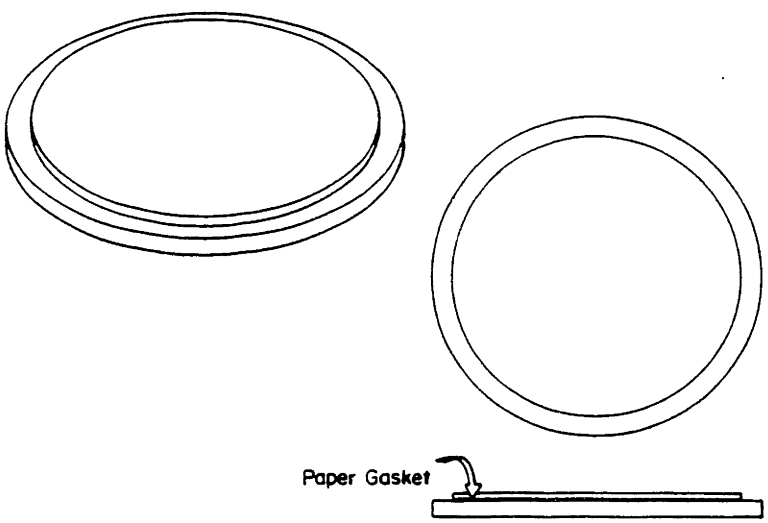

Fig. A3.3 Header Plate Construction

ng them while immersed in water and observing for bubbles. Once leak free
ctions flow resistances were measured and compared with design values. Fig.

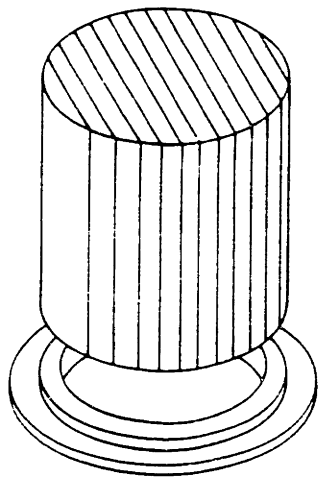

Fig. A3.4 Fitting the Header Plates to The Core Segments

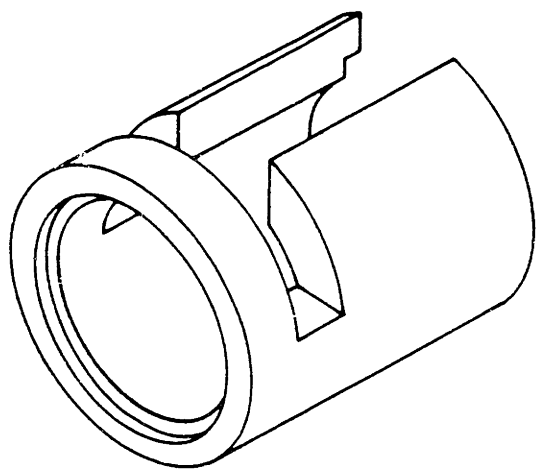

Fig. A3.5 Jig for Aligning the Header Plates

(A3.8) shows the results of these measurements. The design flow resistances were calculated assuming steady, laminar, constant property, fully developed flow.

The fit of the core sections into the vacuum insulated stainless steel sheath required an encapsulant which would have the following properties: ability to form a void free filling between the irregular perimeter of the core and the cylindrical section of the vacuum jacket. This requirement is important both to avoid the unwanted thermal inertia of entrained helium and to prevent helium from bypassing the core during flow processes. The second requirement of the encapsulant is that it survives

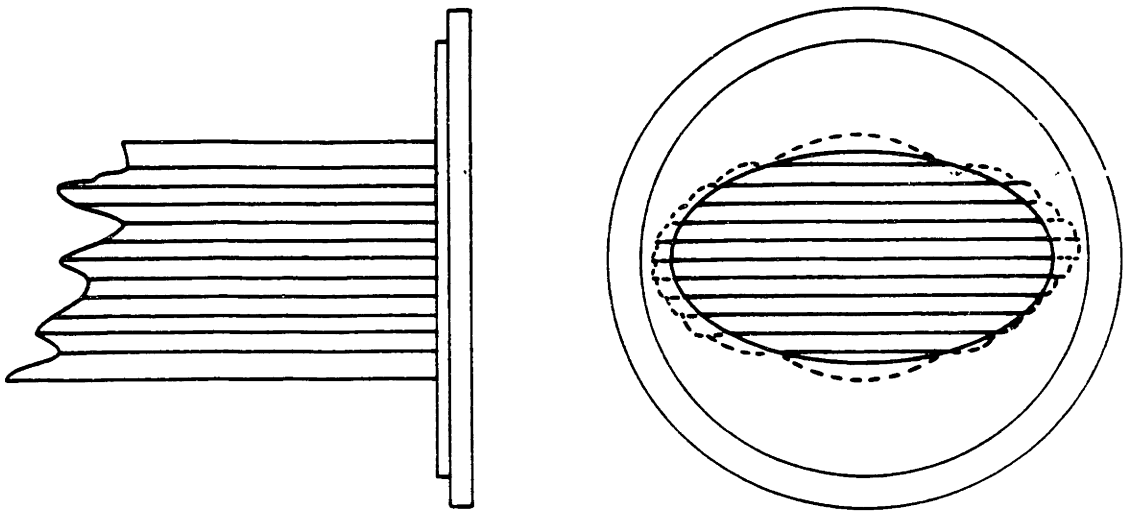

Fig. A3.6 Header Plates Only Cover Shim Material

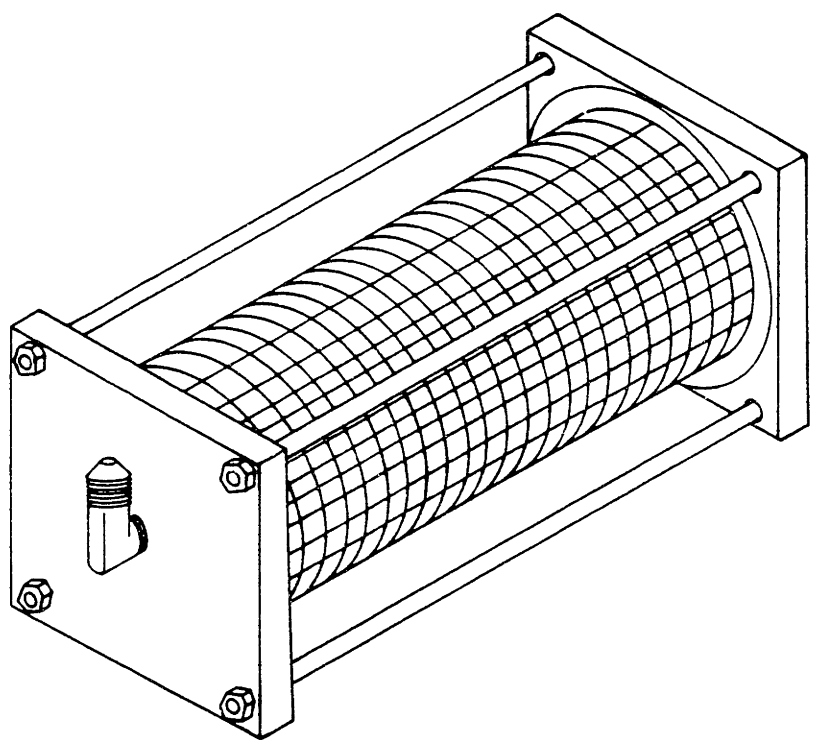

Fig. A3.7 Pressure Checking Jig

the cooldown without either fracturing itself or fracturing the core. The encapsulant must have low thermal mass at operating temperature, low conduction, and must be able to apply or cast to the GGG core sections without extreme difficulty.

G-10 replicas of the regenerator core section were constructed to evaluate the

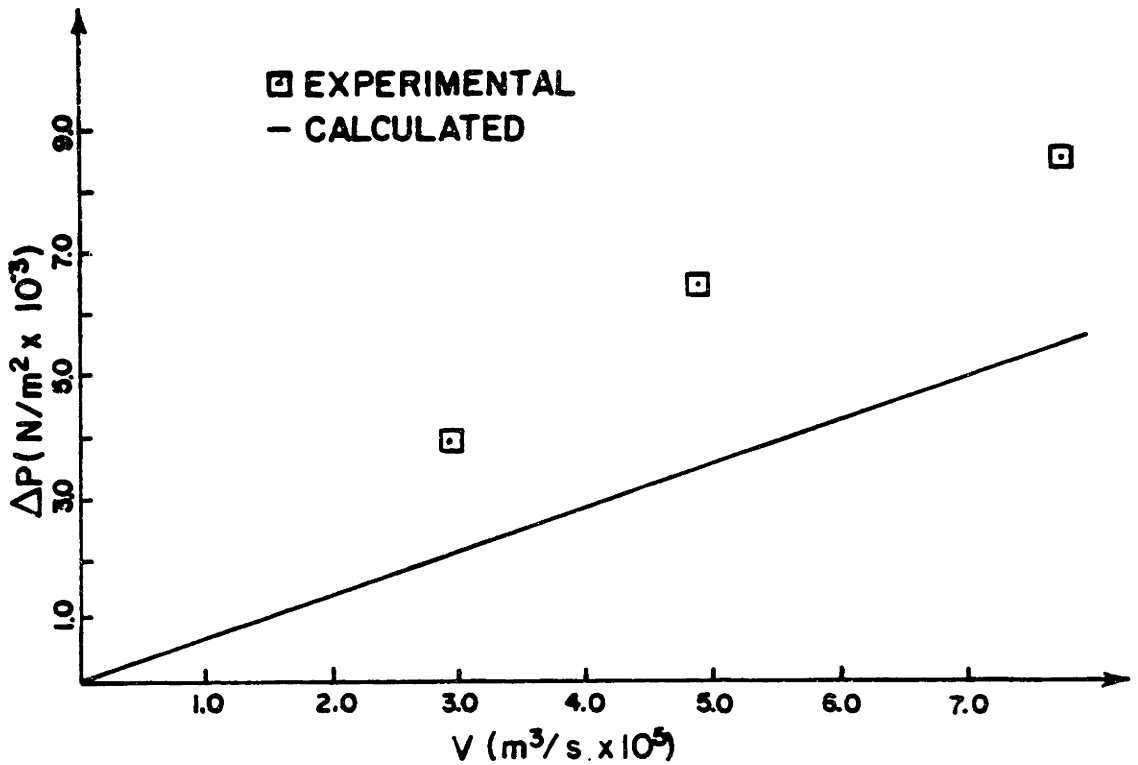

Fig. A3.8 Pressure Drop For Core Sections Compared to Design Values

various encapsulants. The replica core sections were potted with different encapsulants then immersed in liquid nitrogen. Upon warm up the encapsulants were examined for fracture or cracking. The encapsulants investigated were all either epoxies or silicone rubbers. These materials were thought to be the best candidates because of their good casting properties and their resiliency at low temperatures. Polyester resin was given preliminary consideration but was rejected because it shattered on cooldown.

The epoxies as a rule cracked or fractured on cooldown. Micro cracks in the encapsulant could be tolerated so long as they do not appreciably shunt the flow through the core or provide void space which would increase the entrained helium. Additional experiments with test sections made from GGG showed that on cooldown the epoxies tended to shatter the crystal. Various fillers were added to the epoxies

in an attempt to match its thermal contraction to that of the crystal. None of these experiments was successful.

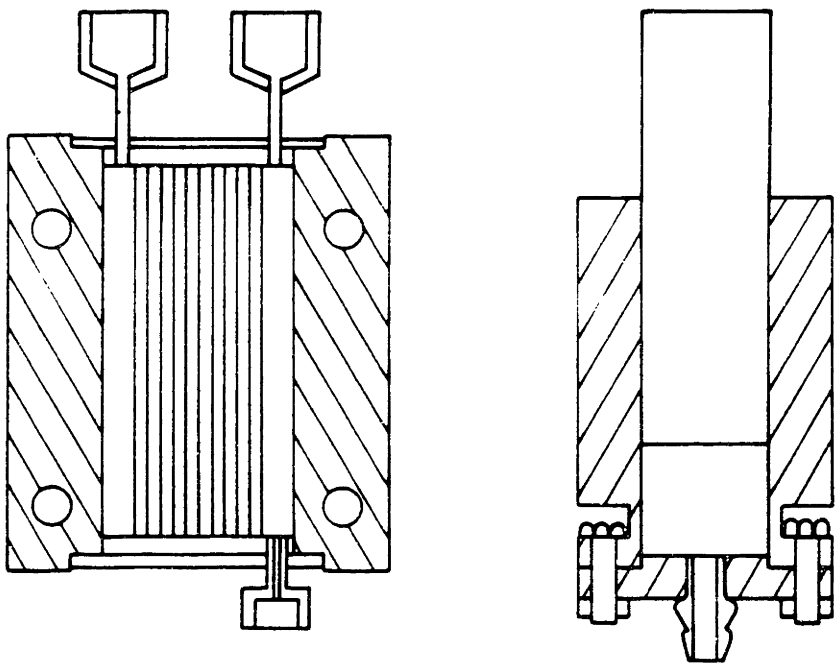

Fig. A3.9 Injector (right) and Mold with Core Section Inside

Silicone rubbers have much higher compliance than epoxies at room temperature. Methyl-phenyl-silicone retains its flexibility down to approximately 100 K. At this point, the majority of thermal strains have transpired, so hopefully neither the crystal or the encapsulant will shatter. The Castall company of East Weymouth MA manufactured the methyl-phenyl-silicone used to encapsulate the regenerator core. Castall's S1251-A was the only product tested which survived cold testing without failing or shattering the crystal. Castall's metallic soap curing agent SC-28 was used as a catalyst because it will not corrode copper and because of its deep section cure ability. Castall P1291 primer was used to improve adhesion between the core section and the encapsulant. Castall 1285 diluent was used to lower the viscosity of the silicone to reduce the chance of void formation during casting. Fig. (A3.9) shows the cross section of the casting set up. Before loading into the injector,

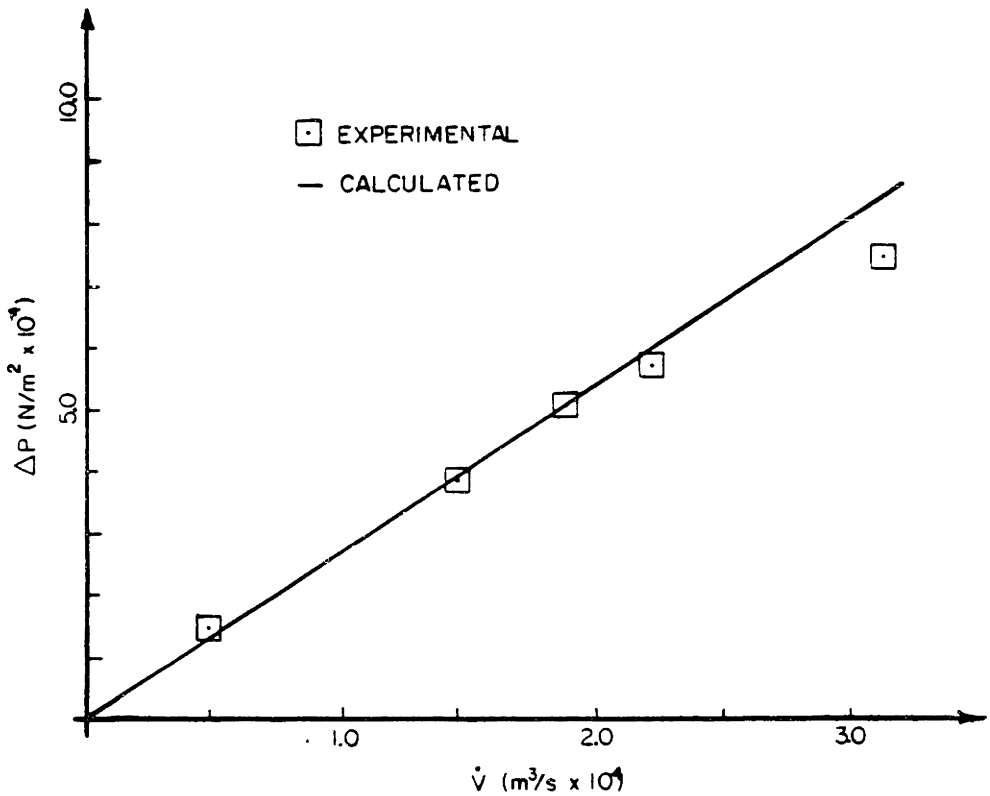

Fig. A3.10 Pressure Drop For Fully Assembled Core

the silicone was degassed by repeatedly pumping it to 700 torr then pressurizing back to 1 atm. The mold used to cast the sections was the same ID as the vacuum jacket into which the assembled core would be installed.

The molds were coated by American Durafilm of Wellsely MA with a teflon coating as a release. A Vaseline coating was wiped on the inside of the mold as a precautionary release. The pot life of the silicone is approximately 1 hour and the cure time approximately 24 hours at 50°C. The core was removed from the mold then trimmed. The trimming process was performed in two steps. First the G-10 header plates were split at the paper gasket so that only the 0.3 mm thick section remained attached to the core. Second, using a concentric tube cutter, the flash at the base of the section was trimmed to a light interference (0.13 mm on the radius) fit with the vacuum jacket to provide a better seal against helium blow-by.

The final step in the assembly of the regenerator core was the installation of the core sections into the vacuum jacket. First the micarta end piece was inserted

in one end of the vacuum jacket, then the core sections were installed sequentially each with a 0.25 mm bead of Devcon 5 minute epoxy gel on its mating gasket with the section ahead of it. A pressure drop test was made on the core after installation in the vacuum jacket. Fig. (A3.10) shows the results of this measurement compared with design calculations. Although laminar flow was present in both test and actual operating conditions no attempt was made to match exact Reynolds number in any of the flow tests.

References

1. F. Sears, *An Introduction to Thermodynamics, the Kinetic Theory of Gasses, and Statistical Mechanics*, Addison-Wesley, Reading, Massachusetts, 1953.
2. N. Tesla, "Pyromagnetic electric generator," U.S. patent 428,057 May 13 1890.
3. K. Mendelssohn, *The Quest for Absolute Zero: the meaning of low temperature physics*. Taylor & Francis, Ltd., London (1977), p. 161.
4. C.G.B. Garret, *Magnetic Cooling*, Harvard University Press John Wiley & Sons, Inc.,(1954).
5. J.E. Zimmerman, J.D. McNutt, & H.V. Bohm."A magnetic refrigerator employing superconducting solenoids." Cryogenics **2**(3), March 1962.
6. C. Delpuech, R. Béranger, G. Bon Mardion, G. Claudet, A.A. Lacaze, "Double acting reciprocating magnetic refrigerator: first experiments." Cryogenics **21** pg 579, 1981.
7. R. Béranger, *etal.*, "A gadolinium-gallium-garnet double acting reciprocating magnetic refrigerator." Adv. in Cryogenic Engr., **27** pg. 703 (1982).
8. A.F. Lacaze, *etal*, "Efficiency improvements of a double acting reciprocating magnetic refrigerator." Cryogenics **21** August 1983.
9. A.F. Lacaze, *etal*, "Thermodynamic analysis of a double acting reciprocating magnetic refrigerator," Proc. 9th International Cryogenic Engr. Confr., Kobe Japan 1982, pg. 14.
10. A.F. Lacaze, *etal*, "Double acting reciprocating magnetic refrigerator: recent improvements." Adv. Cryogenic Engr., **29** pg 573 (1984).
11. G.M. Claudet, "Magnetic refrigeration study at CEA Grenoble." Adv. Cryogenic Engr., **31** pg 733 (1985).
12. H. Nakagome, N. Tanji, O. Horigami, H. Ogiwara, T. Numazawa, Y. Watanabe, T. Hashimoto, "The helium magnetic refrigerator I: Development and experimental results," Adv. Cryogenic Engr., **29** pg. 581 (1984).
13. J.R. van Geuns, "A study of a new magnetic refrigerating cycle." Philips Res. Rep. Suppl. 6 (1966).
14. G.V. Brown, "Magnetic heat pumping near room temperature." J. Appl. Phys. **47**(8) pg. 3673, August 1976.
15. J.A. Barclay, O. Moze, & L. Paterson, "A reciprocating magnetic refrigerator for 2-4K operation: Initial results," J. Appl. Phys. **50**(9) pg 5870, September 1979.
16. J.A. Barclay, "The theory of an active magnetic regenerative refrigerator," 2nd Conference on refrigeration for cryogenic sensors and electronic systems NASA, Goddard Research Center, Greenbelt (1982).
17. R.A. Fisher, G.E. Brodale, E.W. Hornung, & W.F.Giaque, "Magnetothermodynamics of gadolinium gallium garnet. I. Heat capacity, entropy, magnetic moment from 0.5 to 4.2K, with fields to 90kG along the [100] axis,"
18. D.G. Onn, H. Meyer, & J.P. Remeika, "Calorimetric study of several rare-earth gallium garnets," Physical Review **156**(2), pg 663, 10 April 1967.
19. G.A. Slack, & D.W. Oliver, "Thermal conductivity and phonon scattering by rare-earth ions," Physical Review B **4**(2) pg 592 15 July 1971.
20. J.A. Barclay, & W.A. Steyert, "Materials for magnetic refrigeration between 2K and 20K," Cryogenics **22** pg. 73 1982.

21. T. Hashimoto, T. Numasawa, M. Shino, & T. Okada, " Magnetic refrigeration in the temperature range from 10K to room temperature: the ferromagnetic refrigerants," Cryogenics **21**(11) pg. 647 November 1981.
22. Gallagher, G.R., "Analysis of magnetically active regeneration," S.M. thesis Dept. of Mechanical Engineering, MIT, Cambridge MA, October 1986.
23. W. Kays, & A.L. London, *Compact Heat Exchangers*, McGraw-Hill, 1964 pg. 131.
24. P.A. Rios, "An approximate solution to the shuttle heat-transfer losses in a reciprocating machine," Transactions of the ASME, Journal of Engineering for Power, April 1971. pg.17.
25. F.J. Zimmerman, & R.C. Longsworth, "Shuttle heat transfer," Advances in Cryog. Engr., **16**, pg. 342.
26. Advertisement, *Alsthom Atlantique*, 1983, Belfort France.
27. W.W. Chin, "Construction and testing of an AC superconducting magnet for a magnetic refrigerator," S.B. thesis Dept. of Mechanical Engineering, MIT, Cambridge MA, June 1985.
28. G.R. Gallagher, "Experimental investigation of three key thermal processes for a magnetic refrigerator operating in the temperature range between 10 K and 4.2 K," Interim report prepared for the Air Force, Wright-Patterson Air Force Base, Ohio.
29. R.M. Heffernan, "Temperature control system for a low temperature magnetic refrigeration experiment," S.B. thesis Dept. of Mechanical Engineering, MIT, Cambridge MA, June 1985.
30. Kline, & McClintock, "Describing the uncertainties in single sample experiments," Mechanical Engineering, January, 1953. pg. 3.
31. R.D. McCarty, *Thermophysical properties of helium-4 from 2 to 1500 K with pressures to 1000 atmospheres*, NBS Technical Note, November, 1972.
32. A.C. Anderson, "Carbon Resistance Thermometry," *Temperature- Its Measurement and Controlin Science and Industry*, Vol. **4**.
33. H.H. Sample, B.C. Brandt, L. Rubin, "Low temperature thermometry in hogh magnetic fields-CGRs," Review of Scientific Instruments, August 1982. pg. 1129
34. D. Linenberger, "Thermal response times of some cryogenic thermometers," Temperature- Its Measurement and Control in Science and Industry, Vol **5**
35. G. Ries, & H. Brechna, "AC losses in superconducting pulsed magnets," KFK 1372, Gesellschaft fur Kernforschung M.B.H., Karlsruhe, January 1972.
36. D.B. Montgomery, "Solenoid Magnet Design," John Wiley & Sons, inc., 1969.
37. W. Frost, "Heat transfer at low temperatures,"Plenum Press, 1975.

ANNOTATED BIBLIOGRAPHY

In this bibliography the references on magnetic refrigeration will be presented according to the following scheme:

1. Magnetic Refrigeration Devices
   a) Carnot Cycles
   b) Regenerative Cycles
2. Magnetic Refrigeration Materials
   a) Gadolinium-Gallium-Garnet ($Gd_3 Ga_5 O_{12}$)
   b) Other Materials
3. Related References

Within each section the papers are organized by research project and listed chronologically with respect to the first paper written on the project.

MAGNETIC REFRIGERATION DEVICES

Carnot Cycles

1. Zimmerman, J.E., McNutt, J.D., & Bohm, H.V.,"A magnetic refrigerator employing superconducting solenoids," Cryogenics **2**(3), March 1962. Continuous refrigeration of 0.1 mW at 0.257 K from 1.05 K sink, utilizing superconducting heat switches and moving superconducting magnet for excitation.
2. Steyert, W.A., "Rotating Carnot cycle magnetic refrigerators for use near 2 K," J. Appl. Phys. **49**(3), March 1978. Design study for cycle using rotating wheel of magnetic refrigerant and stationary magnet; items 2-4 discuss this project.
3. Pratt, W.P.,Jr.,*et al*,"A continuous demagnetization refrigerator operating near 2 K and a study of magnetic refrigerants," Cryogenics **17**(12) December 1977. Experimental results of 0.450 W refrigeration at 2.7 K from 4 K sink for rotating wheel machine. Problems of poor heat transfer and seal leakage reported.
4. Barclay, J.A., *et al*, "Experimental results on a low temperature magnetic refrigerator," paper presented at the 1985 Cryogenic engineering conference Boston, MA Aug 12-16 1985 to be published in Adv. Cryogenic Engineering,

31. Experimental results of 1 W at $\approx$ 4 K with a temperature span of 2 K: second generation rotating wheel.

5. Barclay, J.A., "A 4 K to 20 K rotational-cooling magnetic refrigerator capable of 1 mW to > 1 W operation," Cryogenics **20** pg. 467, 1980. Design study of rotating wheel machine using anisotropic material ($Dy\,PO_4$) in steady field.

6. Delpuech,C., Béranger, R., Bon Mardion, G., Claudet, G., Lacaze, A.A., "Double acting reciprocating magnetic refrigerator: first experiments," Cryogenics **21** pg 579. 1981. Items 6-11 all refer to this project. Experimental results: 0.5 W at 1.8 K from 4.2 K sink. Configuration: two plugs of copper-GGG composite reciprocated in and out of stationary magnetic fields.

7. Béranger, R. *et al.*, "A gadolinium-gallium-garnet double acting reciprocating magnetic refrigerator," Adv. in Cryogenic Engr., **27** pg. 703 (1982). Analysis of first experiments recommending improvements in field profiles and extending heat transfer surface.

8. Lacaze, A.F., *et al*, "Efficiency improvements of a double acting reciprocating magnetic refrigerator," Cryogenics **21** August 1983. Experimental results after modifying field profile and extending heat transfer surface: 0.9 W at 2.1 K from 4.2 K sink with an efficiency of 64% of Carnot.

9. Lacaze, A.F., *et al*, "Thermodynamic analysis of a double acting reciprocating magnetic refrigerator," Proc. 9th International Cryogenic Engr. Confr., Kobe Japan 1982, pg. 14. Discussion of thermodynamic problems including heat transfer and helium entrainment.

10. Lacaze, A.F., *et al*, "Double acting reciprocating magnetic refrigerator: recent improvements," Adv. Cryogenic Engr., **29** pg 573 (1984). Changing motion of device gives improved performance of 1.2 W at 1.8 K.

11. Claudet, G.M., "Magnetic refrigeration study at CEA Grenoble," Adv. Cryogenic Engr., **31** pg 733 (1985). Survey of work at Grenoble including reciprocating machine and introducing magnetically active regeneration project.

12. Nakagome H., Tanji, N., Horigami, O., Ogiwara, H., Numazawa, T., Watanabe,

Y., Hashimoto, T., "The helium magnetic refrigerator I: Development and experimental results," Adv. Cryogenic Engr., **29** pg. 581 (1984). Carnot cycle machine employing novel heat switch utilizing the different heat transfer coeffients for gas conduction and condensation. The machine has no moving parts and uses a pulsed magnet. The machine produced 6.25 W at 4.2 K from a sink at 20 K with an efficiency of 50% excluding the magnet losses. Items 12-14 describe this project.

13. Numazawa, T., *et al*, "The helium magnetic refrigerator II: Liquefaction process and efficiency," Adv. Cryogenic Engr., **29** pg. 589 (1984). Analysis of heat switch performance.

14. Hashimoto, T., *et al*, "The carnot type magnetic refrigerator below 4.2K: computer simulation," Adv. Cryogenic Engr., **29** pg. 597 (1984). Computer model of machine described above.

15. Nakagome, H., Kuriyama, T., Ogiwara, H., Fujita, T., Hashimoto, T., & Yazawa, T.,"Reciprocating magnetic refrigerator for helium liquefaction," Adv. Cryogenic Engr. **31** pg. 753 (1985). Second generation machine from Toshiba. Employs heat switch from previous machine but uses moving GGG in stationary magnet. Produces 0.95 W at 4.2 K and rejects to sink between 12 K and 15 K. Items 15-17 are related to this project.

16. Fujita, T., *et al*, "An experimental study simulating the helium liquefaction process in a reciprocating magnetic refrigerator," Adv. Cryogenic Engr., **31** pg. 763, (1985). Experimental investigation into the losses of the heat switch used in (15.). Major loss in transient period.

17. Numazawa, T., *et al*, "Improvement in the efficiency of the heat pipe type magnetic refrigerator,"Adv. Cryogenic Engr. **31** pg 771 (1985). Efficiency of heat switch is improved by narrowing the gap between the wall and the magnetic refrigerant.

Regenerative Cycles

18. van Geuns, J.R., "A study of a new magnetic refrigerating cycle," Philips Res. Rep. Suppl. 6 (1966). Original design study for magnetic Stirling cycle. Ph.D. thesis at University of Lieden, supercritical helium regenerator with paramagnetic material as working fluid and refrigerant.

19. Brown, G.V., "Magnetic heat pumping near room temperature," J. Appl. Phys. **47**(8) pg. 3673, August 1976. Experimental device implementing van Geuns' cycle at room temperature using a water and ethyl alcohol mixture as a regenerator and Gadolinium as a working fluid and magnetic refrigerant. A no-load temperature span of 47 K.

20. Steyert, W.A., "Stirling cycle rotating magnetic refrigerators and heat engines for use near room temperature," J. Appl. Phys., **49** pg. 1216 (1978). Rotating wheel concept from Items 2-4 reconfigured in this design study to produce room temperature refrigeration using Stirling cycle.

21. Barclay J.A., Moze, O., & Paterson, L., "A reciprocating magnetic refrigerator for 2-4 K operation: Initial results," J. Appl. Phys. **50**(9) pg 5870, September 1979. Experimental investigation of van Geuns' cycle with machine producing 0.145 W at 3.8 K from a sink at $\approx$ 4.1 K. Moving magnet, moving $Gd_2(SO_4)_3 \cdot 8H_2O$ refrigerant, losses due to instabilities in fluid regenerator.

22. Barclay, J.A., "The theory of an active magnetic regenerative refrigerator," 2nd Conference on refrigeration for cryogenic sensors and electronic systems NASA, Goddard Research Center, Greenbelt (1982). Computer model of system using regenerator core made of magnetic refrigerant with circulating helium working fluid.

23. Taussig, C.P., Gallagher, G.R., Smith, J.L., & Iwasa, Y., "Magnetically active regeneration," Paper presented at the 1985 Cryogenic engineering conference Boston MA, August 12-16 1985. Items 23-25 all refer to the present project.

24. Taussig, C.P., *et al*, "Magnetic refrigeration based on magnetically active regeneration," Paper presented at 4th Intl. cryocooler conf., Easton, MD September

25-26, 1986. Presentation of experimental results.

25. Gallagher, G.R., "Analysis of magnetically active regeneration," S.M. thesis Dept. of Mechanical Engineering, MIT, Cambridge MA, October 1986. Numerical simulation of the device, property corelations for GGG, and simulations of the preliminary experiments.

26. Chin, W.W., "Construction and testing of an AC superconducting magnet for a magnetic refrigerator," S.B. thesis Dept. of Mechanical Engineering, MIT, Cambridge MA, June 1985. Experimental measurement of magnet AC loss, inductance, and field profile.

27. Heffernan, R.M., "Temperature control system for a low temperature magnetic refrigeration experiment," S.B. thesis Dept. of Mechanical Engineering, MIT, Cambridge MA, June 1985. Design and experimental results for temperature controller prototype.

28 Seyfert, P., & Claudet, G., "A superconducting coil with low AC losses for use in magnetic refrigerators," Paper presented at 4TH Intl. cryocooler conf., Easton MD., September 25-26 1986. Experimental results for AC magnet developed for machine very similar to the one discussed in this thesis.

Magnetic Refrigeration Materials

Gadolinium-Gallium-Garnet ($Gd_3 Ga_5 O_{12}$)

29. Fisher, R.A., Brodale, G.E., Hornung, E.W., & Giaque, W.F., "Magnetothermodynamics of gadolinium gallium garnet. I. Heat capacity, entropy, magnetic moment from 0.5 to 4.2 K, with fields to 90kG along the [100] axis," The Journal of Chemical Physics **59**(9) pg 4652, November 1973. One of three papers written in a series each measured the properties relative to a different crystal axis. Properties are isotropic, range of measurement 0-9 T and 0.5-4.2 K.

30. Brodale, E.W., "Magnetothermodynamics of gadolinium gallium garnet. III. Heat capacity, entropy, magnetic moment from 0.5 to 4.2 K with fields to 90kG

along the [110] axis," The Journal of Chemical Physics, **62**(10) pg. 4041, 15 May 1975. Third paper in series explains "per gram mole ion" nomenclature.

Other Materials (some including GGG)

31. Onn, D.G., Meyer, H., & Remeika, J.P., "Calorimetric study of several rare-earth gallium garnets," Physical Review **156**(2), pg 663, 10 April 1967. Includes GGG, same range as items 29 & 30.

32. Cooke, A.H., Thorp, T.L., & Wells, M.R., "The magnetic susceptibilities of some rare-earth garnets," Proc. Phys. Soc., 1967 **92** printed in Great Britain. Includes GGG same range as items 29 & 30.

33. Slack, G.A., & Oliver, D.W., "Thermal conductivity and phonon scattering by rare-earth ions," Physical Review B **4**(2) pg 592 15 July 1971. Includes GGG measurements made from 2 K to 300 K.

34. Barclay, J.A., & Steyert, W.A., "Materials for magnetic refrigeration between 2 K and 20 K," Cryogenics **22** pg. 73 1982. Comprehensive litterature survey and presentation of criteria for selection of magnetic refrigerants. Presents a corelation for data on GGG.

35. Hashimoto, T., Numasawa, T., Shino, M., & Okada, T., " Magnetic refrigeration in the temperature range from 10 K to room temperature: the ferromagnetic refrigerants," Cryogenics **21**(11) pg. 647 November 1981. Discussion of materials for higher temperatures where lattice heat is significant.

36. Numazawa, T., *et al*, "The magnetic refrigeration characteristics of several magnetic refrigerants below 20K: II thermal properties," Proc. Intl. Cryog. Eng. Conf., Kobe, Japan, May 1982. Thermal conductivity of GGG shown to be much larger for single crystal than polycrystaline.

37. Hashimoto, T., *et al*, "The magnetic refrigeration characteristics of several magnetic refrigerants below 20K: I magnetocaloric effect," ' Proc. Intl. Cryog. Eng. Conf., Kobe, Japan, May 1982. Study includes GGG and extends experimental data to 20 K.

38. Hashimoto, T., *et al*, "A new usage of anisotropic magnetic compound for the magnetic refrigerant,"' Proc. Intl. Cryog. Eng. Conf., Kobe, Japan, May 1982. Experimental investigation of some ferromagnetic refrigerants which are anisotropic.

Related Readings

39. Tesla, N., "Pyromagnetic electric generator," U.S. patent 428,057 May 13 1890. Device uses iron's loss of ferromagnetism above the Currie temperature to break the flux in a magnetic circuit. Cyclic heating produced AC voltage.

40. Rosenweig, R.E., "Fluid dynamics and science of magnetic liquids," Advances in Electronics and Electron Physics **48** pg. 103 1979. Interesting concept possible applications to fluidized bed magnetic refrigerators.